UNIVERSITY OF SOUTHAMPTON

Stability of thin film insertion electrodes

Béatrice GAVANIER

Doctor of Philosophy

FACULTY OF SCIENCE

CHEMISTRY

APRIL 2000

UNIVERSITY OF SOUTHAMPTON

ABSTRACT

FACULTY OF SCIENCE

CHEMISTRY

Doctor of Philosophy

STABILITY OF THIN FILM INSERTION ELECTRODES

By Béatrice GAVANIER

This work investigated the effect of inserting and extracting lithium from metal oxides used in an electrochromic device. Both the electrochromic (tungsten oxide) electrode and the vanadium-titanium oxide electrode were studied separately. The electrochemical behaviour of these electrodes was studied using slow scan cyclic voltammetry and AC-impedance spectroscopy. Scanning electron microscopy was used to study the surface of the electrode before and after cycling. Vanadium-titanium oxide samples were also studied using an electrochemical quartz crystal microbalance.

Two forms of tungsten oxide were studied: amorphous and crystalline tungsten oxide samples. Normal conditions for the electrochemical study of tungsten oxide electrodes were defined by a potential range of 2 V *vs.* Li/Li^+ to 4.5 V *vs.* Li/Li^+. The samples were then cycled to potentials as low as 1.6 V *vs.* Li/Li^+. The amorphous samples showed a very poor stability at these potentials where crystalline samples showed a good stability. A model was proposed where the adhesion between the oxide layer and the underlying conductive layer is a key factor. Inserting lithium at very low potential causes an expansion of the film. When the strain forces exceed the adhesion forces, the expansion of the film causes film detachment. By heating the samples to get the crystalline form of tungsten oxide, the adhesion properties of the film and thus its stability upon lithium insertion-extraction are improved.

The electrochemical behaviour of vanadium-titanium oxide was studied using slow scan cyclic voltammetry, which showed a parasitic reaction superimposed on the insertion/extraction current. The quartz crystal microbalance *in-situ* measurements showed that hydrated lithium is inserted under mild conditions (above 3.2 V *vs.* Li/Li^+). At potential below 3.2 V, lithium ions are the only species inserted. During a slow extraction, an increase of the slope showed an additional loss of mass, which probably corresponds to the extraction of the hydrated lithium ions.

Acknowledgements

I would first like to thank Dr John Owen for offering me the chance to do my PhD in his group, for his advice all the way through this work and his patience.

I also want to thank the European community for funding the project I was working on. In this project, I have collaborated with a few people outside the university of Southampton. I would like to thank Dr José Gallego from Pilkington Technology Centre for his help during the project. At Oxford Brookes University, Pr Michael Hutchins and Mr John Topping have been very helpful with the crystalline tungsten oxide samples, I would like to thank them. I want to thank Dr Marine Consigny at Danionics (Denmark) and Pr Boris Orel at the National Institute of Chemistry (Slovenia) for their kindness all the way through the project.

I also want to thank many people in the lab. First, Dr Adam Whitehead for his help with the electronics and all his advice for the electrochemical problems and the long discussion outside the lab; Mr Nick Gray for his help with the computers; Mr Alistair Clark for his help with the scanning electron microscope and the sputtering machine. Finally, I want to thank Melanie, Emmanuel, Mike, Yaser, Virginie, Emmanuelle, Lionel, Stefano for their help in the every day tasks in the lab.

Last but not least, a very special thank for Franck, for his help and his support during the last three years.

TABLE OF CONTENTS

CHAPTER 1. INTRODUCTION. 3

1.1. Electrochromism and its applications. 3

1.2. Background and aims of the project. 6

1.3. Principles of electrochromic devices. 7

1.4. Transparent electrical conductor. 9

1.5. Electrochromic materials. 9
1.5.1. Metal oxides. 9
1.5.2. Inorganic non-oxide electrochromic materials. 13

1.6. Electrolytes. 13

1.7. Counter electrodes. 17

1.8. Theory of insertion materials. 18
1.8.1. Principle of insertion electrodes. 18
1.8.2. Atomic and electronic structure of the electrodes studied. 20
1.8.3. Chromic mechanism in amorphous tungsten oxide. 25
1.8.4. Thermodynamics of insertion. 27
1.8.5 Kinetics of insertion. 31
1.8.6. Summary. 33

1.9. Stability of metal oxides. 34

1.10. Electrochemical quartz crystal microbalance study of insertion materials. 35

1.11. Scope of own work. 36

CHAPTER 2. THEORY OF THE EXPERIMENTAL TECHNIQUES. 36

2.1. Cyclic voltammetry. 37

2.2. AC- impedance spectroscopy. 38

2.3. Ex-situ physical characterisation. 40
2.3.1. Scanning electron microscopy. 40
2.3.2. Tungsten spectrophotometric titration. 41

2.4. In-situ characterisation. 42
2.4.1. UV-visible spectroscopy. 42
2.4.2. Quartz crystal microbalance. 42

CHAPTER 3. EXPERIMENTAL DETAILS. 45

3.1. Samples preparation. 45

3.2. Preparation of materials. 47
3.2.1. Electrode for cyclic voltammetry and UV-visible in situ. 47
3.2.2. Electrode for the electrochemical quartz crystal microbalance. 48
3.2.3. Electrolyte preparation. 49

3.3. Cell construction. 49

CHAPTER 4. RESULTS ON TUNGSTEN OXIDE 53

4.1. Amorphous tungsten oxide. **53**
4.1.1. "Standard" amorphous tungsten oxide from Pilkington. 54
4.1.2. Amorphous tungsten oxide sputtered at higher power. 66
4.1.3. Amorphous WO_3 sputtered at Southampton. 71

4.2. Crystalline tungsten oxide. **86**
4.2.1. Cyclic voltammetry. 86
4.2.2. UV-visible in situ. 91
4.2.3. Effect of the substrate. 94

4.3. Comparison of samples - Conclusions. **98**

CHAPTER 5. RESULTS ON VANADIUM TITANIUM OXIDE COUNTER ELECTRODE. 100

5.1. Effect of the sputtering conditions. **100**

5.2. Cyclic voltammetry. **102**

5.3. Electrochemical quartz crystal microbalance. **106**

5.4. Conclusions. **111**

CHAPTER 6. CONCLUSION. 112

REFERENCES 114

Chapter 1. Introduction.

1.1. Electrochromism and its applications.

Electrochromism is a word used to describe the ability of some materials to change their optical properties upon the application of an electric current or an applied field. Electrochromism has attracted a lot of interest in the last 30 years and many papers have been published on the subject including two books (1, 2). Ideally, the change of optical properties should be reversible in the visible (400 nm < λ< 800 nm) and the near infrared region (800 nm < λ < 2500 nm).

The word electrochromism was introduced by Platt (3) in 1961 in analogy to thermochromism and photochromism. He was studying the effect of an electric field on the optical absorption spectrum of an organic dye. His idea came from the fact that the absorption peaks of some molecules can be changed by dissolving the dye in solvents of various polarisability and he looked at the effect of an electric field instead of a change of solvent and came to the conclusion that it has the same effect.

But it was Deb in 1969 who described the electrochromism of tungsten oxide and its possible applications (4, 5). Deb knew that tungsten oxide could be coloured by the application of an electric field and he applied this property to an "electrophotographic" system in which he sandwiched a film of WO_3 between two electrodes and changed the colour by applying a voltage of 1 V. The more conductive the tungsten oxide was, the darker it became. He built a device where tungsten oxide is sandwiched between a gold plate on one side and a CdS plate on the other side. This sandwich is deposited on SnO_2 coated glass. CdS is a semiconductor that becomes more conductive with light. Thus, if the image is projected and a DC field is applied across the device, an image is formed as the circuit is completed and the tungsten oxide is coloured. This device showed a good switching time, a memory effect at power off, a good reversibility and a good contrast. He did not give an explanation to the coloration of tungsten oxide but this first application attracted interest to this phenomenon.

In his second paper on the subject (5), he noticed that amorphous tungsten oxide showed a better coloration than the crystalline form. The coloration occurred when the light corresponded to excitation energies across the bandgap with a maximum at 3.6 eV. He found that the coloration efficiency was temperature and moisture dependent and increased by doping the film with electron donors. He then concluded that the coloration was due to the injection of electrons associated with a positive defect in WO_3 structure. The effect of the moisture was then explained by the dissociation of water giving protons that could act as charge compensating ions in the layer. It is interesting to note that in this device, there is no electrolyte. That means that the tungsten oxide layer used must have had a lot of defects in the structure.

Since this work, a lot of interest was shown in the electrochromic phenomenon and many electrochromic materials have been discovered. Two types of electrochromic materials can be distinguished: organic and inorganic. In this work we will only refer to inorganic electrochromic materials.

Electrochromism can be used in four major applications: information displays, variable reflectance mirror, smart window and variable emittance surface. These applications are described in figure 1-1.

Figure 1-1a shows the principle of an information display where the electrochromic film is located in front of a diffusely scattering pigmented surface. This gives good viewing properties and better contrast than liquid crystal devices. These systems were studied for the same applications (i.e. wrist-watch displays) as liquid crystals in the 1970s but a better durability and a faster response for the liquid crystals led to the development of liquid crystals for these applications.

Figure 1-1b shows the principle of a variable reflectance mirror where the electrochromic layer sits in front of a mirror. This is the more mature application of electrochromism as it has been available since 1994. Work on variable reflectance mirrors was started by Schott in Germany (6) and subsequently work was done at Donnelly Corporation in the U.S in collaboration with Optical Coatings Labs. Inc., to produce an all solid state mirror that was supplied to Land Rover in 1991. The most

successful electrochromic mirror was the anti-glare mirror, the Gentex Night Vision Safety (NVS ®) Mirror from Gentex Corporation.

Finally, figure 1-1c shows the principle of an electrochromic window designed as "smart window" by Svensson and Granqvist in 1985 (7). The idea is to modulate the incoming/ outcoming light through a window, the main purposes being the energy saving and comfortable indoor temperature especially in warm regions where air conditioning is very expensive. For the moment, an electrochromic window remains expensive but with the development of the technique and many new materials, the price should decrease.

The variable emittance shown in figure 1-1d can have applications in space technology where energy exchange is mainly due to radiation. The principle of this device is based on the outer layer of crystalline tungsten oxide. Insertion/ extraction of cations in this layer makes the surface infrared reflecting/ absorbing. This application is described more precisely by Braig and Meisel (8).

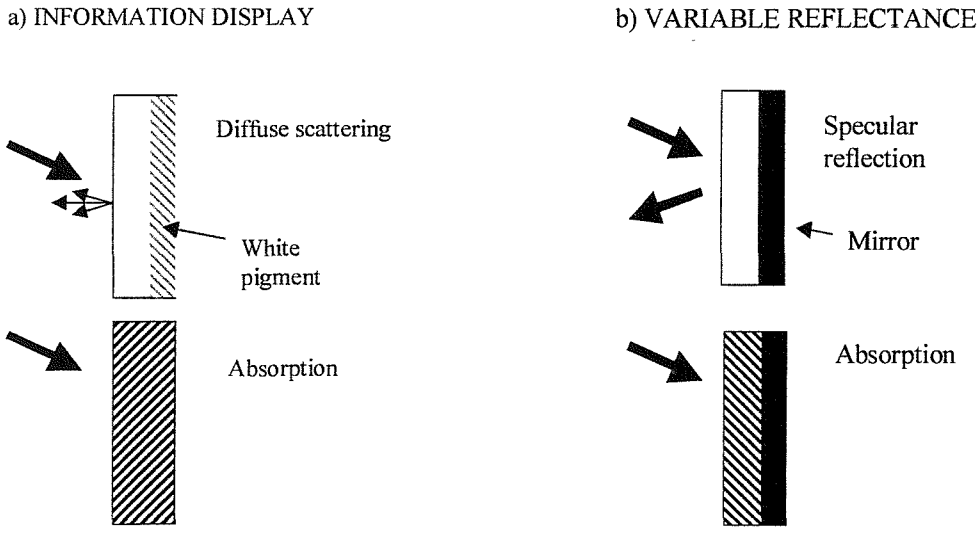

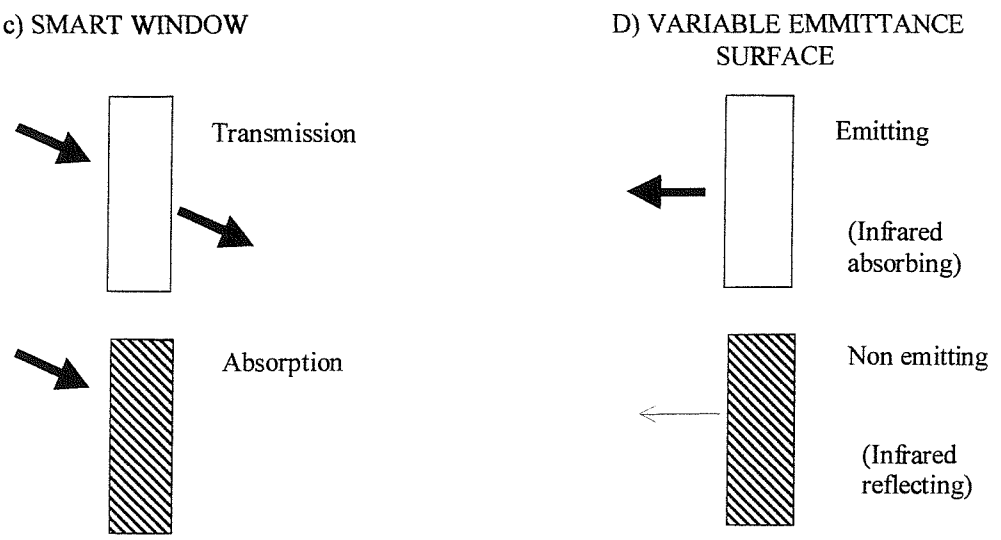

Figure 1-1: Four different applications of electrochromic devices.

1.2. Background and aims of the project.

Electrochromism has attracted a lot of interest in the last 30 years. The energy savings and the comfort are two reasons for this interest. In this context, the laboratory was involved in the Joule "Smart Window" projects funded by the European community and this work was part of the Joule III project. This project was following two other projects (9) in which various electrochromic materials were studied and at the end of the second project, it was decided to use tungsten oxide as the electrochromic material and vanadium-titanium oxide as the counter electrode material. The aim of this project was to produce an electrochromic window and our role was to study the electrochemical behaviour of the electrodes. We were particularly interested by the stability of these electrodes.

The electrochromic electrode in this project was tungsten oxide deposited by sputtering and we tested samples made at Pilkington Technology Centre and Oxford Brookes University as well as our own samples. We used slow scan cyclic voltammetry and AC-impedance spectroscopy to study these materials. We also used UV-visible spectroscopy in situ to look at the optical properties of the samples and scanning electron microscopy to investigate the effect of cycling on the surface of the

electrode. Our main objective was the determination of a safe cycling potential range for the electrode and the determination of the failure mechanism.

The second type of electrode studied was the counter electrode. In our case, it was a mixed vanadium-titanium (50/50) oxide electrode prepared by sputtering. All the electrodes studied were prepared at Southampton. We used slow scan cyclic voltammetry and electrochemical quartz crystal microbalance to study these electrodes.

1.3. Principles of electrochromic devices.

An electrochromic device is usually constituted of superimposed layers as shown on figure 1-2. Usually, the different layers are sandwiched between two glass substrates. The glass substrates are coated with an electrically conducting transparent layer which provides the electron necessary for the charge balance in the electrochromic and ion storage layer during the insertion and/or extraction of the cation. One of the coated glass slides is then covered with a layer of storage material: electrochromic material and the other one with the ion storage material. These materials should be electronic and ionic conductors. An ion-conducting electrolyte is put between the two electrodes to complete the device. Usually, ITO (indium tin oxide) or FTO (fluorine doped tin oxide) are used as transparent conducting layer. The electrochromic layer is usually a transition metal oxide. The counter electrode can be either a complementary colouring electrochromic electrode or a neutral ion storage material. The ion-conducting layer is often a polymer or a hydrous metal oxide. A more detail description of the constituent of the electrochromic device is given below: transparent electronic conductor, electrochromic electrode, electrolyte and counter electrode (ion storage electrode).

The electrochromic efficiency also called coloration efficiency (CE) is defined as the change in optical density per unit of charge:

$$CE = \Delta(OD) / \Delta Q$$

High coloration efficiency corresponds to a large change of optical properties for a small charge inserted. This means that, for the electrochromic window to be effective,

the working electrode and the counter electrode needs to be complementary (one anodic electrochromic material and one cathodic electrochromic material) or they need to have coloration efficiency very different if both electrode are cathodic or anodic electrochromic materials. For an electrochromic device, the coloration efficiency should be about 20 $cm^2.mC^{-1}$. Usually, thin films are used for the electrodes: less than 1 μm. The switching time is also an important characteristic for a commercially viable device. It should be of the order of 2 to 3 minutes for a window for this project.

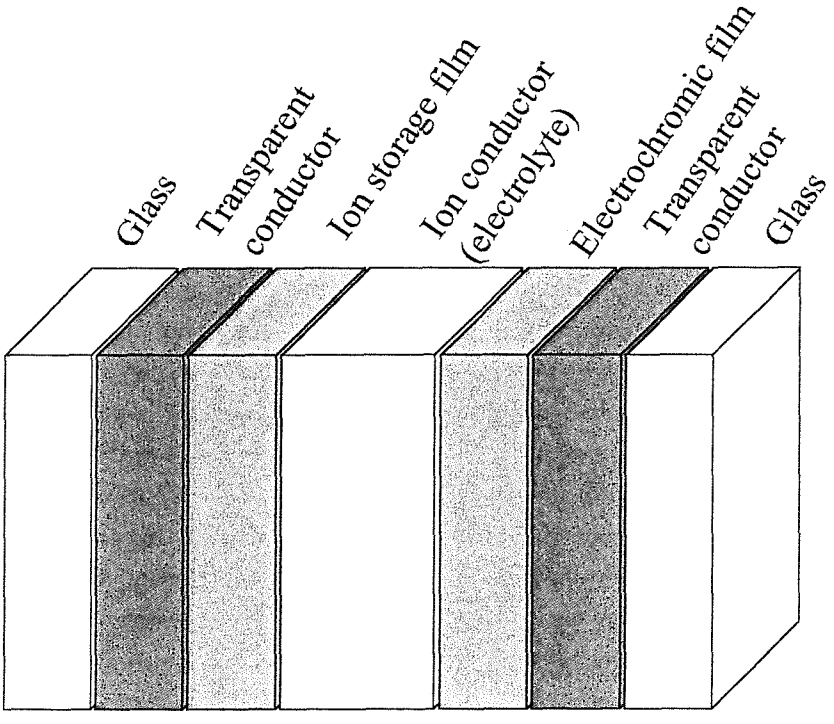

Figure 1-2: Layered design for an electrochromic design.

The half reactions of this cell are:

$EC + xM^+ + x\ e^- \leftrightarrow M_xEC$ for the electrochromic electrode

$M_xCE \leftrightarrow CE + xM^+ + x\ e^-$ for the counter electrode.

The complete reaction is:

$EC + M_xCE \leftrightarrow M_xEC + CE$

The reaction is fully reversible for a perfect device with no side reactions: solvent degradation or electrode degradation. These side reactions can occur in a real device and need to be avoided to have a device with a long lifetime.

1.4. Transparent electrical conductor.

Transparent electrical conductor needs to have a low "resistance per square", defined as $R_{square}=\rho \cdot d$ with ρ the resistivity of the film and d its thickness. Usually, the "resistance per square" has a value between 1 and 100 $\Omega.cm^{-2}$. Heavily doped semiconductors are often used as transparent electrical conductor. They are strongly adherent to the glass and their resistivity depends on the thickness of the film. The most commonly used semiconductors are Sn doped In_2O_3 (ITO) and fluorine doped tin oxide (FTO referred to as K-glass^{TM}). The optical properties can be modified without compromising the good conductivity by changing the dopant concentration and the thickness of the film.

1.5. Inorganic electrochromic materials.

1.5.1. Metal oxides.

Most well known inorganic electrochromic materials are transition metal oxides. In all these materials, the change of optical properties is induced by the reversible insertion/ extraction of small ions, typically H^+, Li^+, Na^+ or K^+:

$$MO_x + yI^+ + ye^- \leftrightarrow I_y MO_x$$

Coloured	uncoloured	for anodic electrochromism
Uncoloured	coloured	for cathodic electrochromism.

Where M is a transition metal and I=H, Li, Na or K.
Because of the charge neutrality, the insertion of a cation is accompanied by the insertion of electron.

Well known examples of electrochromic metal oxides are WO_3, MoO_3, NiO_x. These materials and their properties are described later.

Electrochromic reaction has been showed and studied in many transition metal oxides. Table 1-1 gives, after Granqvist (1), a list of electrochromic oxides and their characteristics: anodic or cathodic coloration, full transparency and type of structure (layered or framework). Granqvist gives a full review of the deposition, electrical properties and optical properties of these oxides.

Electrochromism has also been reported in mixed oxides such as MoO_3-WO_3 (10), TiO_2-WO_3 (11, 12, 13), V_2O_5-MoO_2 (14) and TiO_2-V_2O_5 (15, 16), V_2O_5-WO_3 (17, 18).

Oxide	Coloration	Full transparency	Structure type
TiO_2	Cathodic	Yes	Framework
V_2O_5	Cathodic /anodic	No	Layered
Cr_2O_3	Anodic	No	Framework
MnO_2	Anodic	No	Framework
FeO_2	Anodic	No	Framework
CoO_2	Anodic	No	Layered?
NiO_2	Anodic	Yes	Layered
Nb_2O_5	Cathodic	Yes	Framework
MoO_3	Cathodic	Yes	Framework / layered
RhO_2	Anodic	?	Framework
Ta_2O_5	Cathodic	Yes	Framework
WO_3	Cathodic	Yes	Framework
IrO_2	Anodic	Yes	Framework

Table 1-1: Summary of the principal electrochromic oxides and their properties.

All the oxides listed above have structures based on MeO_6 octahedra linked together by corner sharing, edge sharing or a mixture of both giving framework or layered structure with channels big enough to for insertion cations to move. They exist in various phases and they all have a crystalline, polycrystalline and amorphous structure.

Tungsten oxide is used as the active material on the working electrode in most cases. The first reason for that is the amount of work done on this oxide that makes it very easy to find information to compare with your sample. The second reason is the attractive colour of tungsten oxide in the inserted state: very nice blue colour. Also, the change in transmittance occurs at wavelengths where the IR radiation can be controlled and thus the thermal exchange can be controlled reducing air conditioning bills. The very good coloration efficiency and the good ion insertion reversibility also explain the interest showed for this oxide.

The other transition metals oxides give different colours as shown in table 1-2. All these oxides have been proposed for use as electrochromic electrode in a working device, many of them due to the desire of an electrochromic device that is not blue. The mixed oxide also have attracted interest and some of them are very promising, for example WO_3-MoO_3.

Nickel oxide is the anodic electrochromic oxide studied the most both in acidic aqueous media and with lithium ion non aqueous media (19, 20, 21).

Material	Cathodic colour	Anodic colour	Electrolyte	Comments
WO_3	Blue Up to x=0.5	Transparent	Aqueous non aqueous	Most viable
MoO_3	Blue, purple, dark grey	Yellow (as deposited) transparent	Aqueous non aqueous	Less stable than WO_3
WO_3/MoO_3	Grey	Transparent	Aqueous non aqueous	Neutral colour
Nb_2O_5	Dark blue	Pale blue	Aqueous Li^+ in non-aq.	H_2 evolution
V_2O_5	Brown, green, grey	Beige, yellow	Aqueous Li^+ in non-aq.	High charge capacity, many valence states
TiO_2	Blue	Transparent	H^+ aqueous Non aqueous	H_2 evolution
IrO_2	Transparent	Blue	H_2SO_4 Li^+, OH^-	Expensive and rare
RhO_2	Pale yellow	Dark green	5 M KOH	Risk for O_2 evolution
NiO_2	Transparent	Dark grey	Weak alkaline	Neutral colour
CoO_2	Red, purple	Grey, black	Weak alkaline	Limited open circuit memory

Table 1-2: Main electrochromic oxides and their characteristics.

1.5.2. Inorganic non-oxide electrochromic materials.

Transition metal hexacyanometallates form an important class of insoluble mixed valence compounds. They have the general formula: $M_k[M'(CN)_6]_l$ where M and M' are transition metal ions with different valences. Iron hexacyanoferrate known as prussian blue is the most widely studied (22, 23).

Prussian blue (a hexacyanoferrate) can be reversibly changed from transparent to dark blue upon ion insertion and extraction:

$$Fe_4^{3+}[Fe^{II}(CN)_6]_3 + xe^- + xK^+ \leftrightarrow K_x^+ Fe_x^{2+} Fe_{4-x}^{3+}[Fe^{II}(CN)_6]_3$$

Blue colourless

Partial oxidation leads to a green product known as Berlin Green or Prussian Green and complete oxidation gives a yellowish product called Prussian yellow where both iron ions have a +3 valence state.

A new type of electrochromic material was recently discovered: lanthanide hydrides, which can switch from metallic to transparent by intercalation of protons (24).

$$LnH_2 + H^+ + e^- \rightarrow LnH_3$$

Metallic transparent

This reaction gives an electrochromic switchable mirror. Even better performance can be obtain with magnesium lanthanide alloys (25-26) which are colour neutral and show virtually no absorption in the visible.

1.6. Electrolytes.

The electrolyte assures the ionic conductivity between the electrochromic electrode and the ion storage electrode. Thus its electronic conductivity must be very small and its ionic conductivity must be high enough to allow good performances of the device. The total ionic conductivity σ_i is the sum of the cationic conductivity σ_+ and the anionic conductivity σ_-. In the case of an electrochromic device working by insertion/extraction of cation, we are interested in the ratio of the ionic conductivity

due to the cation. This ratio is called the cationic transport number: $t_+ = \frac{\sigma_+}{\sigma_i}$. In the same way, the anionic transport number is defined by $t_- = \frac{\sigma_-}{\sigma_i}$. The conductivity necessary for good performances of the device depends on the switching time required. The IR drop in the electrolyte should not exceed 5 to 10 % of the applied voltage i.e. for an applied voltage of 1 to 2 V, the IR drop should be of the order of 100 mV. Assuming an average current density of 1 mA/cm^{-2}, we can calculate the conductivity required of 10^{-4} S.cm^{-1} at room temperature as shown on equation below for a switching time of about 15 s (assuming a charge needed of about 15 mC/cm^2 as seen for tungsten oxide samples for example).

$$\Delta U = RI = \frac{e}{\sigma S} I \Leftrightarrow \sigma = \frac{e}{\Delta U} \frac{I}{S}$$

$$\sigma = \frac{0.01cm}{0.1V} 0.001 A/cm^2$$

$$\sigma = 10^{-4} S.cm^{-1}$$

ΔU : RI drop

R: electrolyte resistance

I current

e: electrolyte thickness

S: surface area of electrodes

σ: electrolyte conductivity

For large samples, one minute is often an acceptable switching time and a conductivity of about 2.5x10^{-5} S.cm^{-1} is then enough.

For electrochromic devices, there are three choices for the electrolyte (ion conductor): liquid electrolytes, solid inorganic conductors and solid polymer electrolytes as shown in table 1-3.

The second important parameter for the electrolyte is the stability at the potential range used to colour and bleach the electrochromic device. The stability of the electrolyte depends on the stability of each constituent of the electrolyte. Each constituent of the electrolyte must have a potential window as big as the potential range used to run the device. For example, the stability of a polymer electrolyte depends on the stability of the polymer itself but also on the stability of the salt and eventually on the stability of the additives (plasticiser, etc). The potential window of the electrolytes containing protons is limited on the cathodic side by the reduction of protons.

Type of electrolyte	Conductivity ($S.cm^{-1}$) at 25°C	References
Polymer electrolytes		
PEO-LiTFSI [a]	$2x10^{-5}$	27
PEO-KTFSI [b]	$\sim 5x10^{-6}$	28
Poly-AMPS [c]	10^{-2}	29
BPEI, $1.5H_3PO_4$ [d]	10^{-3}	30
Nafion H^+, in water	$6.8x10^{-2}$	31
Nafion Li^+, in PC [e]	10^{-4}	32
Inorganic solid electrolytes		
$LiNbO_3$	10^{-7}	29
Li_2O-B_2O_3	10^{-7}	29
$LiAlSiO_4$	$4.7x10^{-6}$	29
HUO_2PO_4, $4H_2O$	$4x10^{-3}$	29
Ta_2O_5, 3.92 H_2O	10^{-3}	29, 33
Sb_2O_5, $4H_2O$	10^{-3}	29
Liquid electrolytes or gels		
H_2SO_4 1 M + water	$3x10^{-1}$	29
$LiClO_4$ 1 M + water	$7.4x10^{-3}$	29
$LiClO_4$ 1 M + PC	$4.7x10^{-3}$	34
$LiClO_4$ 1 M + γ-butyrolactone	$6x10^{-3}$	29
Nafion Li^+ 0.3 M + PC	$4.5x10^{-4}$	32
$LiClO_4$ 1 M +PC + PMMA[f] (20% weight)	$2.3x10^{-3}$ to $6x10^{-4}$	34

Table 1-3: Electrolytes used in electrochromic systems and their conductivity at 25°C.

a Polyethylene oxide + lithium trifluorosulfonimine

b *ibid.* with potassium salt

c. poly-2-acrylamido-2-methylpropanesulfonic acid

d polyethylene imide

e propylene carbonate

f polymethylmethacrylate

Liquid electrolytes have been used a lot to make devices and many different electrolytes have suitable conductivities, potential windows, resistance to degradation under UV light, etc. But, they have been rejected for various reasons. First, the electrolytes would fall under gravity to the bottom of the device causing failure. The second reason is the risk of leakage and if the windows were broken, the electrolyte that could be toxic or corrosive would spill causing a hazard. The third reason is the lack of adhesion. For a commercial use of a smart window, the device should not break in many sharp pieces and a product based on liquid electrolyte between two glass plates would probably shatter.
The second type of electrolyte is inorganic solid ion conductor. Many devices have been made using such electrolytes and are still made by some producers but they also have some problems such as the lack of adhesion of the device, the reduced transmission due to the extra inorganic layer.

The last type of electrolyte is polymer electrolytes. Many researchers are now working with polymer electrolytes and have found suitable electrolytes (cf. Table 1-3). The positive point of polymer electrolytes is the good adhesion to the oxides. They also avoid the risk of leakage. The negative point of polymers is lower ion conductivities than other electrolytes. They also degrade upon ultraviolet irradiation or heating. Many combinations of salt and polymer can be found. For proton conduction, polysulfonic acids and polyvinyl alcohols are commonly used. For lithium and sodium conduction, polyethylene oxide, propylene glycol and poly-methyl methacrylate are very popular. Propylene carbonate is often used as plasticiser to improve the mechanical properties and the ionic conductivity.

The choice of the ion used is also very important. As said previously, H^+, Li^+, Na^+ or K^+ can in theory be used but in practice, protons and lithium ions have been preferred because of their fastest kinetics. H^+ has the greatest diffusion coefficient and therefore gives a faster switching time for the device. It is also more convenient because using protons, the device can be assembled in ambient conditions. However, protons present a major inconvenience as tungsten oxide (electrochromic material used in most devices) dissolves in acidic medium. The other problems are the possibility of gas evolution in a water containing system. These problems would cause a device failure over the long term and therefore protons have become less popular. The use of Li^+

implies that the device is constructed in non-aqueous conditions but this is not a problem with modern manufacturing techniques. Thus lithium is the ion chosen by most researchers now.

1.7. Counter electrodes.

All the materials listed in the tables 1-1 and 1-2 have also been proposed as counter electrode. The choice of the counter electrode is very important for the electrochemical and optical properties of the complete device. It can either be a material with a very low electrochromic efficiency that would stay almost transparent during the whole insertion/extraction process or it can be a material that colours and bleaches simultaneously with the electrochromic electrode.

Anodic electrochromic materials are favoured due to the large change in transmission obtained but it can be difficult to obtain a completely bleached state using this type of counter electrode. For example, the system WO_3 coupled with NiO_x has been used by Passerini *et al.* (35) and elsewhere.

Thus, cathodic electrochromic materials with very low electrochromic efficiency have been used as counter electrode in the electrochromic devices i.e. TiO_2 (36, 37, 38), V_2O_5 (39,40, 41), SnO_2 (42, 43). Combination of these oxides and doped oxides are also used: CeO_2 (44), TiO_2-V_2O_5 (15,16, 45), CeO_2-TiO_2 (46), CeO_2-SnO_2 (47), MnO_2-V_2O_5 (48), Sb-SnO_2 (42), ZrO_2-CeO_2 (49), titanium oxyfluoride (37).

Among these mixed oxides, vanadium titanium oxide and cerium titanium oxide are the most studied. The electrochemical and optical properties of these oxides depends on the stoichiometry of the mixture. Azens *et al.* (50) showed for mixed cerium titanium oxide that a Ce/Ti ratio above 0.3 gives films optically passive upon lithium insertion which makes them suitable as counter electrode for an electrochromic device. The kinetics of lithium insertion is also strongly dependent on the Ce/Ti ratio as shown by Keomany *et al.* (51). They described the TiO_2-CeO_2 films as a matrix of TiO_2 with some crystallites of CeO_2 where TiO_2 improves the diffusion of lithium ions and CeO_2 improves the insertion capacity of the film.

The effect of the stoichiometry on vanadium titanium films was studied by Burdis (16). He showed that films containing higher vanadium concentration had higher charge capacity but the stability of the film increased with the titanium concentration. In this work, the attention was focused on vanadium titanium mixed oxide with a V/Ti ratio of 1.

Finally, transparent electrical conductors are also used as counter electrode for the electrochromic devices (52).

1.8. Theory of insertion materials.

1.8.1. Principle of insertion electrodes.

An insertion material is a solid composed of atoms or molecules called host molecules capable of intercalating atoms or molecules called guest molecules. The interesting properties of this material are the possibility for the guest atoms to enter or leave the host molecule and to move in the framework of the host molecule. The concentration of the guest atoms in the framework can vary and the variation of this concentration is accompanied by a variation of the electrochemical potential of the host. This property of the insertion material is used in electrochemical devices such as Li^+-ion battery, solid state sensors and electrochromic devices. The insertion of the guest in the host structure can create a distortion of the structure. In the case of crystalline materials, the intercalation of the guest can create new phases. If the modifications are too important, the insertion can become irreversible, which would cause a device failure. The insertion can induce a modification of the host structure. The dimension of the host structure, that is, the dimension ion that the guest can move, is a very important characteristic of the material. Schollhorn (53) distinguishes between three categories represented on figure 1-3.

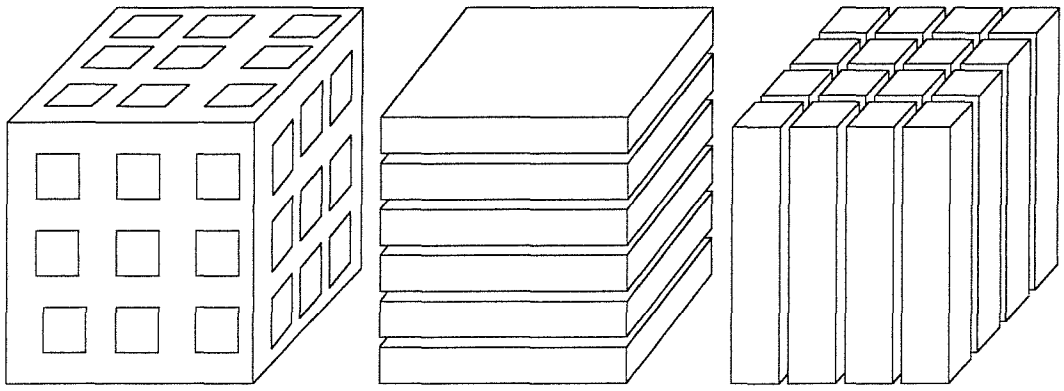

Figure 1-3: Schematic view of the three different type of host structure.

Figure 1-3-a shows the schematic view of three-dimensional compounds where the guest can be inserted and move in the three dimensions. This is the structure of transition metal oxide.

The structure of bidimensional or lamellar structure is shown in figure 1-3-b. The most well known compounds with this structure are graphite, dichalcogenides (i.e. TiS_2) and dihydroxides of transition metal. The planes, in between which the insertion occurs, are linked together by Van der Waals forces. These can intercalate molecules bigger than the distance between the planes such as macromolecules. They make very good material for lithium ion battery (54).

Monodimensional structure is shown in figure 1-3-c. It consists of polyhedral chains orientated in one crystallographic direction. An example of compounds with this structure is MoS_3 (55).The link between the chains is very weak and the insertion stoichiometry can be very high (i.e. 4 Li^+ per MoS_3) but quickly leads to an amorphous structure.

Guests can be monovalent cations or divalent cations or even organic molecules but the most studied cases are insertion/extraction of protons and lithium ions. This is due to their size and their ability to insert and diffuse in the host structure in large quantities.

1.8.2. Atomic and electronic structure of the electrodes studied.

In this work, the materials studied are transition metal oxides. These materials are WO_3 used as electrochromic electrode and vanadium-titanium oxide as the counter electrode. Granqvist (56) has presented a unified view of the electrochromic properties of transition metal oxides using band diagrams based on the fact that most crystalline metal oxides showing electrochromism are based on MeO_6 octahedra connected by corner sharing, edge sharing or a mixture of both.

Electrochromism is associated with a cation insertion represented by the equation:

$$MO_n + xI^+ + x\,e^- \rightarrow I_xMO_n$$

Where M is a transition metal, I^+ is a singly charged small cation such as H^+ or Li^+, e^- is an electron and n depends on the oxide. For example, n is 3 for defect perovskite, 2 for rutile, 1.5 for carborundums and 1 for rock salts.

WO_3 is of perovskite type and tetragonal, orthorhombic, monoclinic(figure 1-4) and cubic symmetry can be found depending on the temperature.

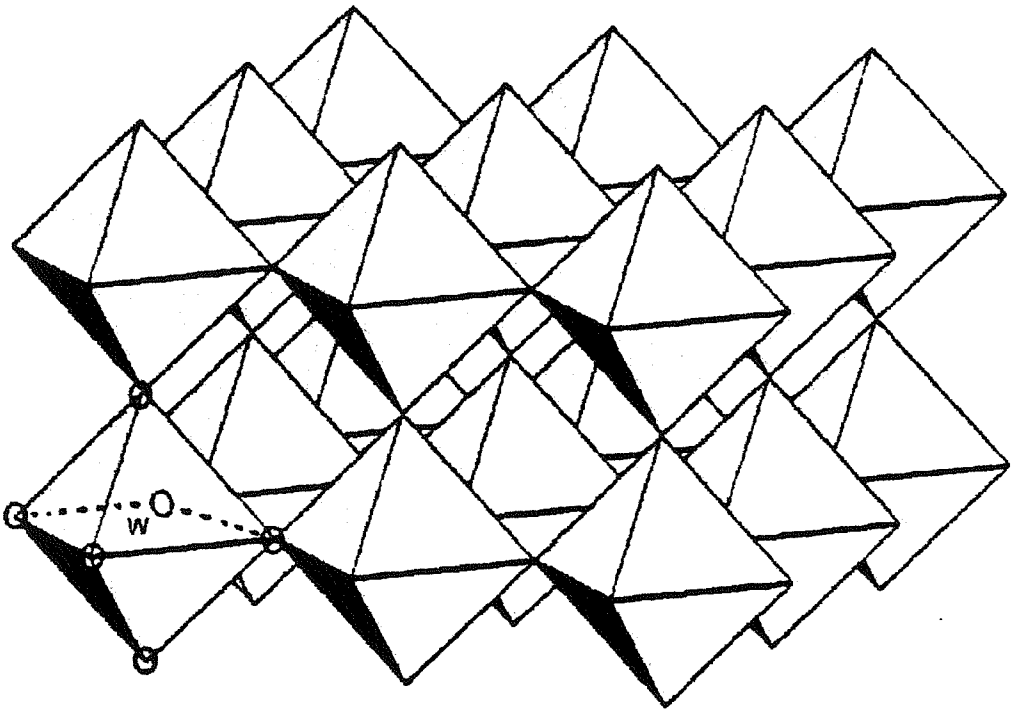

Figure 1-4: Octahedral structure of WO_3 monoclinic.

WO_3 has also the tendency to form sub-stoichiometric phases with edge sharing octahedra and extended tunnels with large pentagonal or hexagonal cross sections. It is possible to form tungsten oxide with pyrochlore (figure 1-5) and hexagonal (figure 1-6) structures. The diffusion of lithium will be favoured by the presence of the channels.

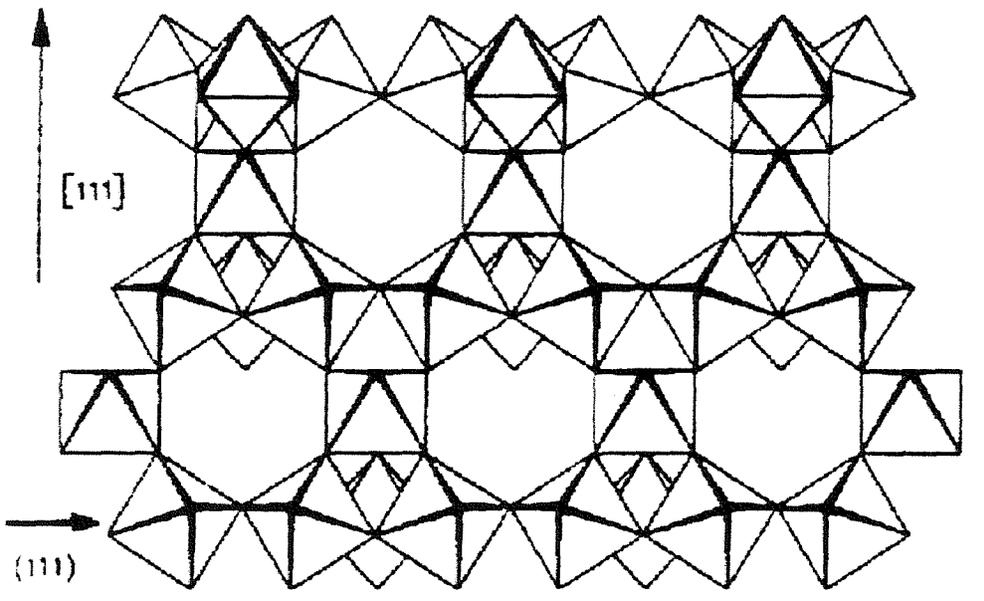

Figure 1-5: Pyrochlore WO_3.

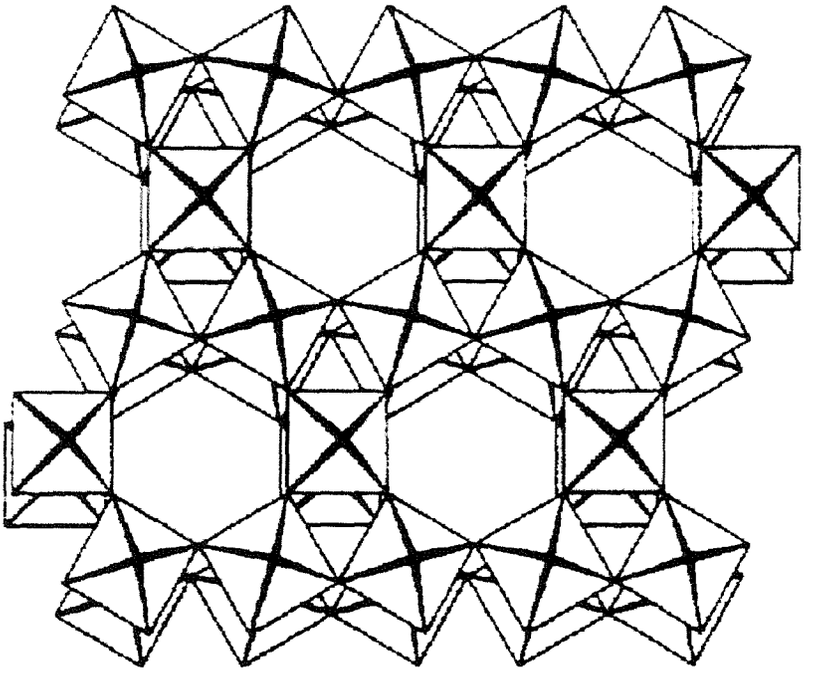

Figure 1-6: Hexagonal WO_3.

For TiO_2, the basic building block is TiO_6 octahedron whatever the structure. TiO_2 can have the anatase structure (thermodynamically more stable), or the rutile structure. The anatase phase is the most attractive for electrochromism as it shows pronounced cathodic electrochromism. It consists of infinite planar double chains of TiO_6 distorted octahedra. The rutile phase can be described as a hexagonal close pack oxygen lattice with octahedrally coordinated metal ions forming edge share infinite chains.

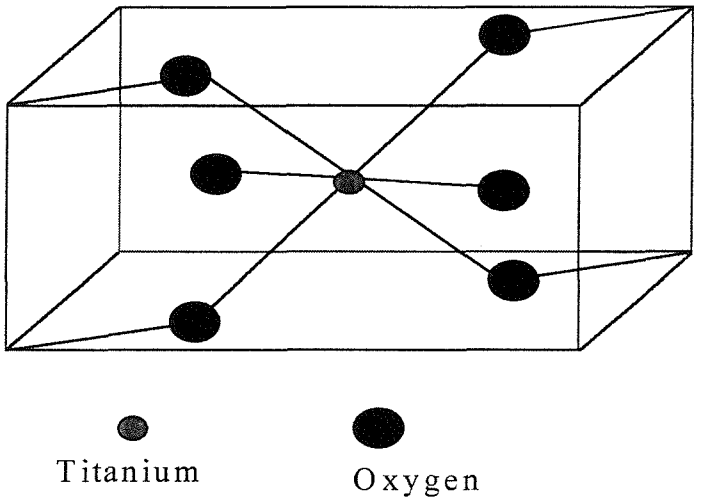

Figure 1-7: Rutile TiO_2.

V_2O_5 can be described as irregular VO_6 octahedra: the V-O distances are 0.159 and 0.202 nm for five of the bonds and 0.279 for the sixth bond. The structure is orthorhombic with the large separation along the crystallographic c direction. The octahedra are linked together by one face as shown on figure 1-8. They can also be described as square pyramidal VO_5 units organised in layers about 0.44 nm apart. Lithium ions are inserted between the layers and are co-ordinated by oxygen between the layers of VO_5 pyramids.

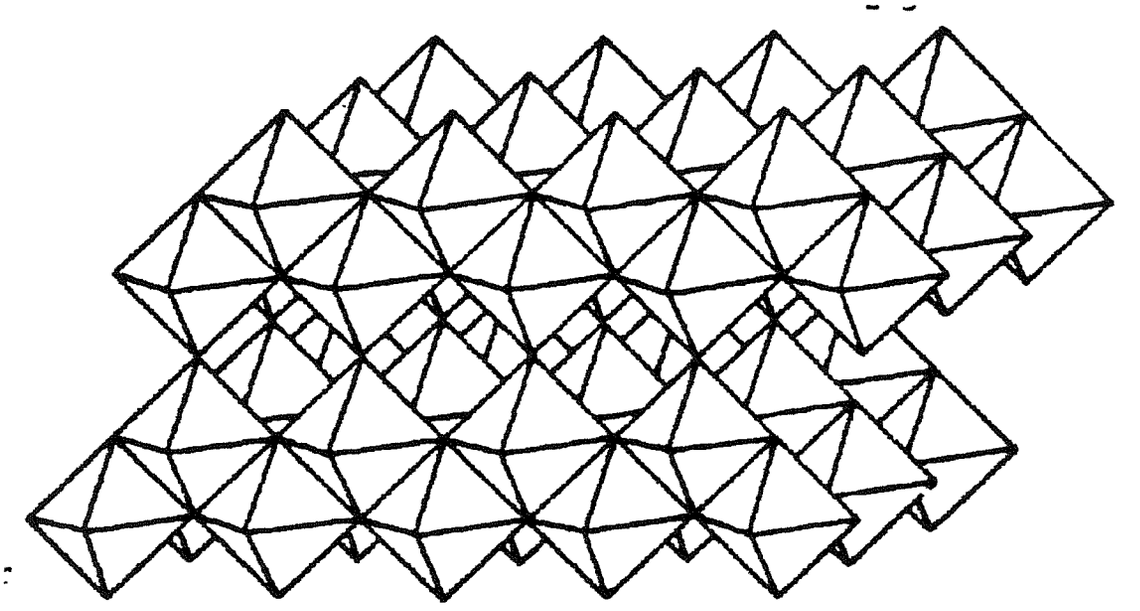

Figure 1-8: Lamellar structure of V_2O_5 distorted octahedra.

The electrical and optical properties of the oxides described above are affected by the simultaneous insertion of electrons and ions. The insertion of electrons changes the band diagram of the host material. Thus the main concern in electrochromic material is the insertion of electrons that modify the electronic structure of the host material and the ion is used for the charge balance although the insertion of the ion determine the switching time of the electrode. Thus it is interesting to look at the band structure of the oxide studied. Granqvist's paper on the subject gives details of the band structure of most well known electrochromic oxides (56).

In the metal oxide lattice, p orbitals from the oxygen overlap with s, p and d orbitals of the metal to form bonding and anti-bonding levels. The overlapping depends on the effective nuclear charge and on the orientation of the orbitals determined by the crystal structure. In the structure, each metal ion is octahedrally surrounded by 6 oxygen ions and each oxygen is linearly surrounded by two metals ions. As a consequence, the d level splits into e_g and t_{2g} levels. The splitting arises because the e_g orbitals point directly at the electronegative O whereas the t_{2g} point away from the nearest neighbours into empty space. Similarly the 2p orbital of the oxygen split into $2p_\sigma$ orbitals pointing at the nearest electropositive Me ions and $2p_\pi$ orbitals pointing at empty space. Figure 1-9 shows the band diagrams of WO_3, TiO_2 and V_2O_5.

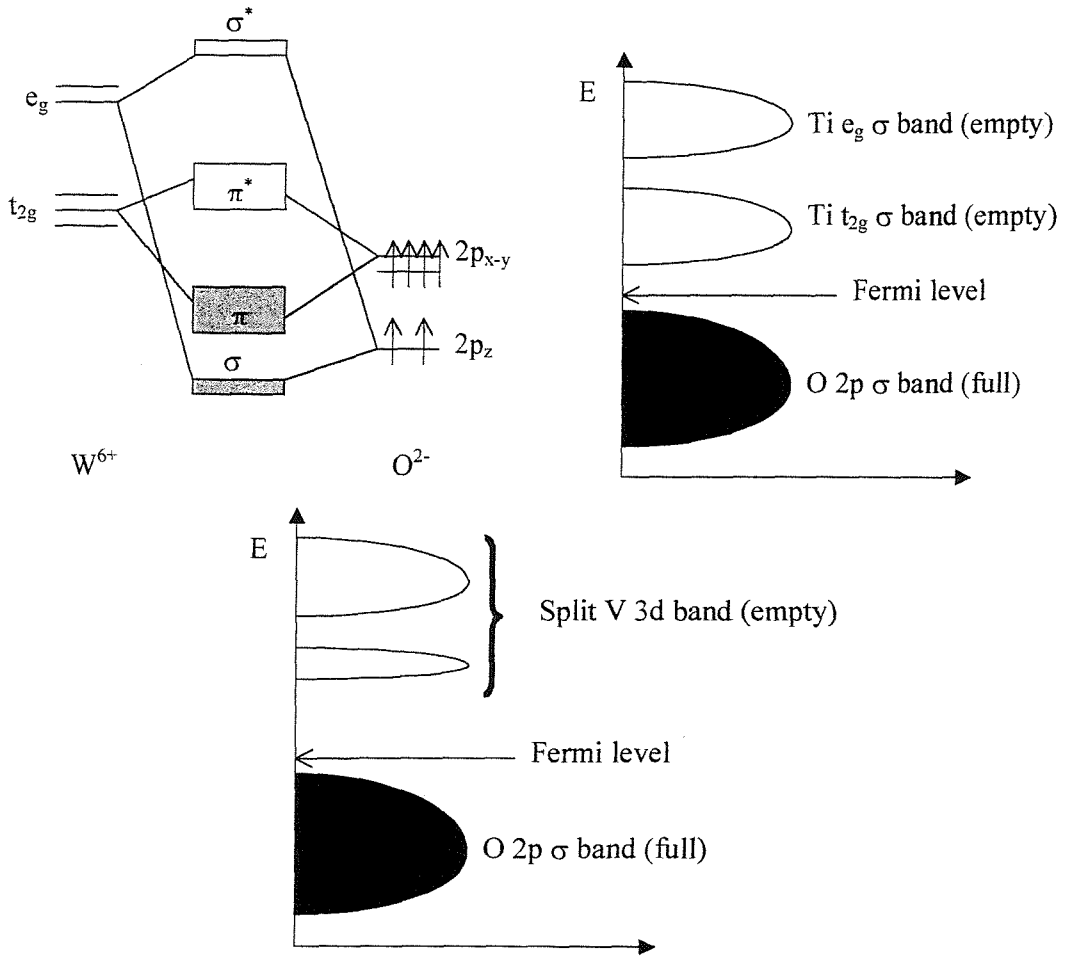

Figure 1-9: Band diagrams of WO_3, TiO_2 and V_2O_5.

In the case of tungsten oxide, the t_{2g} orbitals of the tungsten overlap with the $2p_x$ and $2p_y$ orbitals to form a band that can contain 6 electrons, In WO_3 (W^{6+}, d^0) this band is empty and the Fermi level lies between the π and π^* bands. The band gap is wide enough for the material to be transparent. When ions and electrons are inserted, the excess of electrons must occupy the π^* band. The material can transform from transparent to absorbing or reflecting depending on whether the electrons occupy localised or extended states. When the electrons and ions are extracted, the material returns to its original state. The Fermi level is assumed to be pushed up.

The case of TiO_2 is very similar to the case of WO_3. The d_{xy} orbital points along the metal-metal axis but the band formed by the overlap of this orbital is empty as Ti is in a +4 state. The band gap is between the O 2p and the Ti t_{2g} bands. TiO_2 is a white

insulator in thin film form. On insertion, the electron must enter the Ti t_{2g} band and an absorbing state is obtained.

The electronic structures are more complicated for V_2O_5 because of its layer structure. However, it can be described as a filled O 2p band separated from the V 3d band with a split-off lower portion. This band splitting is characteristic of layered structures. Thus it is reasonable to expect very complicated electrochromic behaviour for V_2O_5.

1.8.3. Chromic mechanism in amorphous tungsten oxide.

The previous models are good for a crystalline material as they are based on the presence of MeO_6 octahedra. The mechanism of electrochromism in tungsten oxide is still subject to discussion usually dependent on the structure, amorphous or crystalline, of a thin layer of tungsten oxide. The limit between crystalline state and the amorphous state is also subject to discussion. But, amorphous tungsten oxide is usually described as a material in which the order does not exceed 50 Å. Such a material gives no define X-ray diffraction spectrum or electron diffraction spectrum. The short order structure of tungsten oxide seems to be dependent on the deposition structure. Arnoldussen (57) described WO_3 prepared by evaporation as a molecular solid constituted by W_3O_9 linked together by water molecules. Another structure made of WO_6 octahedra linked together by a corner was also proposed for tungsten oxide prepared by the same technique and by cathodic pulverisation (58) and also by thermal decomposition of tungsten alkoxides (59).Finally, on samples deposited by evaporation, Green (60) showed the existence of grains of 50 Å diameter constituted of tetragonal WO_3.

The first explanation of electrochromic effect in tungsten oxide was given by Deb (5) who attributed the coloration to the formation of F centres due to the sub-stoechiometry in oxygen of the oxide obtained by evaporation. But this explanation can not explain the high optical densities observed on some tungsten bronzes. Two explanations are now proposed, both based on the fact that the electron is localised near a tungsten atom.

- Intervalence transfer model:

Faughnan *et al.* (61) attributed the coloration to an electronic transfer between two neighbour sites W^{5+} and W^{6+} as shown below:

$$W_A^{5+} + W_B^{6+} \xrightarrow{h\nu} W_A^{6+} + W_B^{5+}$$

This transfer is possible because of the overlapping of the tungsten 5d orbitals to which the electrons belong.

- Small polaron model:

For Schirmer *et al.* (62), the optical absorption may be due to the formation of a small polaron, result of the electron-phonon interaction between the electron inserted and the surrounding network. Because of the amorphous structure of the host material, the local changes of potential of the 5d electrons can trap the electron on a tungsten site. The localised electron then interacts with a phonon from the lattice to form a small polaron.

Both models imply the formation of absorbing centres and are in good agreement with the optical properties of amorphous tungsten bronzes M_xWO_3 that were shown to be absorbing and non-reflecting in the near infra red region. The variation of their optical density vs. the insertion ratio can be written as Beer Lambert law:

$$DO(\lambda) = \varepsilon(\lambda)\, l\, c$$

Where $\varepsilon(\lambda)$ is the molar absorption coefficient of the bronze at the wavelength λ,

l is the thickness of the tungsten oxide layer,

ε is the average molar concentration of absorbing centres (proportional to the insertion ratio).

In a more recent paper, Bechinger *et al.* (63)came back to this model and found that they can not explain all the experimental results. The double charge insertion model can not account for the photochromic coloration seen for tungsten oxide. The properties of colour centres in tungsten oxide are very similar whether they are formed by photochromic or electrochromic coloration although in the case of photochromic coloration, an external injection of charges can be ruled out. This observation raises the question as to whether it is possible to find a mechanism that works for both coloration processes. Both the electrochromic and the photochromic efficiencies decrease with decreasing oxygen deficiency. This phenomenon can not be explained by the model described before. The authors found that the virgin tungsten

oxide may be considered mainly as a mixture of W^{4+} and W^{6+} and W^{4+} states increase with increasing oxygen deficiency. When injecting charge, the number of W^{5+} states increases. So the authors proposed a mechanism where the intervalence transfer occur between W^{5+} and W^{4+} states. This model also explains the importance of oxygen deficiency for photochromic efficiency.

1.8.4. Thermodynamics of insertion.

For an electrochemical reaction, the electromotive force of the cell is directly proportional to the Gibbs free energy , G, of the reaction:

$$\Delta G = -nFE$$

In the case of insertion electrodes, G changes with the number of inserted ions, n. These changes are described by the chemical potential μ. In the case of Li^+ insertion that we are studying, the chemical potential of the lithium ion can be written:

$$\mu_{Li} = \left(\frac{\partial G}{\partial n_{Li}}\right)_{T,P,n}$$

Thus at the equilibrium i.e. no current is flowing, and $\partial n \to 0$, if E is measured with respect to the Li/Li^+ reference electrode and n=1 (as we only have one electron transfer for each Li^+ inserted) we have:

$$\mu_{Li} = \left(\frac{\partial G}{\partial n_{Li}}\right) = \Delta G = -nFE \Rightarrow E = -\frac{\mu_{Li}}{F}$$

where μ_{Li} is the chemical potential of the inserted lithium. This is equal to the sum of the chemical potentials of the inserted ions and the associated electrons.

$$\mu_{Li} = \mu_{(Li^+,e^-)} = \mu_{Li^+} + \mu_{e^-}$$

where μ_{e^-} = constant + Fermi level.

In the case of a single non-stoichiometric insertion phase in which the insertion sites are of equal energy there are two limiting cases depending whether the chemical potential is only dependent on the electronic term or on the ionic term. The insertion can be limited by the total number of sites available for the ion or the number of electron that can be injected. If the insertion is limited by the number of electron injected, the Fermi level is dependent on the degree of insertion and if we assume that there is an empty electronic band of a constant width, we can define a dimensionless quantity as:

$$x_{el} = \frac{y}{y_{\max}}$$

If the insertion is limited by the number of sites available for the lithium ions and the density of states is high near the Fermi level then we can define the quantity:

$$x_{ion} = \frac{y}{y_{\max}}$$

For both cases, the chemical potential will have the same expression:

$$\mu_{Li} = \mu^{0}_{Li,host} + RT\ln\left(\frac{x}{1-x}\right)$$

where x= x_{el} or x_{ion} and $\mu_{Li} = \mu^{0}_{Li,host}$ when x=0.5.

We can then find the expression of the potential as a function of the insertion ratio:

$$E = -\frac{\mu^{0}_{Li,host}}{F} - \frac{RT}{F}\ln\left(\frac{x}{1-x}\right)$$

A typical value of $-\mu^{0}_{Li,host}/F$ = 3.0 V *vs.* Li/Li^{+} at x=0.5 can be measured for transition metal oxide at room temperature. We can then plot a theoretical curve for a single non-stoichiometric phase (figure 1-10).

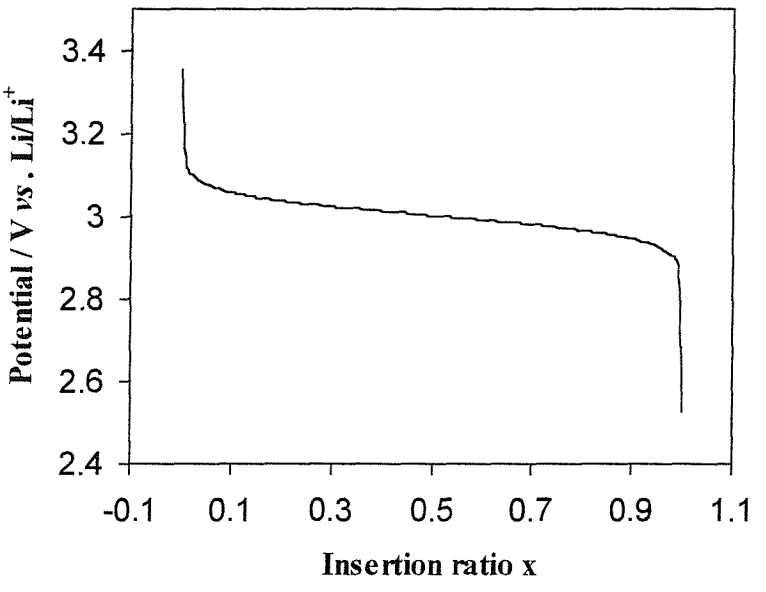

Figure 1-10: Theoretical E *vs.* x curve corresponding to the equation above.

The above equation shows a simplified view where the dominant term is either electronic or ionic. In reality, both terms contribute and they are affected by a third term taking into account the ion-ion interaction in the host. Armand (64) proposed a model taking into account this ion-ion interaction:

$$E = -\frac{\mu^{0}_{Li,host}}{F} - \frac{zx_{ion}E_{Li-Li}}{F} - \frac{nRT}{F}\ln\left(\frac{x_{ion}}{1-x_{ion}}\right)$$

where z is the lithium coordination number, $E_{Li\text{-}Li}$ is the ionic repulsion energy and n is equal to 1 or 2 depending whether the limitation depends on one of the factors (ionic or electronic) or on both factors. The interaction between the ion is assumed to have a linear dependence on x_{ion}.

The previous equation is often written as:

$$E = E^{\Theta} - kx - \frac{RT}{nF}\ln\left(\frac{x}{1-x}\right)$$

where E^{Θ} is the potential at half charge and – kx represents the ion-ion repulsion.

As seen earlier for tungsten oxide, many insertion materials have more than one phase. Phases can exist over a narrow composition range and the pure phase regions are separated by mixture of two phases. This existence of the mixture of two phases, the chemical potential of lithium must be the same in both phases. This implies that the potential will stay constant over the position range where both phases exist simultaneously. This phenomenon has an importance for the battery electrodes. A theoretical curve for a three-phase system is shown on figure 1-11.

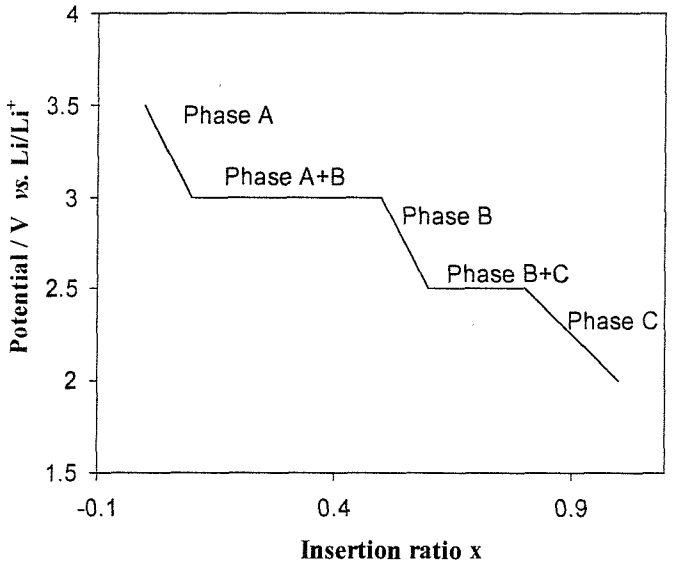

Figure 1-11: Theoretical E *vs.* x curve for a three-phase system.

A very common feature of the potential *vs.* insertion ratio curve is the hysteresis. Hysteresis is the difference between the insertion and the extraction curve. The potential measured for a given value of x is higher in the extraction curve than in the insertion curve (cf. Figure 1-12). Normally, the energy dissipated in a cell is proportional to the square of the current but the overpotential is proportional to the current. In insertion materials, the moving of domain boundaries can produce hysteresis where the overpotential is independent of the current.

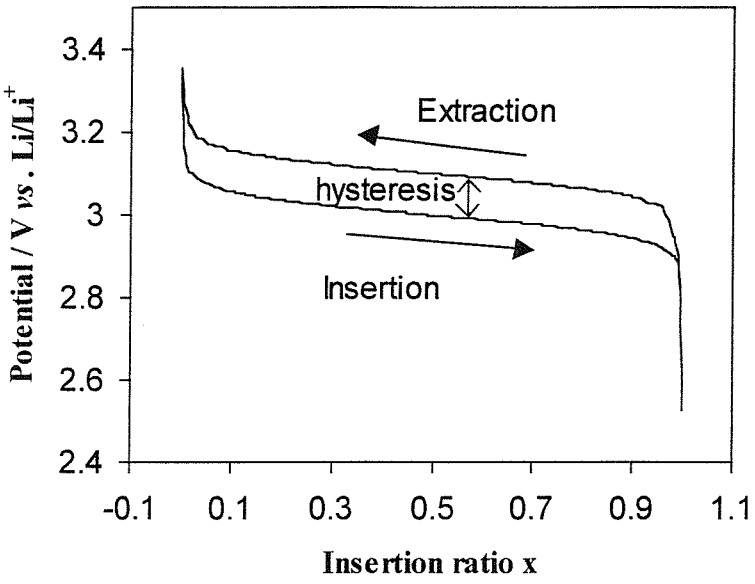

Figure 1-12: Theoretical potential *vs.* insertion ratio curve showing hysteresis.

1.8.5 Kinetics of insertion.

All the equations given above are only correct for the interface between the material and the ion conductor at equilibrium. To have equations correct for the bulk conditions of the electrode we must take into account the mass transport of the ion in the host material. The mass transport of the ion in the host structure will depend on a few parameters. The ion insertion is accompanied by an electron injection in the material as described before. The electron is also moving in the host structure and the diffusion of the electron can interfere with the diffusion of the ion. Crandall and Faughnan (65) first gave a model on the kinetics of insertion of protons in tungsten oxide. They performed measurements of the diffusion coefficient of the electrons and obtained a value of about 10^{-3} $cm^2.s^{-1}$. This value is to compare with the value of the diffusion of lithium in tungsten oxide, which is typically of the order of 10^{-11} $cm^2.s^{-1}$. This shows that we can assume that the electron transport is much faster than the ion transport in the oxide. Therefore, we can consider the transport of lithium as the rate-limiting step. We also consider a on dimension diffusion, perpendicular to the surface of the electrode. This direction is called x.

Ficks first law gives the relationship between the surface concentration and bulk concentration:

$$J_{Li} = -D\frac{\partial c_{Li}}{\partial x}$$

with J is the flux and I = zFJ. This equation is replaced by the Nernst-Planck equation when the system studied is concerned with solid state diffusion:

$$J_{Li} = -c_{Li} b_{Li} \frac{\partial \overline{\mu}_{Li}}{\partial x}$$

where $\overline{\mu}_{Li} = \mu_{Li^+} + zF\Phi$

$\overline{\mu}_{Li}$ is the electrochemical potential of the ion,

b_{Li} is the mobility of the ion,

c_{Li} is the concentration of Li^+ ion

μ_{Li^+} is the chemical potential of Li^+ ions.

and Φ is the electric field gradient.

However, the earlier assumption means that the electric field gradient is zero, Thus:

$$J_{Li} = -c_{Li} b_{Li} \frac{\partial \mu_{li}}{\partial x}$$

The chemical potential can be expressed as:

$$\mu_{Li} = \mu_{Li}^0 + RT \ln a_{Li}$$

where a_{Li} is the activity of the lithium ion.

By differenciation:

$$\frac{\partial \mu_{Li}}{\partial x} = RT\frac{\partial \ln a_{Li}}{\partial x} = RT\frac{\partial \ln a_{Li}}{\partial c_{Li}}\frac{\partial c_{Li}}{\partial x} = \frac{RT}{c_{Li}}\frac{\partial \ln a_{Li}}{\partial \ln c_{Li}}\frac{\partial c_{Li}}{\partial x}$$

$$J_{Li} = -RTb_{Li}\frac{\partial \ln a_{Li}}{\partial \ln c_{Li}}\frac{\partial c_{Li}}{\partial x}$$

Substituting into Ficks equation we have:

$$D = RTb_{Li}\frac{\partial \ln a_{Li}}{\partial \ln c_{Li}}$$

This is the expression of the diffusion coefficient obtained when we consider that the diffusion of the ion is the rate-determining step.

The expression $\frac{\partial \ln a_{Li}}{\partial \ln c_{Li}}$ is known as the thermodynamic enhancement factor. In the case of an ideal solution, the concentration of the ion is equal to its activity and this factor becomes 1 giving a diffusion coefficient of:

$$D=RTb_{Li}$$

This is called Nernst-Einstein relationship.

For all the equations given above, we assume that the diffusion of the ion is the rate-limiting step. Some authors give other models. For example, Crandall et al. (65) or Mohapatra (66) assumed that the kinetics are limited by the charge transfer reaction at the interface insertion material / electrolyte. Other models assume that the charge transfer reaction is the limiting factor at short time and the diffusion of the ion becomes the limiting step at longer time (67). We will not detail all these models.

1.8.6. Summary.

In section 1.8, we have seen that the properties of the materials depend on their electronic and molecular structure.

Solid state electrochemistry is different from solution electrochemistry and the main difference is the very slow diffusion rate observed in solid state chemistry. This means that the techniques used must take into account this slow rate i.e. slow scan cyclic voltammetry.

1.9. *Stability of metal oxides.*

Generally, metal oxides are stable to reversible insertion of lithium. But there are some circumstances where reversibility of lithium insertion is poor:

- when the insertion of lithium induces changes in the lattice structure.
- if soluble products are formed.

For example, it was shown that indium tin oxide (ITO) and fluorine doped tin oxide (FTO) irreversibly insert lithium in small quantities below 2.5 V *vs.* Li/Li^+ (9) and in large quantities below 2 V. This property can be important in our study as ITO and FTO are used as electronic conductive layer for the electrochromic devices.

Metal oxides are used as electrode materials in both electrochromic devices and batteries. In both applications, the stability of this oxide is a very important factor for the lifetime of the device. But, it is perhaps a more important factor for electrochromic applications. Secondary batteries are required 1000 cycles in their lifetime. In contrast, electrochromic devices are required to switch a few times a day for 15 or 20 years lifetime corresponding to 10^5 cycles.

Every transition metal oxide can be reduced under some conditions dependent on the voltage range. The electrochemical work is to define the potential range suitable for the oxide. For the electrochromic electrode, the voltage range is determined by the colouring requirements e.g. a fast colouring will require a large overpotential. For the counter electrode, the potential range is extended to achieve high capacities. A compromise between high capacity and high stability needs to be reached.

Authors working on lithium ion batteries have been studying the capacity fading of their cell and have tried to explain that phenomenon.

Amatucci *et al.* (68) have studied a $LiCoO_2$/ $LiPF_6$, 2EC:DMC/ Li cell using a configuration which minimised the electrolyte volume (69). After cycling 25 times from 3 V to 4.5 V *vs.* Li/Li^+, the cell was disassembled and the lithium anode surface was analysed both qualitatively by Energy Dispersive Spectroscopy (EDS) and quantitatively by Atomic Absorption Spectroscopy (AAS). The authors showed that,

above 4.2 V *vs.* Li/Li^+, the cobalt was dissolved and deposited on the lithium surface. Quantitative analysis revealed a linear relationship between the capacity loss and the cobalt dissolution from the cathode.

Using a $Li/LiClO_4$, PC:DME/ $Li_xMn_2O_4$ cell, Jang *et al.* (70) found a similar result. The charge/ discharge cycling was performed galvanostatically at 1 $mA.cm^{-2}$. To avoid Mn deposition on the lithium anode and reference electrode, these electrodes were isolated from the cathode. The electrolyte was analysed by differential pulse polarography to determine the Mn^{2+} concentration. Their results demonstrated the dissolution of manganese and showed that the manganese ion concentration increased with repeating cycling.

These results led us to suspect that metal dissolution may occur with the metal oxides used in the electrochromic cells.

1.10. Electrochemical quartz crystal microbalance study of insertion materials.

Electrochemical quartz crystal microbalance (EQCM) is a very powerful technique to monitor the change of mass of the electrode during an electrochemical experiment. Buttry and Ward (71) published a review of the applications of quartz crystal microbalance to electrochemistry. Various insertion materials have been studied using EQCM. The first study of tungsten oxide WO_3 using EQCM was carried out by Córdoba de Torresi *et al.* (72). They showed that, in acidic solutions, a dissolution process occurs in parallel with the intercalation of protons. Bohnke *et al.* (73-74) studied the insertion of lithium into tungsten oxide films and showed that at short times, a loss of mass is observed. They explained this loss of mass by the existence of a non-faradaic process involving the expulsion of anions from the electrode surface. After this loss of mass, they observed a gain of mass attributed to the insertion of non-solvated lithium ions in the tungsten oxide layer. Other insertion materials such as manganese dioxide and lithium cobalt oxide were also studied using the EQCM (75-76). All these studies showed that non-solvated lithium ions are the only species inserted and extracted from the insertion material.

1.11. Scope of this work.

In this work, we study both the electrochromic electrode (WO_3) and the counter electrode ($VTiO_x$) using electrochemical and physical techniques.

For the electrochromic and the counter electrodes, the chemical composition is not the only factor influencing the properties of the electrode. The behaviour of the electrode will be affected by:

- the porosity of the structure.
- the adhesion of the thin film to the substrate.
- the crystallinity of the oxide.
- the electrolyte used and the traces of impurities, e.g. acids and bases can be very destructive to thin layers.

Amorphous and crystalline samples of tungsten oxide were studied using slow scan cyclic voltammetry and impedance spectroscopy. The electrode surface before and after cycling was studied using scanning electron microscopy and tungsten trace in the electrolyte is analysed with a spectrophotometric titration technique. UV-visible spectroscopy in situ with the electrochemistry is also used to study the optical changes of the film upon cycling.

Vanadium titanium oxide films were studied using slow scan cyclic voltammetry and electrochemical quartz crystal microbalance.

Chapter 2. Theory of the experimental techniques.

2.12. Cyclic voltammetry.

Cyclic voltammetry consists in sweeping the potential of the working electrode back and forth between two potentials E_1 and E_2 at a constant sweep rate and measuring the current. In our case, the start and end potential are different from E_1 and E_2. The open circuit potential was used as a starting potential. The open circuit potential was around 3.3 V *vs.* Li/Li^+ for the tungsten oxide samples and around 3.5 V *vs.* Li/Li^+ for the vanadium titanium oxide samples. The samples were then cycled down to a potential lower than the open circuit potential to insert lithium, typically 2 V *vs.* Li/Li^+ and lower. The lithium was extracted by cycling the sample up to 4.5 V *vs.* Li/Li^+. Figure 2-1 shows the variation of the potential with the time during the cyclic voltammetry at 0.1 mV/s (sweep rate used in all the experiments).

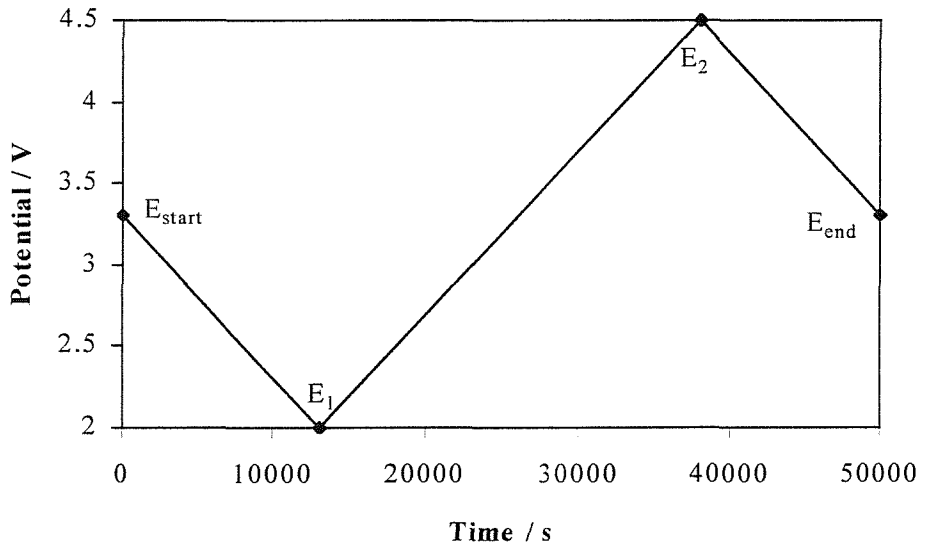

Figure 2-1: Potential *vs.* time during cyclic voltammetry between 2 V and 4.5 V at 0.1 mV/s.

The main difference between solution electrochemistry and solid state electrochemistry is that the interfacial process studied is ion transfer rather than electron transfer. The rate of ion insertion is limited by the diffusion of the ion in the

solid rather than the kinetics of the charge transfer since the diffusion coefficients are generally very small in solids. This means that the scan rate used in solid state electrochemistry should be smaller than the scan rate used in solution electrochemistry. A very slow scan rate helps to distinguished between the different insertion steps (i.e. phase transitions). It also helps to distinguish the currents from the insertion reactions, from the currents from the parasitic reactions.

In this work, slow scan cyclic voltammetry (0.1 mV/s) was performed using a home-built potentiostat piloted by a program written in house in Turbo Pascal.

2.13. AC- impedance spectroscopy.

AC impedance spectroscopy consists in superimposing a small amplitude AC signal on a DC potential. The DC signal is used to set up the surface concentrations and insertion ratio and the AC signal to perturb these conditions. The impedance is the ratio between the applied sinusoidal voltage and the resulting current. The impedance is a complex number that can be written as:

$$Z(\omega) = Z_{\mathrm{Re}}(\omega) + j \cdot Z_{\mathrm{Im}}(\omega)$$

The processes that occur in the electrochemical cell can be modelled using a combination of resistors and capacitors. The equivalent circuit used for thin films is the Randles circuit shown on figure 2-2 where

- R_{el} is the resistance of the electrolyte.
- R_{ct} is the charge transfer resistance.
- Z_w is the Warburg impedance corresponding to the diffusion of the electroactive species.
- C_{dl} is the double layer capacitance.

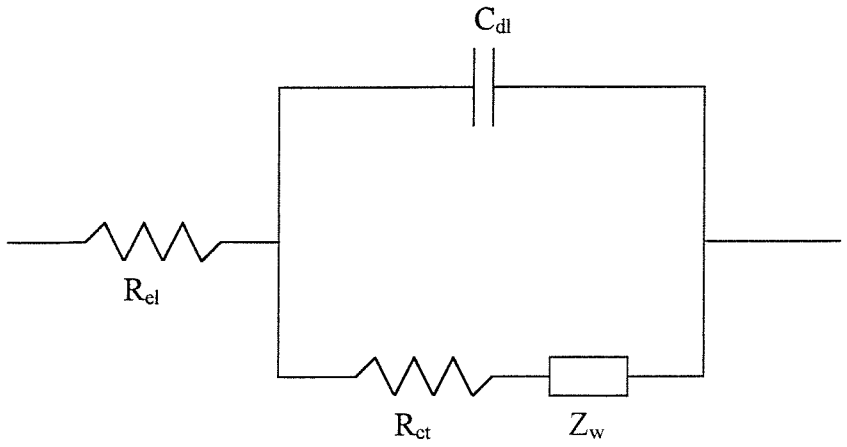

Figure 2-2: Equivalent circuit corresponding to an electrochemical cell.

The impedance is often represented in a Nyquist plot i.e. $-Z_{Im}$ *vs.* Z_{Re} as shown on figure 2-3. The low frequency part of the plot can vary depending on the nature of the diffusion process.

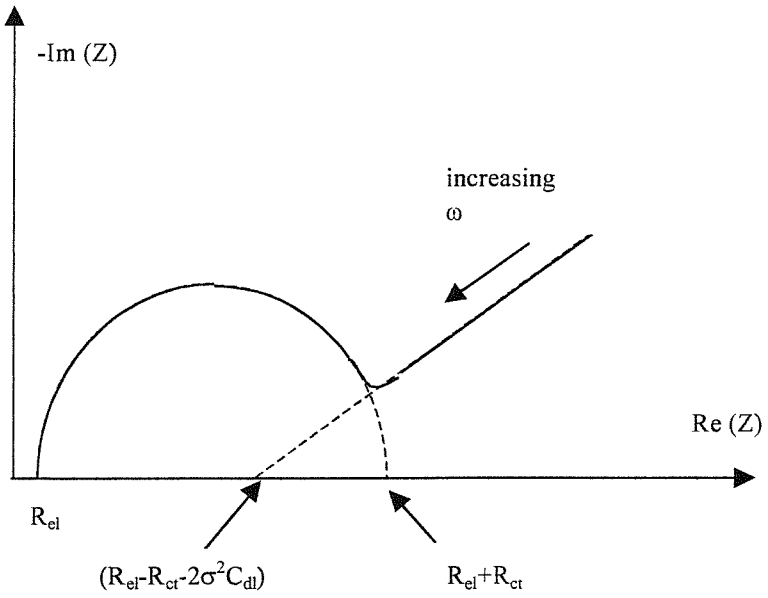

Figure 2-3: Nyquist plot corresponding to the Randles circuit shown in figure 2-2.

The impedance spectroscopy experiments were performed with a Solartron 1250 frequency analyser on a three-electrode cell. The cell was held at a bias potential of 1.6 V and the impedance spectra were recorded as a function of time. Changes in values of Randles parameters are used to monitor any degradation due to applied dc potential.

2.14. Ex-situ physical characterisation.

2.3.1. Scanning electron microscopy.

Scanning electron microscopy (SEM) is widely used to study the surface of conducting or semi-conducting materials. In our study, SEM was used before and after electrochemical conditioning to look at the effect of the insertion-extraction on the surface of the electrodes: change in the surface topography and composition. This technique can only be used ex-situ as the sample has to be studied under vacuum to allow the electron beam to reach the sample. The set-up of the scanning electron microscope is shown on figure 2-4.

An accelerated electron beam (up to 40 kV) is condensed into a spot of a few nanometers diameter, i.e. the probe. The probe is scanned across the specimen while the detector monitors a particular emission, secondary electrons or backscattered electrons.

Low energy, secondary electrons (50 eV) are ejected from the specimen (valence electrons) as a result of inelastic scattering of primary electrons (electrons from the beam). As a result of their low energy, only electrons generated within 5 to 50 nm of the surface will be detected, depending on the material. Since the secondary electrons originate from a region that is only a little larger than the diameter of the probe, they give the signal with the best resolution.
Backscattered electrons are primary electrons that have undergone elastic collisions with the nuclei of the sample atoms. Being more energetic, they will leave the specimen even if they are generated at depth from 100 to 500 nm but the resolution is significantly less than the resolution obtained for a secondary electron image. The energy of backscattered electron varies with the size of the atoms and so they will give some information about the composition.

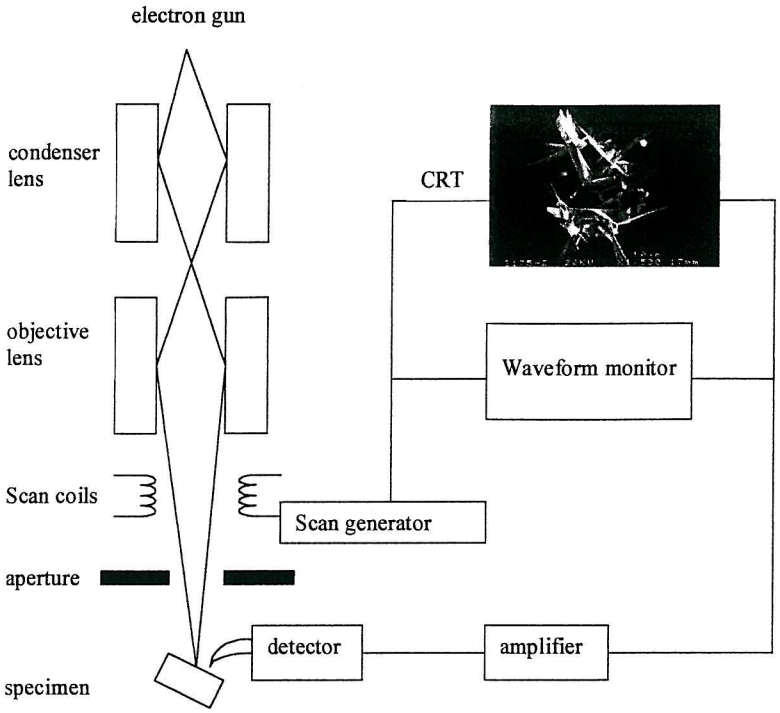

Figure 2-4: Scanning electron microscopy set-up.

2.3.2. Tungsten spectrophotometric titration.

Xu and Parker (77) described a spectrophotometric technique to determine the concentration of tungsten (VI) in solution. The first step of this technique is the reaction of tungsten (VI) with rutin in the presence of cetyltrimethylammonium bromide (CTMAB) in a pH=5 acetate buffer to form a soluble yellow complex. This complex has a maximum absorption at 416 nm. In this work, this technique had two applications.

First, the technique was used to determine the amount of tungsten deposited by sputtering for the amorphous and crystalline tungsten oxide samples studied. First, the tungsten oxide was dissolved off the conducting glass substrate. Amorphous tungsten oxide dissolves very easily in an alkaline solution i.e. sodium hydroxide NaOH (1M). To dissolve crystalline tungsten oxide, sodium hydroxide was used and the solution was heated to 80°C. The solution was then neutralised with concentrated acid. The

solution was then analysed with the technique described above to determine the amount of tungsten present in solution and thus, the amount of tungsten oxide deposited by sputtering.

The second application of this technique was the analysis of the electrolyte and the lithium foil to determine the eventual amount of tungsten dissolved off the electrode. For this, the lithium foil was dissolved in water and the solution neutralized with HCl. The propylene carbonate/ lithium triflate solution was evaporated and the residue dissolved in water. Both solutions were then tested using the CTMAB-rutin reagent.

2.15. In-situ characterisation.

2.4.1. UV-visible spectroscopy.

UV-visible spectrophotometry was performed on a Phillips UV-visible spectrophotometer model PU 8730 to record, in situ, the optical absorbancy (or optical density) of the tungsten oxide electrode during the cyclic voltammetry experiment. The optical density is measured at a constant wavelength (622 nm) corresponding to the maximum change in the tungsten oxide absorption spectrum during the cyclic voltammetry.

2.4.2. Quartz crystal microbalance.

To understand the operation of the quartz crystal microbalance, it is important to understand the piezoelectric effect. The piezoelectric effect is observed on materials that crystallise into non-centrosymmetric space group, for example quartz, rochelle salt ($NaKC_4H_4O_6.4H_2O$) and tourmaline. Mechanical stress applied to the surface of these materials results in an electrical potential proportional to the applied stress across the crystal. The quartz crystal microbalance consists in a thin AT-cut quartz with thin metal pads on each side of the crystal. The pads overlap in the centre of the crystal with tabs expanding from each to the edge of the crystal where electrical contact is made. The terminology "AT" refers to the orientation of the crystal with

respect to its large face. The quartz is made by slicing a quartz rod at an angle of about 35° against the crystallographic x axis.

In an in *situ* electrochemical quartz crystal microbalance experiment, the gold-coated quartz is used to provide the alternating electric field that drives the oscillation of the crystal. It is also used as the working electrode in the electrochemical cell. To supply the alternating electric field, both sides of the crystal are coated with gold layers. The crystal is 1.6 cm in diameter and 0.28 mm thick with a concentric disk gold electrode of 0.2 cm^2 area. The equivalent circuit of the quartz is shown in Figure 2-5. The resonance frequency of the quartz is determined by measuring the admittance of the quartz and fitting the real and imaginary part with the following equations:

$$Y_{real} = \frac{R}{R^2 + \left(L\omega - \frac{1}{C\omega}\right)^2}$$

$$Y_{imag} = C_0\omega - \frac{L\omega - \frac{1}{C\omega}}{R^2 + \left(L\omega - \frac{1}{C\omega}\right)^2}$$

Where $\omega = 2\pi f$ with f the frequency

R: resistance of the equivalent circuit corresponding to the dissipation of the oscillation energy from mounting structures and from the medium surrounding the crystal (e.g. losses induced by the presence of a viscous solution).

L: inductance corresponding to the inertial component of the oscillation.

C: capacitance corresponding to the stored energy of the oscillation and related to the elasticity of the crystal.

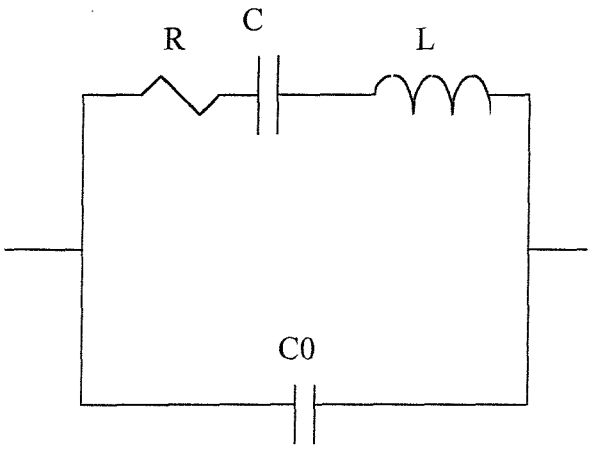

Figure 2-5: Equivalent circuit for the quartz crystal oscillator.

The observed change in the resonance frequency of the quartz Δf is proportional to the mass change of the quartz per unit area Δm according to Sauerbrey equation ():

$$\Delta f = -\Delta m \left[\frac{2\pi f_0^2}{\sqrt{(\rho_q \mu_q)}} \right]$$

Where f_0 is the resonance frequency of the fundamental mode of the quartz.

ρ_q is the density of the quartz.

μ_q is the shear modulus of the quartz.

The principle of the electrochemical quartz crystal microbalance is that a film on the electrode behaves as an added mass of the quartz under some conditions.
The Sauerbrey equation is generally considered accurate so long as the thickness of the film added or taken from the surface is less than 2 % of the quartz crystal thickness i.e. less than 60 μm. The Sauerbrey equation assumes that the material added is perfectly bound to the electrode, that it does not undergo viscoelastic deformation and that the material thickness is uniform over the quartz active area.

Chapter 3. Experimental details.

3.1. Samples preparation.

Various techniques can be used to deposit thin layers of metal oxides (78). Physical deposition techniques can be evaporation and sputtering. Chemical techniques such as the chemical vapour deposition (CVD) and sol-gel-based techniques can also be used. Thin metal oxide films can be deposited electrochemically by electrodeposition and anodisation. In our study, samples were deposited by sputtering. Sputter deposition is a well-established technique used in industry for thin film preparation and can be used for laboratory work as well. Its applicability for coating large areas has made it one of the most widely used vacuum deposition techniques.

Figure 3-1 shows a simplified sputtering set-up. The sputtering technique consists in evaporating atoms from the target to deposit them on the substrate situated just above the target. For this, the chamber is evacuated to a low vacuum of about 10^{-7} Torr (1 Torr corresponds to approximately 130 Pa) before letting a sputter gas into eliminate the impurities. Typically, the sputter gas is a noble gas in particular argon. In this study, metal oxides were deposited from the corresponding metal target so reactive sputtering was used and oxygen was introduced with the argon to form the oxide. The base pressure is then about 10 mTorr in the chamber. Inside the chamber, the target is put to a negative potential opposite to the substrate. Due to the negative potential, electrons are emitted from the target and ionise sputter gas atoms creating a plasma. These ions are then accelerated to the target and eject mostly neutral atoms from the target. The atoms travel to the surface of the substrate where they condense to form the film. The rate of deposition depends on a few parameters: pressure in the chamber, potential applied, argon to oxygen ratio, target to substrate distance, substrate temperature. Simultaneously with the sputtering of atoms from the target, the incident electrons also cause a small amount of secondary electrons to be emitted (79). Those electrons are then accelerated towards the anode and maintain the glow discharge process by ionising sputter gas atoms. About 95% of the energy of the impinging ions is dissipated as heat into the target. Therefore, the target requires a cooling system.

Two types of sputtering can be used. If the cathode is maintain to a constant voltage, the technique is called direct current (DC) sputtering and gives high deposition rates from metal targets. When sputtering from non-conducting targets, the potential of the electrodes is alternated to prevent charging up of the targets. This is called radio frequency (RF) sputtering. RF sputtering is also used during reactive sputtering when the reaction between the gas present and the target is faster than the sputtering reaction.

The partial pressure of oxygen is a very important issue when reactive sputtering is used. If the partial pressure is too low, the oxidation of the metal atoms will be uncompleted. If the partial pressure of oxygen is too high, the metal target will be oxidised and the sputtering power will decrease.

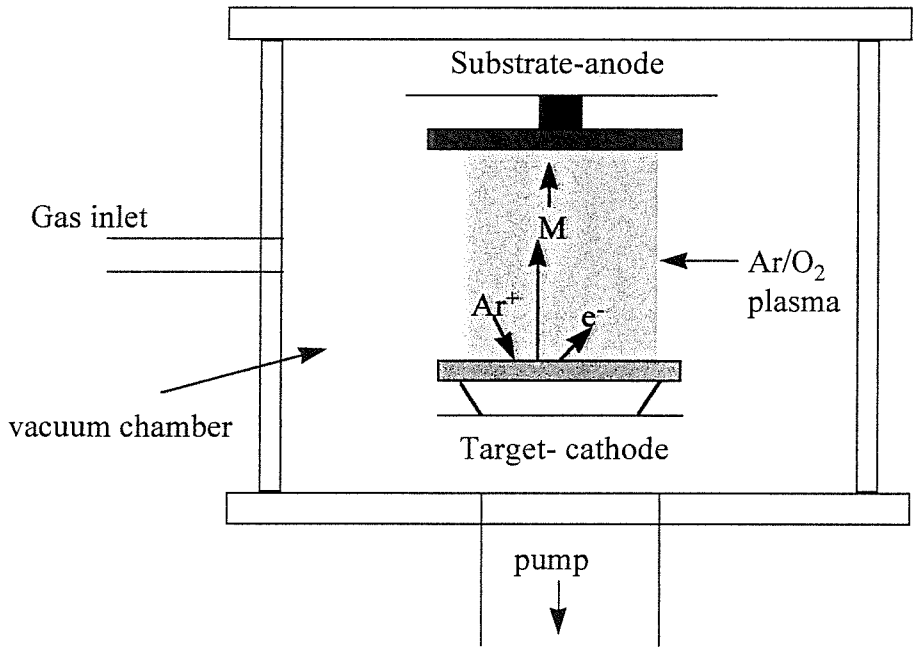

Figure 3-1: Simplified sputtering set-up.

In this study, we used tungsten oxide and mixed vanadium-titanium oxide films.

All the vanadium-titanium oxide films were prepared at Southampton by DC sputtering from a 50/50 vanadium-titanium target in a mixed argon oxygen atmosphere. The argon flow was 40 and the oxygen flow was 40 giving an argon to oxygen ratio of 3 (the mass flow controllers are not the same for the argon and the

oxygen). The voltage applied was 400 V and the current was 1 A for a target area of 200 cm^2.

The tungsten oxide films can be divided into two types: amorphous and crystalline films.

Between the amorphous films we can distinguished three different kind of films:

- The "standard" amorphous samples supplied by Pilkington: DC sputtered from a tungsten oxide target.
- The amorphous tungsten oxide samples from Pilkington sputtered at higher power.
- The amorphous tungsten oxide samples prepared at Southampton: DC sputtered from a tungsten metal target in a mixed argon oxygen atmosphere with various argon to oxygen ratios. The voltage applied was 600 V and the current was 0.5 A for a target area of 200 cm^2..

The crystalline samples were of two types:

- Samples supplied to us by Oxford Brookes University: RF-sputtered from a metal target in a mixed argon-oxygen atmosphere with various argon to oxygen ratios.
- Crystalline samples prepared in Southampton by annealing as-deposited amorphous samples at 400°C for an hour under an oxygen flow.

3.2. Preparation of materials.

3.2.1. Electrode for cyclic voltammetry and UV-visible in situ.

The samples were deposited on various substrates: K-glass (fluorine doped tin oxide coated glass), stainless steel, glassy carbon. It is always very important to avoid the contact between the electrolyte and the substrate; thus polyimide tape was used as a mask to cover the substrate in contact with the electrolyte. This mask had two advantages. First, it avoided the reaction between the electrolyte and the substrate and secondly, it defined the active surface area studied. Usually, the surface studied was

about 0.5 cm^2. At the top of the electrode, a band of substrate was left non-coated to provide a good conduction and covered with silver paint to make a good contact with the crocodile clip as shown on figure 3-2.

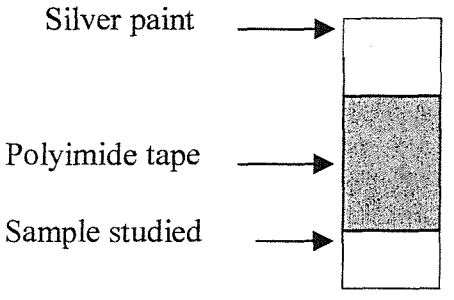

Figure 3-2: schematic view of an electrode used for the cyclic voltammetry and the in situ UV-visible experiments.

For the UV-visible experiment in situ, the only substrate used was K-glass and the active area was increased to make sure that the polyimide tape was not in the path of the beam.

3.2.2. Electrode for the electrochemical quartz crystal microbalance.

Electrochemical quartz crystal microbalance was used to study vanadium titanium oxide ($VTiO_x$). A thin layer of the oxide was sputtered on the circular gold pad of the quartz shown on figure 3-3. The sputtering conditions were the same as the conditions used for the vanadium titanium oxide deposited on K-glass as described earlier. A mask was used to limit the deposition to the gold ring. The quartz was mounted after sputtering and silver paint was used to assure a good contact between the gold tab on the side and the stainless steel.

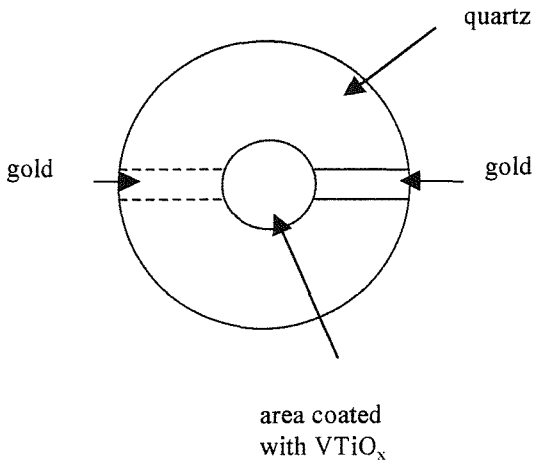

Figure 3-3: Top view of a quartz crystal.

3.2.3. Electrolyte preparation.

The electrolyte used in all the experiments described in this work was a solution of lithium triflate ($LiCF_3SO_3$) (from Fluka) in propylene carbonate (PC) (from Aldrich, 99% purity). The lithium salt was dried under vacuum at 90°C for 24 hours and 140°C for 24 hours. The propylene carbonate was stored over oven-dried molecular sieves and then fractionally distilled. The middle fraction boiling off *circa* 43°C at 0.13 Torr was collected and transfered in the glove box. The salt and the solvent were transferred into the glove box for storage and preparation of the 0.5 M solution to use as the electrolyte.

3.3. Cell construction.

The samples studied were tungsten oxide or vanadium titanium oxide. The working electrodes were prepared as described earlier. All the experiments were done with lithium counter and reference electrodes. The presence of lithium imposes the use of an air and water free cell. In this work, glass cells were used and assembled in a dry box under argon. High vacuum grease was used to provide a good seal.

For the cyclic voltammetry experiment, a three-electrode cell and a two-electrode cell were used. As very slow scan cyclic voltammetry was performed (0.1 mV/s), there is no real need for a three electrode cell: at the slow scan rate used, the current measured is very small and the IR drop is very low and the current can be measured between the reference and the working electrode.

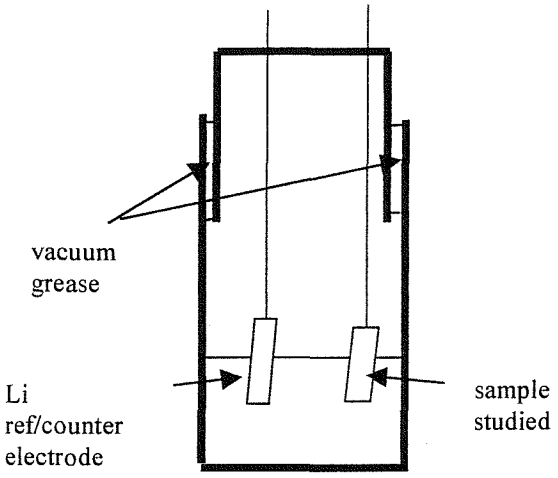

Figure 3-4: Cell design for the cyclic voltammetry experiment.

For the UV-visible spectroscopy experiments, the cell had two quartz windows and the lithium foil situated in a side arm. A two-electrode cell was used.

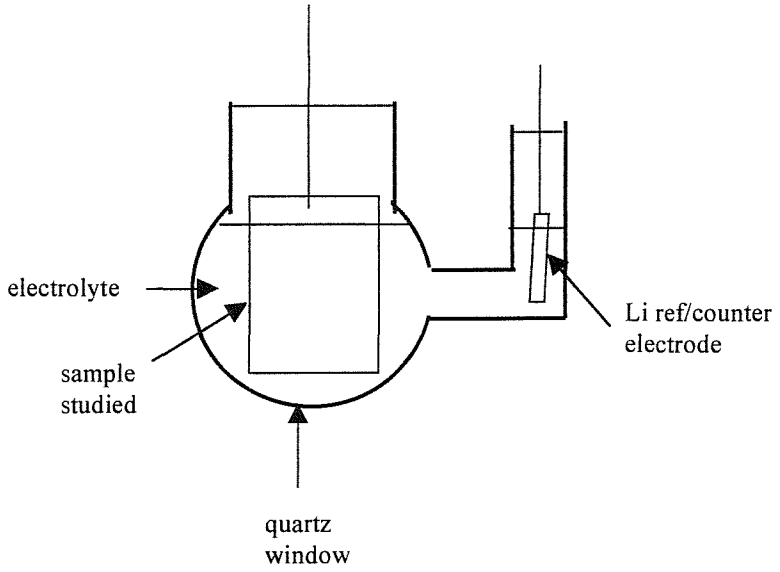

Figure 3-5: cell design for the *in situ* UV-visible spectroscopy experiments.

For the electrochemical quartz crystal microbalance, the working electrode was the coated quartz described earlier. In the design used, the quartz is sitting at the bottom of the cell as shown on figure 3-5. A glass cell sealed with high vacuum grease was used. The quartz crystal microbalance is very sensitive to temperature variations so the cell was thermostated at 30°C by a water circulation system. A viton "o" ring seal was put between the glass and the quartz to avoid leaking. The cell holder was designed so that the cell would go down perpendicularly to the quartz surface to avoid breaking. The coated side of the quartz is used as working electrode and is connected to the potentiostat for the cyclic voltammetry. It is also connected to the impedance analyser to measure the admittance of the quartz and obtain the resonance frequency as shown on figure 3-6.

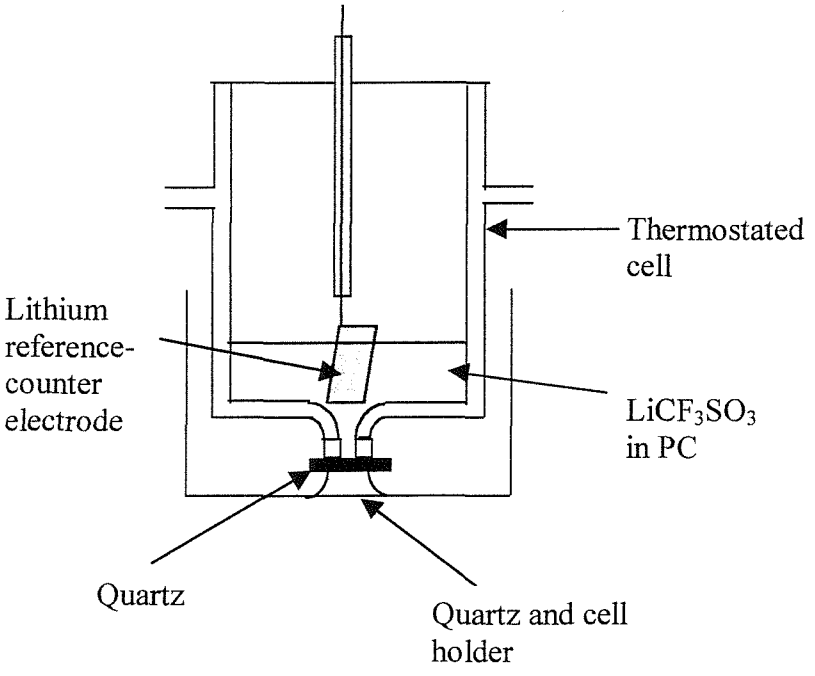

Figure 3-5: EQCM cell design.

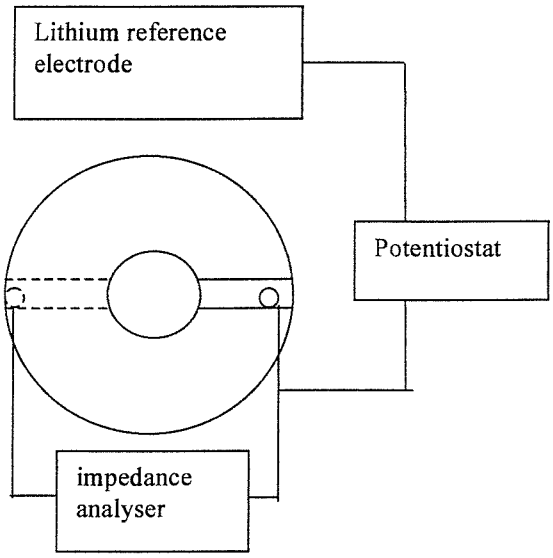

Figure 3-6: Connection of the quartz to the potentiostat and to the impedance analyser.

Chapter 4. Results on tungsten oxide

This aim of this work was to study the stability of these samples and investigate the mechanism of degradation. The stability of an electrochromic device is an important issue. That makes it essential to investigate the stability of all the elements constituting the device. The first element of an electrochromic device is of course, the electrochromic electrode itself. In this study, the electrochromic electrode was a thin layer of tungsten oxide deposited on a conductive glass (glass covered with indium tin oxide (ITO) or fluorine doped tin oxide (FTO)).

Two different types of tungsten oxides were studied in this work: amorphous and crystalline tungsten oxide. Between the amorphous samples, we distinguished three different types of samples:

- The "standard" amorphous WO_3 from Pilkington.
- The samples sputtered at higher power from Pilkington.
- The samples sputtered at Southampton.

The crystalline samples are divided into two types:

- Samples supplied by Oxford Brookes University: sputtered on a heated substrate.
- Prepared at Southampton by annealing amorphous samples after the sputtering.

4.1. Amorphous tungsten oxide.

The samples from Pilkington were deposited by DC-magnetron sputtering from a tungsten oxide target. The exact sputtering conditions for these samples are not known (base pressure, voltage, current, argon flow). The samples prepared at Southampton were deposited by DC magnetron sputtering from a tungsten metal target in a mixed argon-oxygen atmosphere. Details of the sputtering conditions are given later.

The electrochemical stability of the samples was investigated using slow scan cycling voltammetry (0.1 mV/s) to distinguish the side reaction from the insertion reaction (80). The open circuit potential of the cells was about 3.3 V *vs.* Li/Li^+ at the construction. All the samples were studied in the same way. The samples were first cycled between 2 V and 4.5 V *vs.* Li/Li^+. Then they were cycled between 1.6 and 4.5 V *vs.* Li/Li^+ for another 5 cycles.

4.1.1. "Standard" amorphous tungsten oxide from Pilkington.

4.1.1.1. Cyclic voltammetry

Figure 4-1 shows five cycles between 2 and 4.5 V *vs.* Li/Li^+ for a "standard" amorphous tungsten oxide sample from Pilkington. The first cycle shows an extra peak around 2.8 V *vs.* Li/Li^+ in the first insertion half cycle as shown by Burdis *et al.* (81). This peak corresponds to an irreversible charge in the first cycle as shown in the potential *vs.* charge curve on Figure 4-2. As there is no equivalent peak on the anodic scan, the peak is probably due to an irreversible lithiation process. It could be due to oxygen trapped in the oxide layer or to peroxo-bonds:

$$W-O-O-W+2Li^+ + 2e^- \rightarrow 2W-O-Li$$

Although the cyclic voltammograms are superimposable after the first cycle, the potential *vs.* charge curve is shifted towards the cathodic region showing that a parasitic reaction is occurring. This reaction can be:

- Damage of the oxide layer by corrosion.
- Formation of a passivating layer of reaction products.
- Gas evolution that can be limited by minimising the water content of the electrolyte.

In a real device, these parasitic reactions could occur:

- If the device was left in the colouring mode for too long in the case of a galvanostatic switching.
- In the case of a fast switching of the device using a large overpotential.

They could cause the complete and irreversible damage of the device.

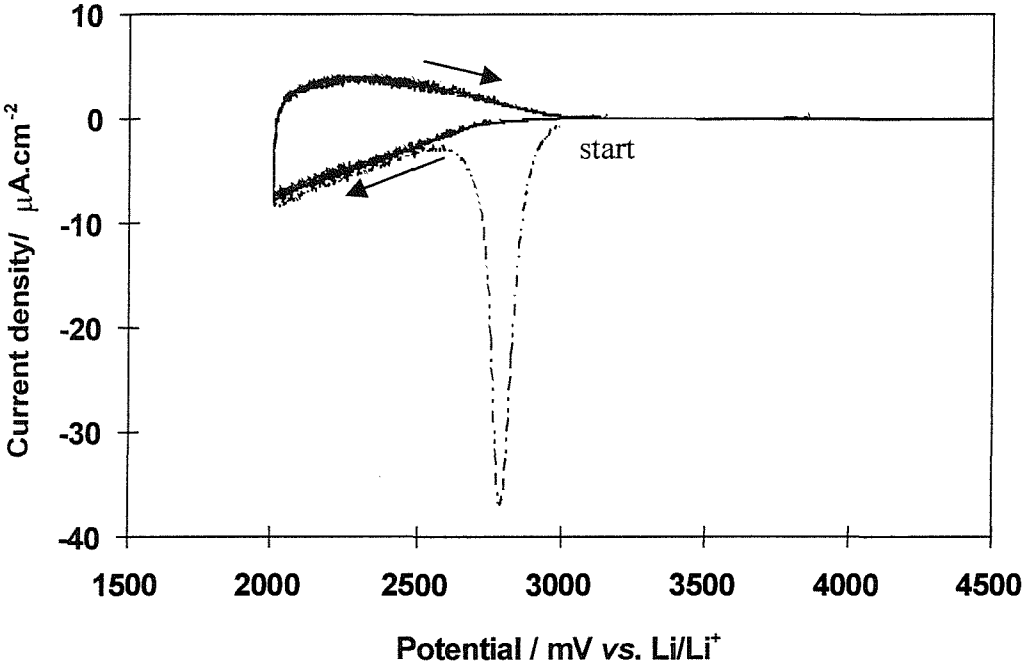

Figure 4-1: Cyclic voltammograms of a standard amorphous tungsten oxide from Pilkington at 0.1 mV/s between 2 V and 4.5 V *vs.* Li/Li^+.

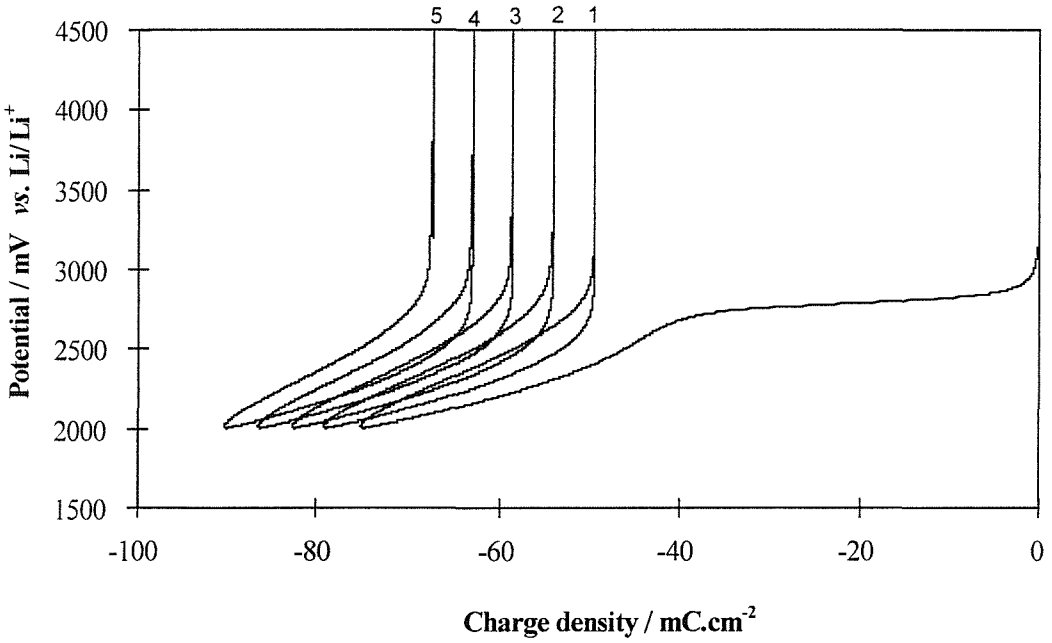

Figure 4-2: Potential *vs.* charge curves corresponding to the cyclic voltammograms on **Figure 4-1**.

To investigate the effect of a large overpotential, which can occur during fast device switching, the sample was then cycled down to 1.6 V vs. Li/Li^+. Again, the scan rate was very slow to allow the side reactions to occur.

Figure 4-3 shows the cyclic voltammogram of the same sample between 1.6 V and 4.5 V *vs.* Li/Li^+ at 0.1 mV/s. The first cycle down to 1.6 V is remarkably superimposable with the 5th cycle of the previous experiment down to 2 V. The current carries on increasing when the sample is cycled down to 1.6 V. A second peak is almost forming at about 1.6 V *vs.* Li/Li^+. Additional charge due to this second peak can also be seen in the extraction half cycle. Even though the 30 $mC.cm^{-2}$ extracted in the 1st cycle down to 1.6 V *vs.* Li/Li^+ is larger than the charge extracted previously, the charge loss is considerable (about 35 $mC.cm^{-2}$), a lot higher than the charge imbalance observed between 2 V and 4.5 V *vs.* Li/Li^+ (about 5$mC.cm^{-2}$) as shown on Figure 4-4. This charge imbalance can be due to an irreversible insertion of lithium. During the subsequent cycles, current and charge decrease dramatically. After 5 cycles, the charge inserted and extracted is only about 5 $mC.cm^{-2}$ corresponding to 10% of the charge exchanged during the first cycle.

This irreversible loss of capacity is consistent with an irreversible damage of the tungsten oxide electrode and would cause the failure in a complete device. In situ UV-visible spectroscopy and scanning electron microscopy are used to examine the damage at the electrode. Results will be reported later. To investigate the possible dissolution of the tungsten oxide layer, a spectrophotometric analysis of the electrolyte was carried out.

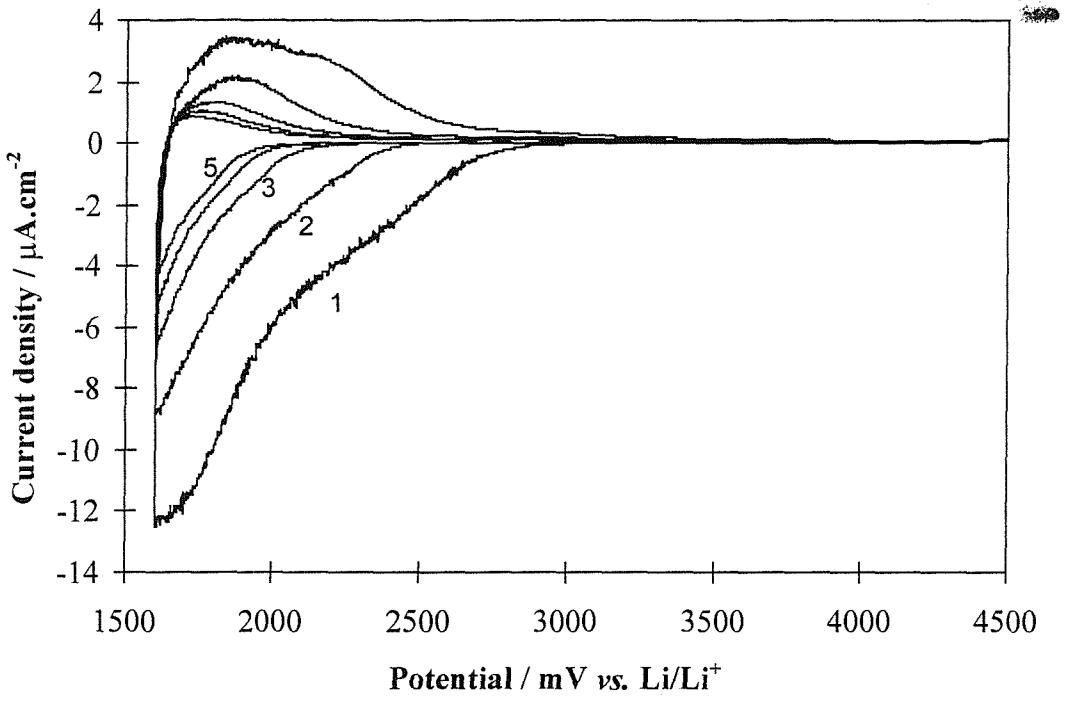

Figure 4-3: Cyclic voltammograms at 0.1 mV/s between 1.6 V and 4.5 V *vs.* Li/Li^+ for a standard amorphous WO_3 from Pilkington (same sample as on **Figure 4-1**).

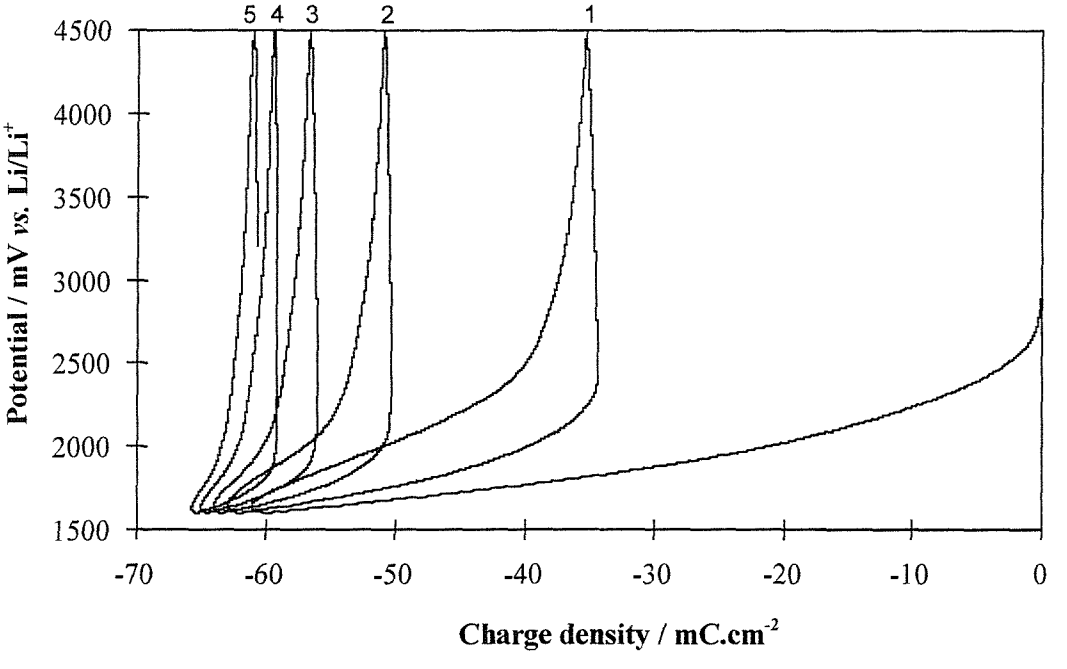

Figure 4-4: Potential *vs.* charge curves corresponding to the cyclic voltammograms on **Figure 4-3**.

4.1.1.2. In situ UV-visible spectroscopy.

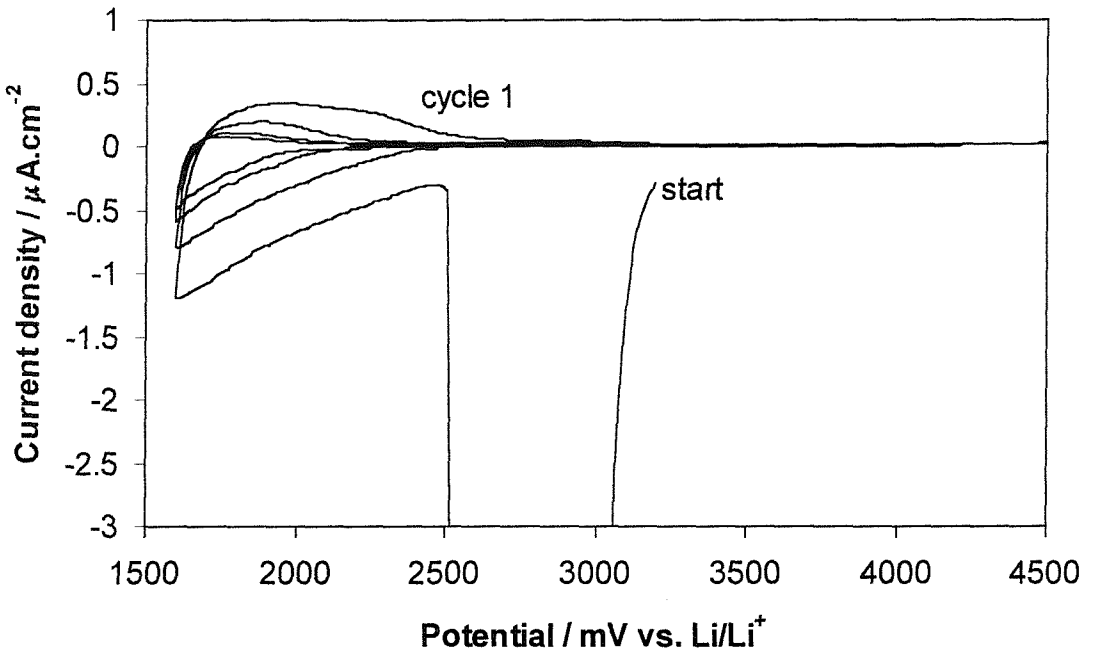

Figure 4-5: Cyclic voltammogram of a "standard" amorphous tungsten oxide from Pilkington between 1.6 V and 4.5 V *vs.* Li/Li^+

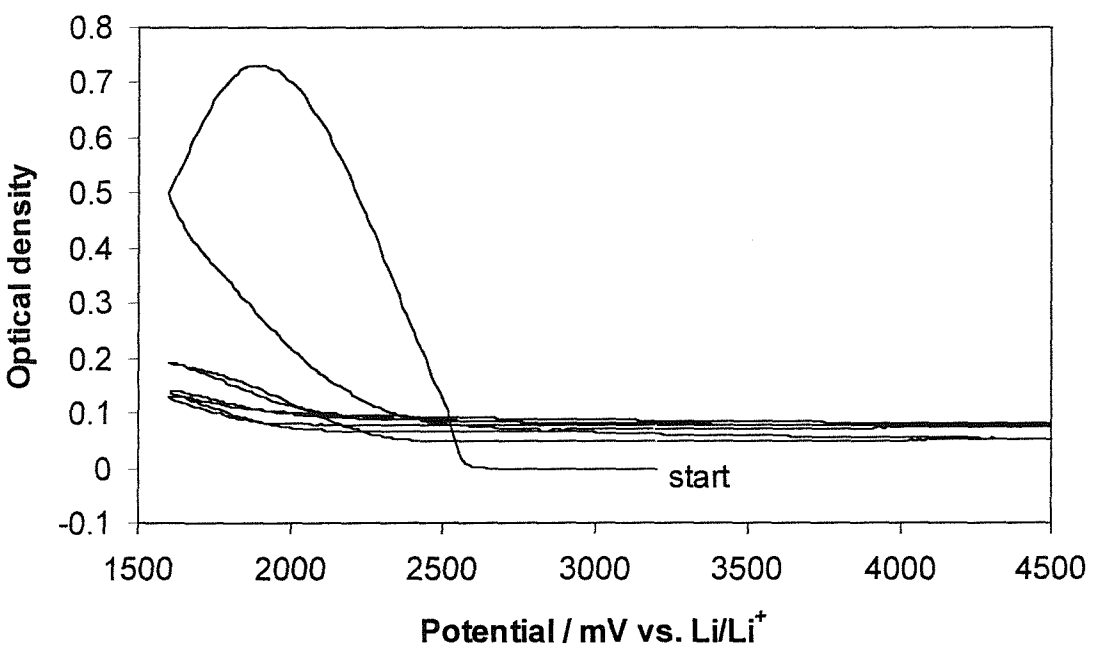

Figure 4-6: Optical density *vs.* potential curve corresponding to the cyclic voltammogram on the previous figure.

Figure 4-5 shows the cycling voltammogram of a "standard" amorphous tungsten oxide from Pilkington similar to the previous sample. In this experiment, an as-deposited sample was cycled directly between 1.6 V and 4.5 V *vs.* Li^+/Li^+. The experiment was done in a cell designed to investigate the optical changes in situ with the electrochemistry. This experiment had two aims:

- First, to determine whether the first peak is associated with a change in the optical properties of the film. This may indicate whether the reduction occurs on tungsten or elsewhere e.g. peroxyde.
- Secondly, to look at the effect of cycling the sample down to low potentials, typically below 2 V *vs.* Li/Li^+.

Figure 4-6 shows the changes in optical density *vs.* the applied potential corresponding to this experiment. The cyclic voltammogram shows a very large peak centred around 2.8 V *vs.* Li/Li^+. Figure 4-6 shows that the charge passed at 2.8 V *vs.* Li/Li^+ has no effect on the optical density of the film at 622 nm. This confirms that the peak does not correspond to a coloration process and could be due to some irreversible transformation of the as-deposited film as suggested earlier.

The second interesting observation in this experiment is the decrease of the optical density of the film below 2 V. When lithium is inserted in the tungsten oxide film, the optical density increases until the film is cycled below 2 V *vs.* Li/Li^+ when the optical density starts to decrease. The decrease in the optical density can be described as continuous with time of exposure below 2 V *vs.* Li/Li^+. Between 2 V and 1.6 V *vs.* Li/Li^+, the optical density shows a decrease of 28% of its maximum value. This result shows a damage of the electrochromic electrode confirmed by the small change in the optical density during the following cycles. At the end of the experiment, the electrode is brown showing the formation of a tungsten bronze or a damage of the underlying FTO layer. The electrolyte was analysed to determine if the tungsten oxide layer was dissolved.

4.1.1.3. Spectrophotometric titration of the electrolyte.

Xu and Parker (77) presented a method to determine the W^{VI} concentration in a liquid. Tungsten (VI) forms a yellow complex at pH = 5 with rutin in the presence of cetyltrimethylammoniumbromide. This complex is detected using UV-visible spectroscopy with an absorption maximum at 416 nm. With this technique, concentrations of tungsten (VI) as low as 10^{-7} M can de detected as shown on the calibration graphs (figure 4-7 and 4-8).

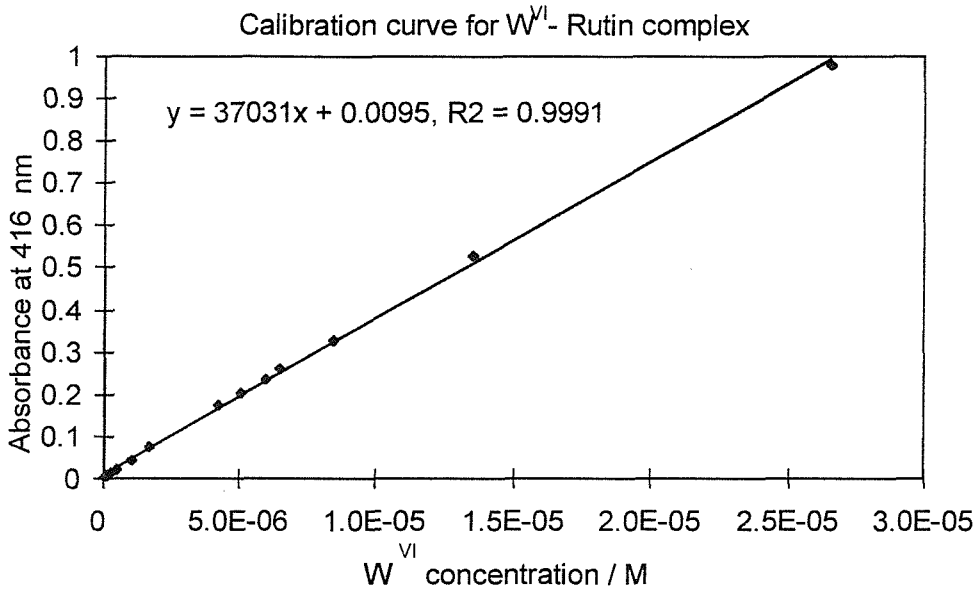

Figure 4-7: Calibration curve for the W^{VI}-Rutin complex.

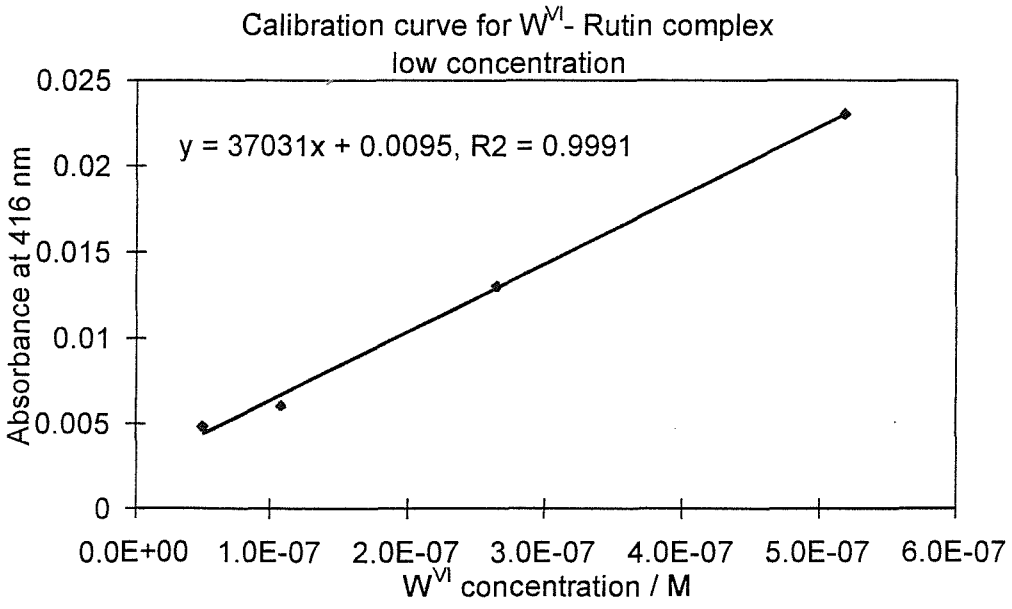

Figure 4-8: Calibration curve on figure 4-7 expanded in the low concentrations region.

It is very difficult to know the amount of tungsten oxide deposited during the sputtering. To have a correct value, the thickness of the sample and the density must be known. The other possibility is to dissolve the tungsten oxide and determine the concentration of the solution obtained. The spectrophotometric titration of tungsten (VI) technique is an accurate measure of the concentration of tungsten as shown on the calibration curves. Tungsten oxide is very soluble in alkaline media. We used 1 M sodium hydroxide solutions to dissolve the tungsten oxide from the conductive glass on a given surface and neutralised the solution before using the spectrophotometric technique to determine the concentration of tungsten. Knowing the amount of tungsten oxide on the sample and the charge passed during the cyclic voltammetry we could determine the Li/W ratio at various points of the cyclic voltammetry as shown on figure 4-9. For example, the Li/W ratio at 2 V *vs.* Li/Li^+ is 0.5. This result is consistent with the results obtained in the literature (82, 83, 84).

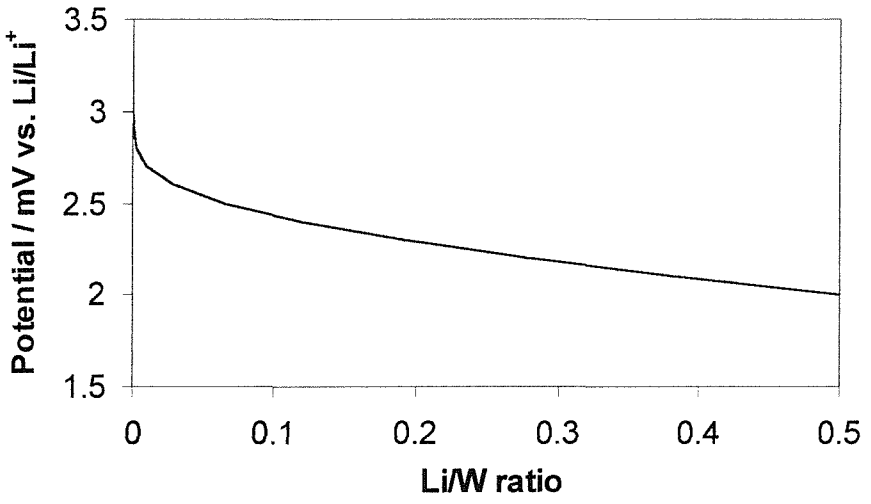

Figure 4-9: Potential *vs.* Li/W ratio curve corresponding to the second cycle of the cyclic voltammetry on figure 4-1.

No evidence of the dissolution of our samples was shown by analysing the electrolytes before and after cycling to low potentials with this technique which showed that less that 1% of the tungsten oxide layer was dissolved. Scanning electron microscopy studies of this sample should give us more details about the damage.

4.1.1.4. Scanning electron microscopy.

Figure 4-10 shows the surface of the sample before cycling. It is similar to the surface after 5 cycles down to 2 V *vs.* Li/Li^+ (figure 4-11). Another sample cycled in the normal conditions shows a few scattered anomalous structures resembling flint arrowheads as shown figure 4-12. After cycling the sample five times between 1.6 V and 4.5V *vs.* Li/Li^+, the sample is covered with dark patches of 1-10 microns in size. These patches are covered by crystals as seen on figure 4-13. This result suggests that the tungsten could be dissolved off the sample and reprecipitated at the surface.

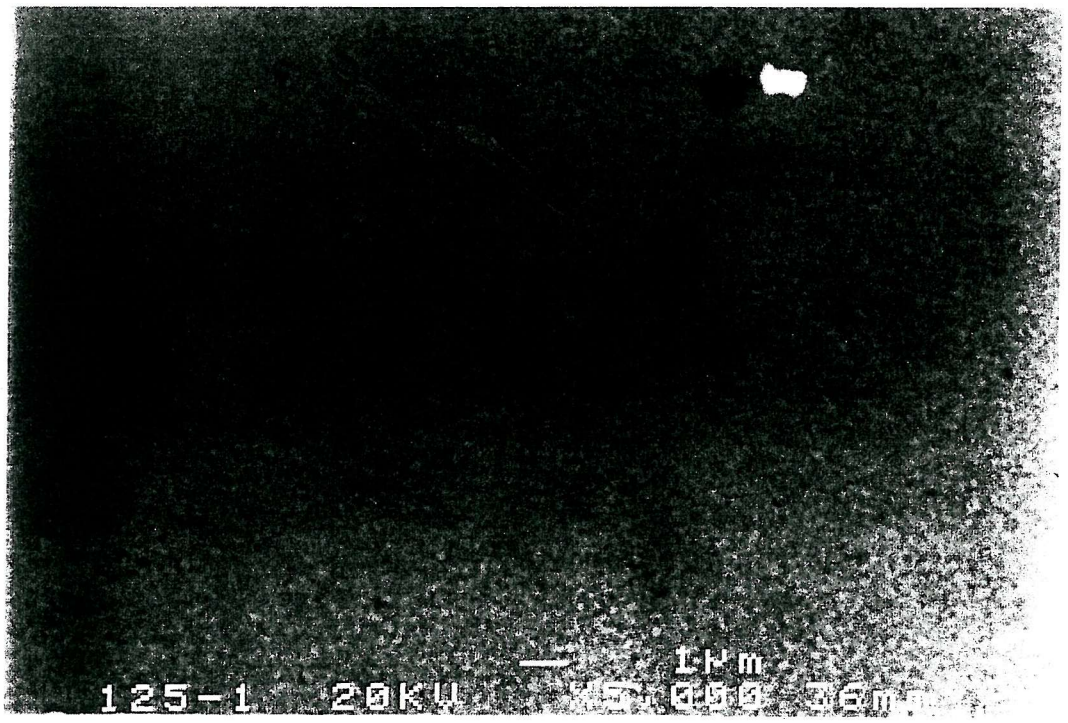

Figure 4-10: before cycling.

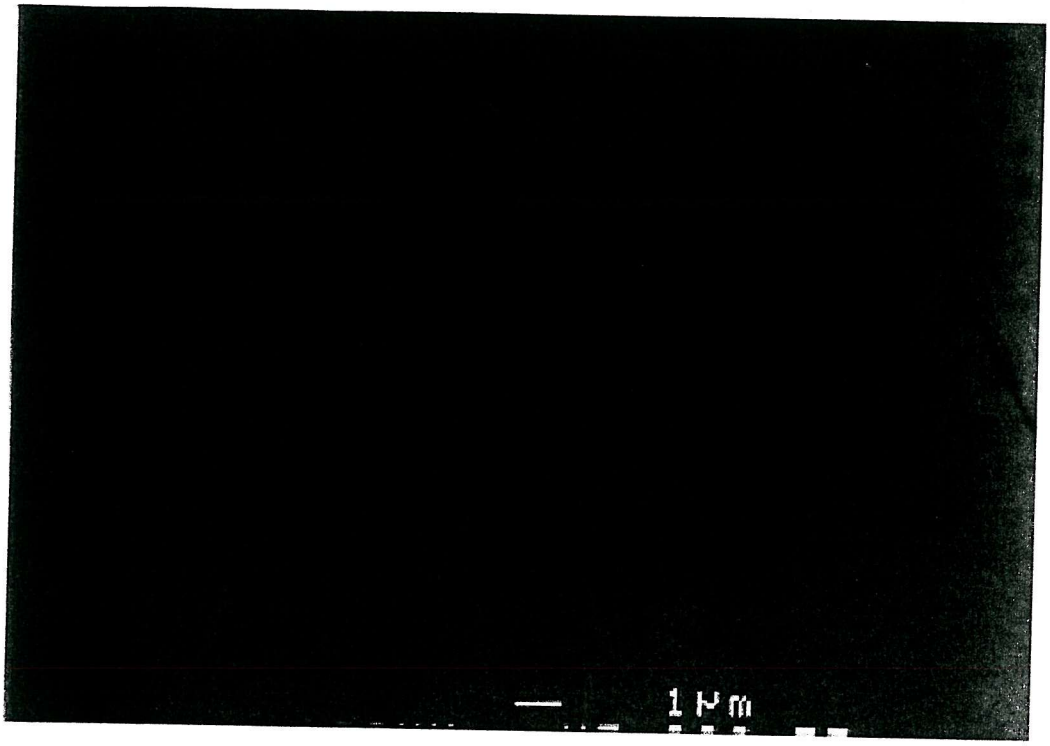

Figure 4-11: after 5 cycles down to 2 V.

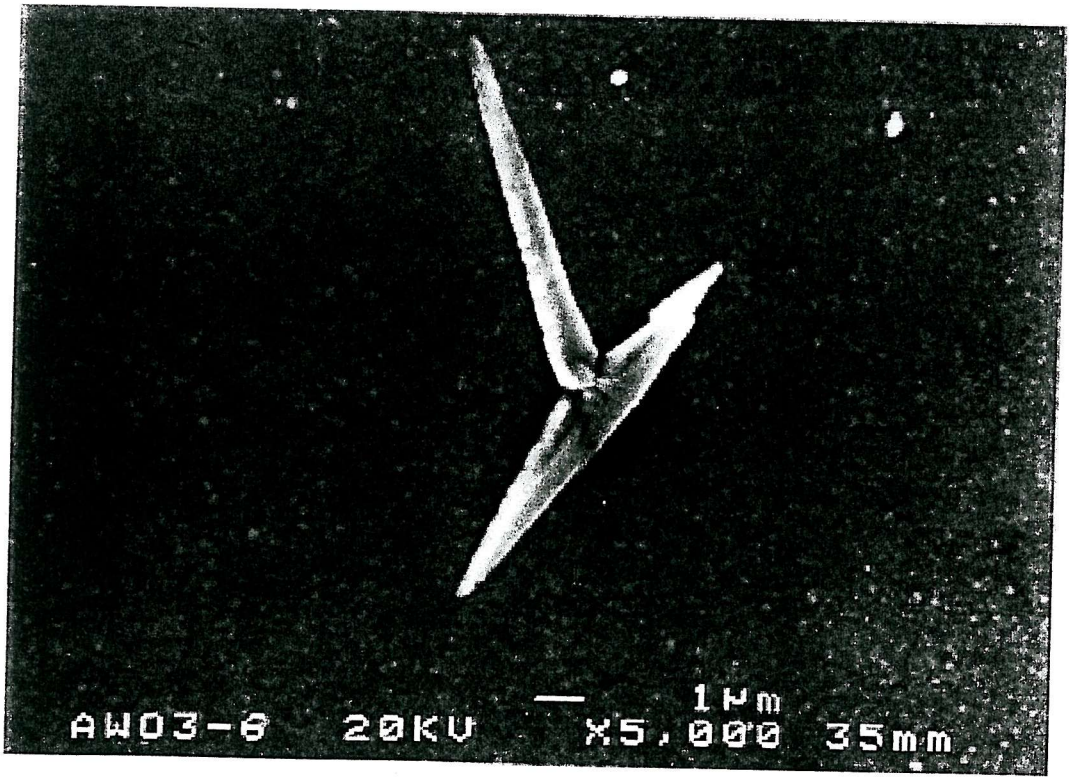

Figure 4-12: after 5 cycles down to 2 V (other sample).

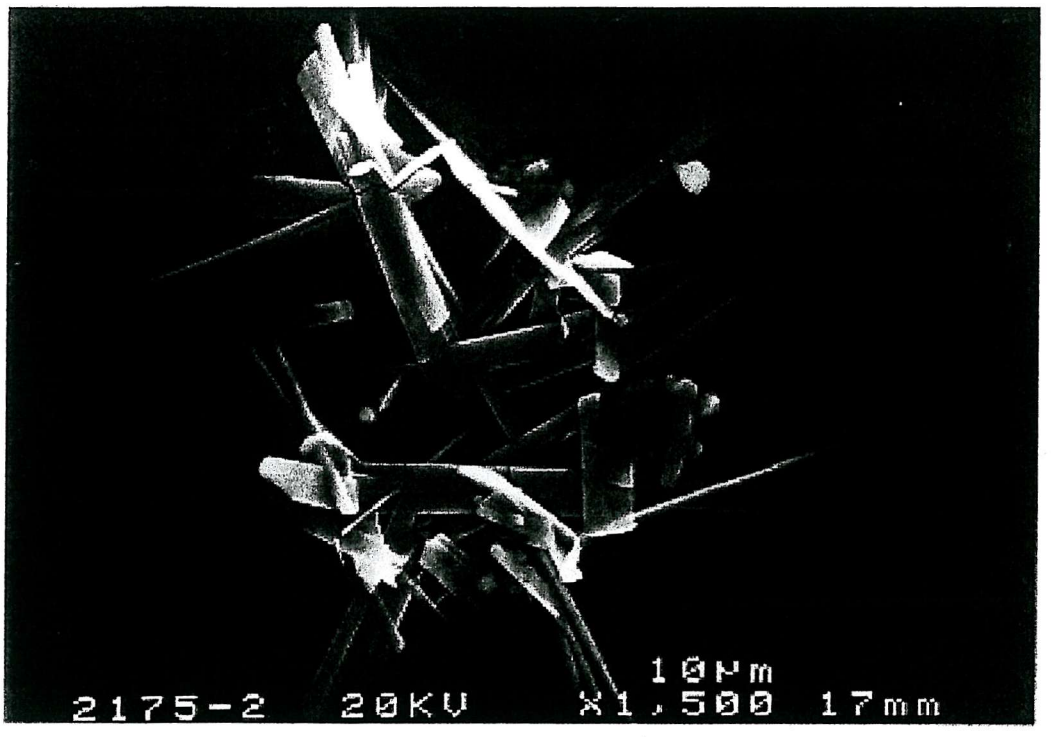

Figure 4-13: after 5 cycles down to 1.6V *vs.* Li/Li^+.

4.1.1.5. Suggested corrosion model.

The cyclic voltammetry experiment showed an irreversible damage of the electrochromic electrode when it was cycled down to 1.6 V *vs.* Li/Li^+. Although no evidence of tungsten oxide dissolution was shown with the spectrophotometric technique, the scanning electron microscopy clearly showed some areas where the tungsten oxide was dissolved and reprecipitated forming crystals at the surface of the sample. It is suspected that a localised cathodic parasitic reaction creates highly alkaline conditions near the electrode surface, causing a pit-like corrosion of the thin film. Away from the surface, conditions are less alkaline and precipitation occurs as shown on figure 4-14.

The reaction of dissolution of the oxide can be written as follows:

$$WO_3 + 2OH^- \rightarrow WO_4^{2-} + H_2O$$

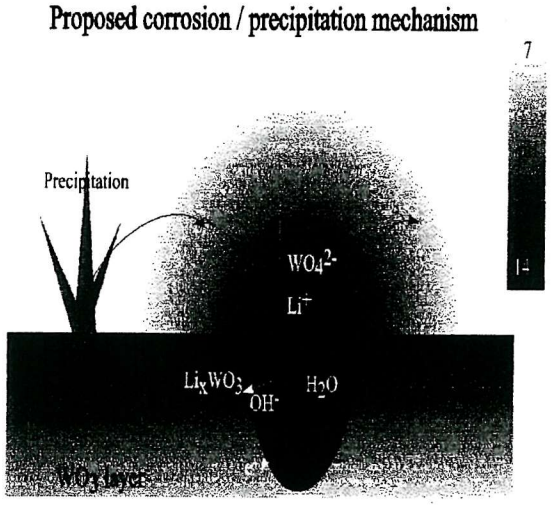

Figure 4-14: Suggested corrosion model for a "standard" amorphous tungsten oxide sample.

4.1.2. Amorphous tungsten oxide sputtered at higher power.

4.1.2.1. Cyclic voltammetry.

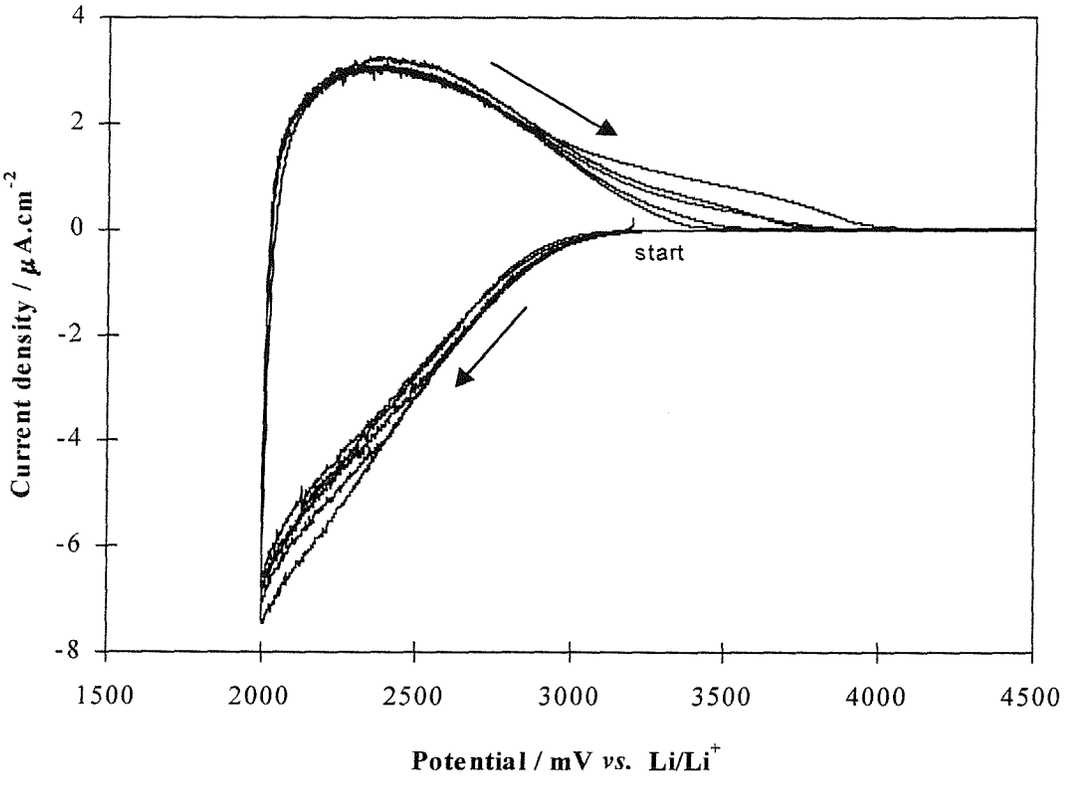

Figure 4-15: Cyclic voltammogram between 2 V and 4.5 V *vs.* Li/Li^+ of an amorphous tungsten oxide sample sputtered at higher power.

Figure 4-15 shows the cyclic voltammograms for a second type of sample supplied by Pilkington technology centre: amorphous tungsten oxide sputtered at higher power. This voltammogram is very similar to the voltammogram of the "standard" amorphous sample studied before. A few differences are noticeable. First, no cathodic peak is shown in the first cycle. This is probably due to the increase of sputtering temperature due to the higher power. The high temperature will prevent the formation of the peroxide bonds in the film. Secondly, with the "standard" amorphous sample, the current falls to zero above 3.5 V *vs.* Li/Li^+. In this case, a slower decrease of the current is observed during the first three cycles. This is probably due to a slower diffusion in the film. A similarity between the two types of samples is the good

stability of the sample upon cycling between 2 V and 4.5 V *vs.* Li/Li^+. This good stability was observed for a large number of cycles.

The stability upon cycling to lower potential (down to 1.6 V *vs.* Li/Li^+) was then investigated. Figure 4-16 shows the last cycle of the previous experiment (cycle 5 between 2 V and 4.5 V) and five cycles between 1.6 V and 4.5 V *vs.* Li/Li^+. In the sixth cycle, the voltammogram is superimposable to the voltammogram of the fifth cycle down to 2 V. The current increases again down to 1.6 V. In the extraction half cycle, the current is higher than the current observed in the fifth cycle but only two third of the charge inserted was extracted (figure 4-17). In the 7^{th} cycle, only about half the charge inserted was extracted: 56 $mC.cm^{-2}$ inserted and only 29 $mC.cm^{-2}$ extracted. In the subsequent cycles, current and charge decrease with the number of cycles showing irreversible damage of the tungsten oxide electrode. The behaviour of the tungsten oxide sputtered at high power is overall very similar to the behaviour of the "standard" amorphous tungsten oxide as far as the electrochemistry is concerned. The other similarity between the two samples is the brown colour that appears after 5 cycles down to 1.6V vs. Li/Li^+. Scanning electron microscopy was used to investigate the damage at the surface of the electrodes.

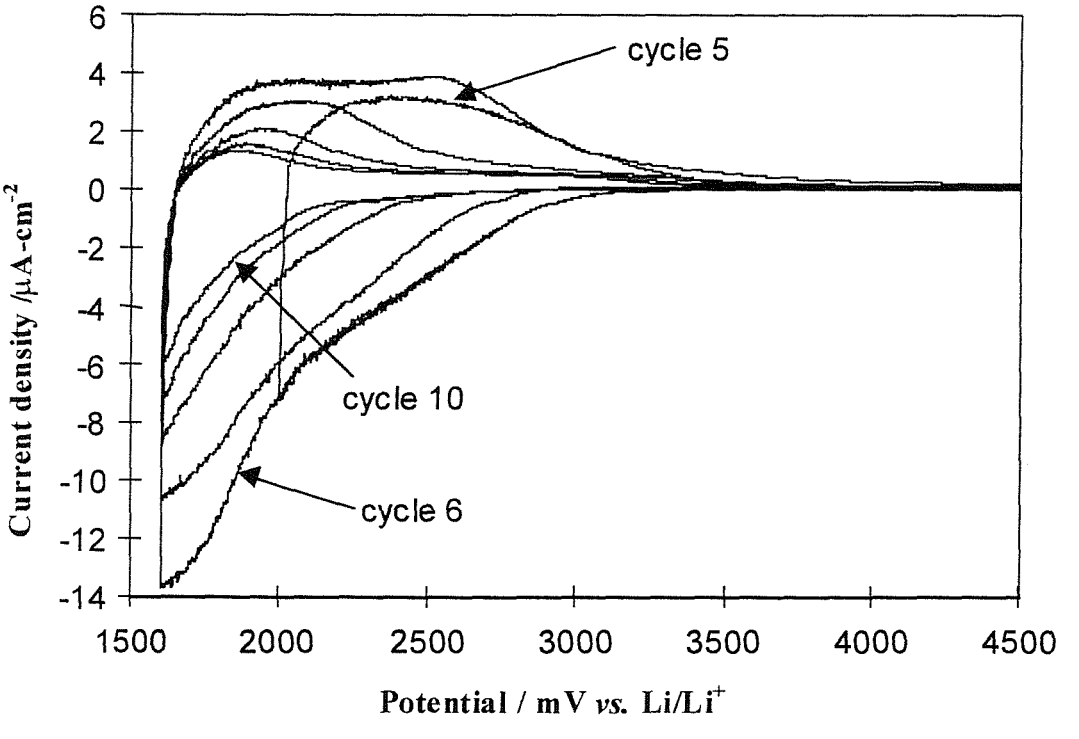

Figure 4-16: Cyclic voltammogram (same sample as figure 4-12): 1 cycle between 2 and 4.5 V and 5 cycles between 1.6 V and 4.5 V *vs.* Li/Li^+.

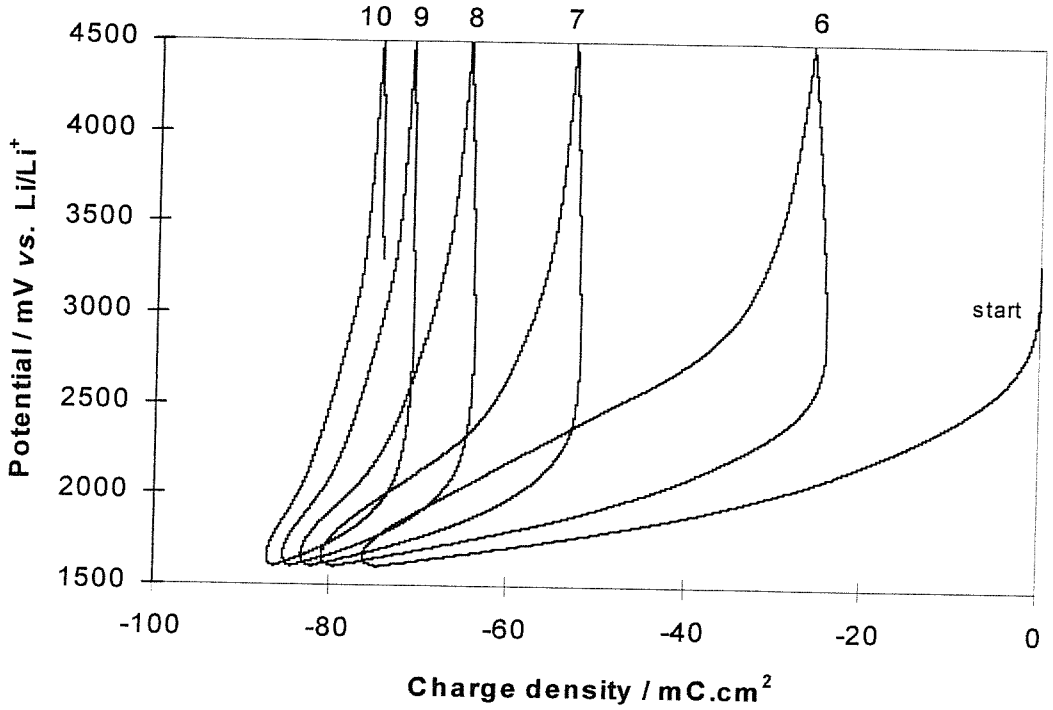

Figure 4-17: Potential *vs.* charge curves corresponding to the cyclic voltammograms on figure 4-16.

4.1.2.2. Scanning electron microscopy.

Before cycling (figure 4-18) and after cycling down to 2 V *vs.* Li/Li^+ (figure 4-19), the tungsten oxide sputtered at high power is very similar to the "standard" amorphous tungsten oxide. The surface of the sample is completely different after 5 cycle down to 1.6 V *vs.* Li/Li^+: there is no flint arrowhead crystal as seen for the previous sample but some cracks appear at the surface of the electrode. These cracks are probably due to an excessive expansion of the lattice during the insertion of the lithium (figure 4-20) and a compressive stress that induces a loss of adhesion.

A low temperature sample will be highly amorphous. Its amorphous structure will increase its solubility but it will have a more compliant structure that could absorb stress. The higher power used to sputter the second sample produced a higher temperature that increased the short-range order eliminating the OH group which would contribute to increase the solubility.

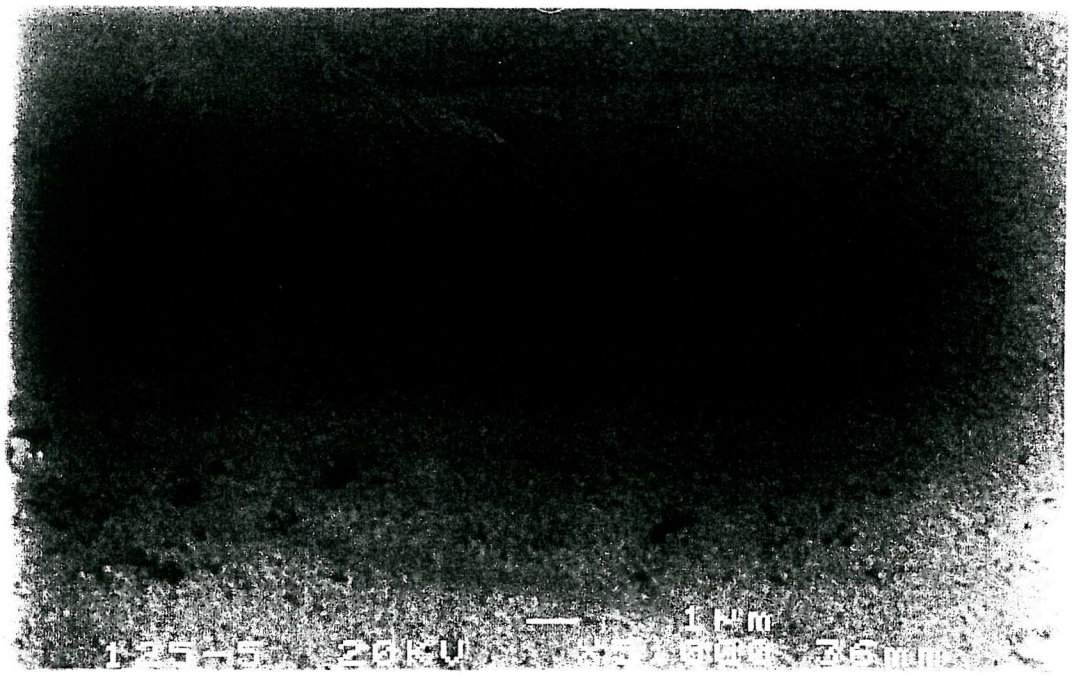

Figure 4-18: before cycling.

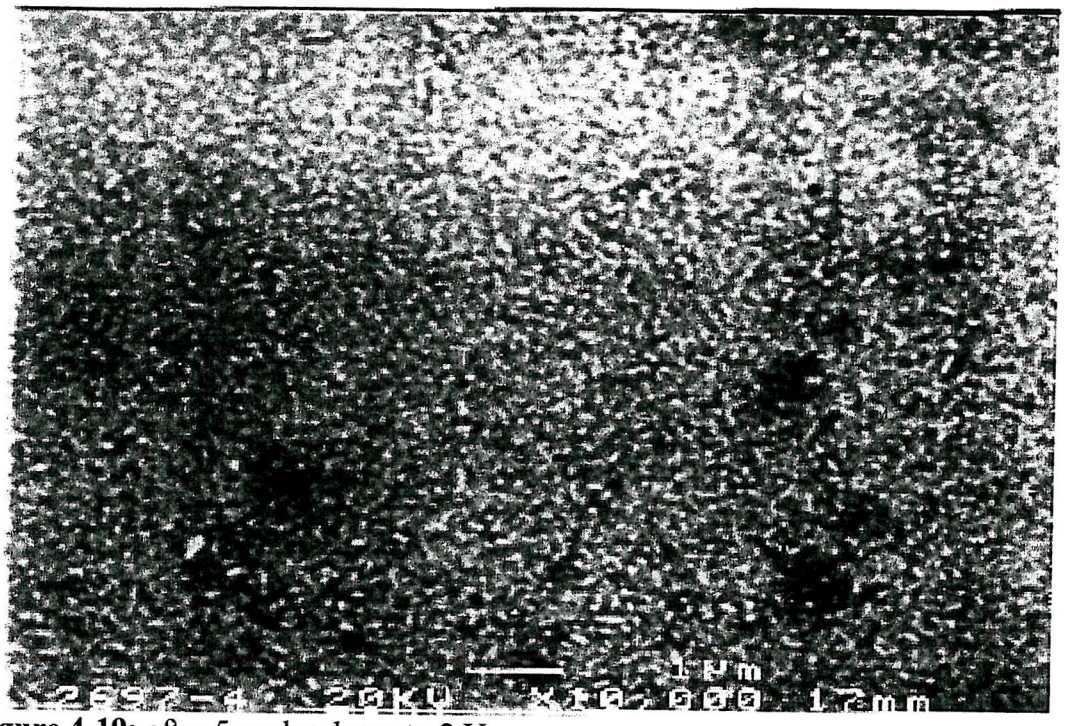

Figure 4-19: after 5 cycles down to 2 V.

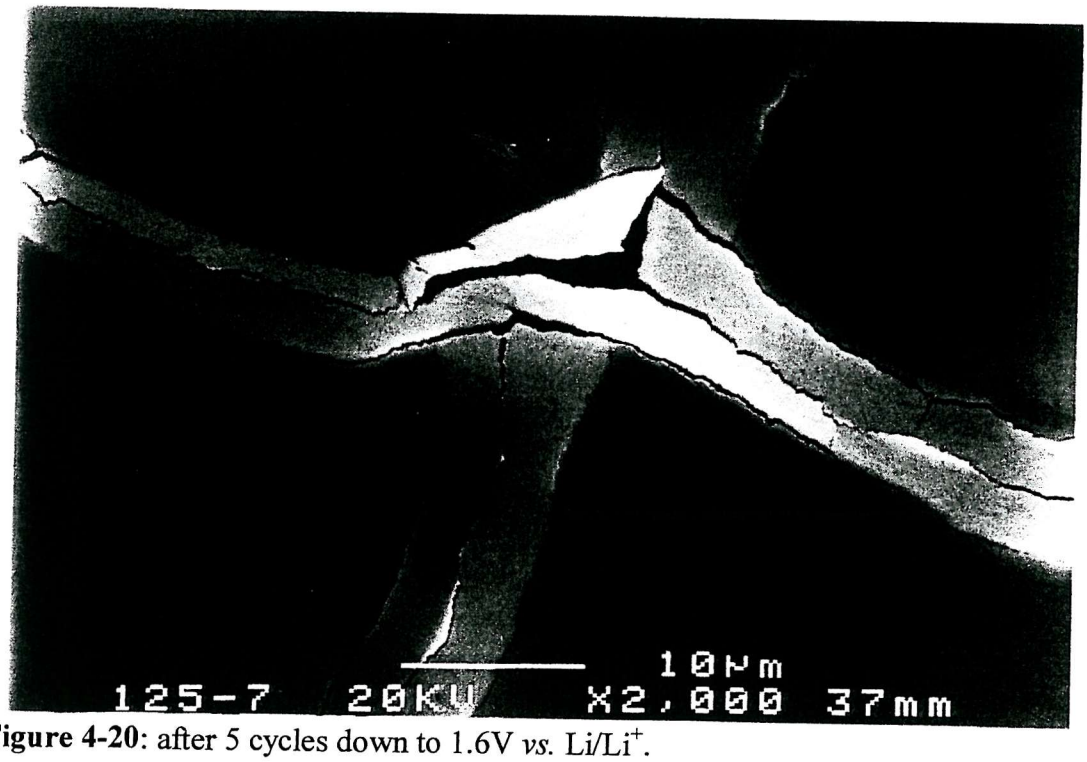

Figure 4-20: after 5 cycles down to 1.6V *vs.* Li/Li^+.

4.1.3. Amorphous WO_3 sputtered at Southampton.

4.1.3.1. Effect of the sputtering conditions.

The sputtering conditions used at Pilkington technology centre were unknown. The only information was that a tungsten oxide target and DC magnetron sputtering were used. Thus, the first objective was to find some conditions to get samples similar to the samples obtained at Pilkington. A tungsten metal target 99.9% was used and mixed argon-oxygen atmospheres with various argon to oxygen ratios were tried. DC-magnetron sputtering was used with a constant power: 1 A and 600 V.
The argon and oxygen flows were controlled by two mass flow controllers but in view of the complexity of the system, it was difficult to evaluate the effective pressure of these two gases during the sputtering. However, it was recognised that changing the relative flows was effective in varying the stoechiometry of the oxide and the deposition rate. The argon to oxygen ratio is very important because it fixes the stoichiometry of the oxide and it influences the deposition rate as shown by Akram *et al* (85) and Kaneko *et al.* (86). In the following description, the flow settings are reported simply as the front panel dial position and variations in flow and pressure are assumed to be roughly proportional to dial settings. The tungsten oxide obtained can probably be written as WO_{3-x} but no determination of the stoichiometry was carried out.

The optimum argon to oxygen ratio was determined, all the other parameters remaining constant. The argon flow was maintained constant and equal to 40. The oxygen flow was varied from 40 to 130. The samples sputtered with oxygen flow below 80 were blue, colour characteristic of a suboxide. Samples sputtered with an oxygen flow between 80 and 100 were transparent before lithium insertion but did not bleach during lithium extraction. Samples sputtered with an oxygen flow between 105 and 130 showed good reversibility during insertion-extraction and good bleaching. Then, the argon flow was changed to 80 and samples were prepared with oxygen flow from 105 to 130.

The thickness of the sample was measured using a profilometer. The thickness (i.e. deposition rate) varies with the oxygen content and with the argon content in the atmosphere. Thus, the charge inserted in the samples varies with the oxygen content (Table 4-1). The thickness of the films varied from 3000 Å to 12000 Å.

The results in table 4-1 showed that the charge inserted in the tungsten oxide increased with the amount of oxygen in the sputtering atmosphere until it reached a maximum and then decreased. This effect was observed with two different argon flows but the maximum was reached for a lower oxygen flow with an argon flow of 80.

Argon flow settings	Oxygen flow settings	Charge inserted ($mC.cm^{-2}$)	Approximate thickness (Å)
80	105	-169.6	9000
	110	-151.48	8500
	115	-201.74	10000
	120	-221.36	12000
	125	-222.77	12000
	130	-160.33	9000
40	105	-201.4	8000
	110	-170.29	6500
	115	-213.08	10000
	120	-139.11	4500
	125	-130.46	4000
	130	-119.72	3000

Table 4-1: Charge inserted during the first cycle at 2V *vs.* Li/Li^+ for each sample.

The conditions chosen for the experiments described after were:

- Ar flow: 40
- Oxygen flow: 120
- Current 1 A
- Voltage: 600V
- Sputtering time: 10 minutes

4.1.3.2. Cyclic voltammetry.

Figure 4-21 shows representative cyclic voltammetry at 0.1 mV/s for an amorphous tungsten oxide sample sputtered at Southampton between 2 V and 4.5 V *vs.* Li/Li^+. The first cycle shows a cathodic peak, which was ascribed to trapped oxygen or peroxo-bonds in the film. After this first cycle, the cyclic voltammograms are perfectly superimposed. Although the voltammograms show a good reproducibility after the first cycle, the potential *vs.* charge curve showed in figure 4-22 is slightly shifted towards the cathodic region for each cycle, showing a small parasitic reaction. A similarity with the sample sputtered at high power supplied by Pilkington is the slow decrease of the current above 3 V vs. Li/Li^+. This phenomenon can probably be explained to slow kinetics due to the thickness of the sample.

To investigate this parasitic reaction, the cell was cycled at lower potential: down to 1.6 V *vs.* Li/Li^+. The cyclic voltammograms are shown figure 4-23. The first cycle at 1.6 V *vs.* Li/Li^+ (cycle 6) is similar to the previous cycle down to 2 V. Cycling down to 1.6 V, the current carries on increasing. In the extraction half cycle, only two thirds of the charge is extracted from the film as shown in the potential *vs.* charge curve (Figure 4-24). After this first cycle down to 1.6 V *vs.* Li/Li^+, the voltammograms show an irreversible loss of current at each cycle. After 5 cycles, the charge inserted in the tungsten oxide electrode is only 20 % of the charge inserted in the first cycle as shown on figure 4-24. These results show an irreversible damage of the electrode as observed previously with the amorphous tungsten oxide sample from Pilkington Technology centre.

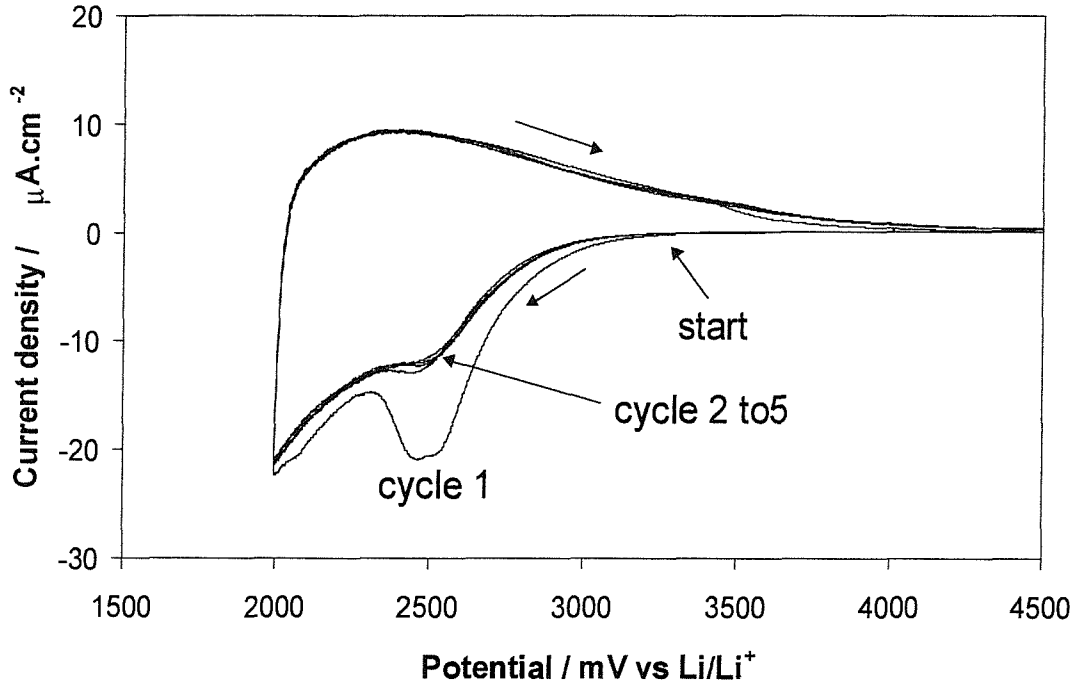

Figure 4-21: Cyclic voltammogram at 0.1 mV/s between 2 V and 4.5 V *vs.* Li/Li^+ of an amorphous tungsten oxide sample sputtered at Southampton.

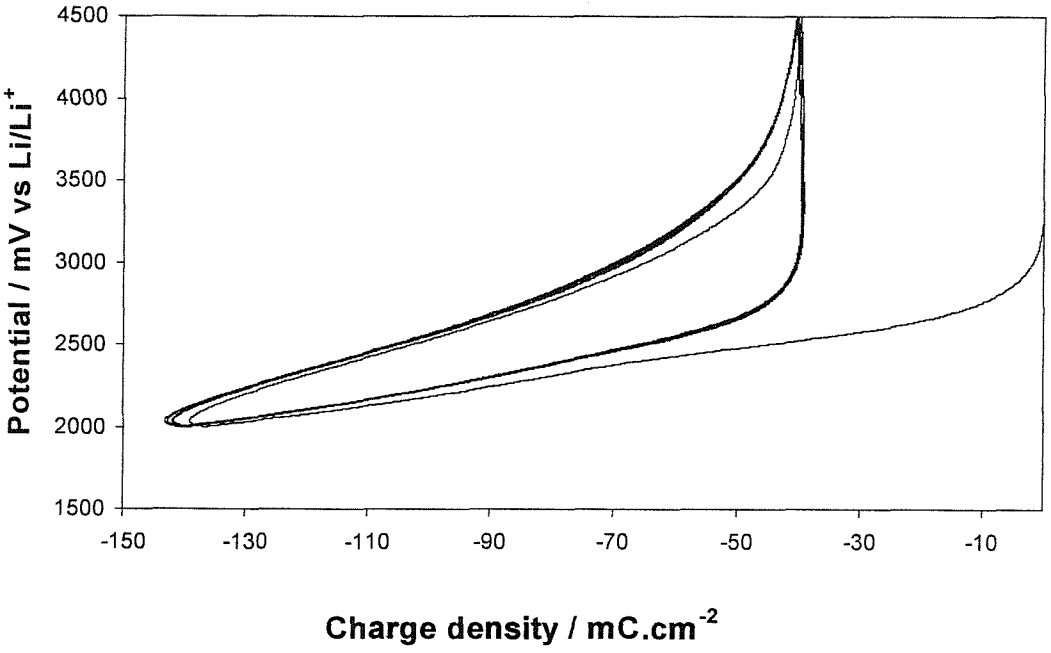

Figure 4-22: Potential *vs.* charge curves corresponding to the cyclic voltammogram shown figure 4-21.

Page 75
missing from
this Thesis

4.1.3.3. Scanning electron microscopy.

Scanning electron microscopy was used to study the damage at the surface of the electrodes as shown earlier with the other types of amorphous samples. The general surface of the as-deposited samples was very similar to the surface of the previous samples shown in figure 4-7 of the section 4.1.3.5. No evidence of a surface damage (cracks, pinholes, etc.) was shown using the scanning electron microscopy technique after cycling down to 1.6 V *vs.* Li/Li^+. The loss of current and charge might then be due to a loss of adhesion between the tungsten oxide layer and the underlying layer.

Impedance spectroscopy was then use to try to get more information on this sample and the degradation mechanism and the effect of changing the substrate was also studied.

4.1.3.4. Effect of the substrate.

4.1.3.4.1. Cyclic voltammetry of the substrate.

Three different substrates were used for the samples sputtered at Southampton: K-glass (fluorine doped tin oxide coated glass), glassy carbon and stainless steel. The cyclic voltammograms of the substrates in the propylene carbonate/ $LiCF_3SO_3$ (0.5M) electrolyte are presented here.

Figure 4-25 shows the cyclic voltammogram of K-glass in the electrolyte in the same potential range as the previous experiment. The voltammogram shows that k-glass reacts with the electrolyte but this reaction is not very important between 2 V and 4.5 V *vs.* Li/Li^+: the charge passed is only 1 to 2 $mC.cm^{-2}$ at each cycle. It becomes more significant when the electrode is cycled between 1.6 V and 4.5 V *vs.* Li/Li^+ with a charge of about 5 $mC.cm^{-2}$ inserted at each cycle. This charge is irreversibly inserted and could cause a failure of the device if the lithium was inserted in the FTO underneath the WO_3 layer.

Figure 4-26 shows the cyclic voltammogram of stainless steel in the same conditions. It shows that stainless steel is very reactive towards the electrolyte both at high and low potentials. Between 1.6 V and 4.5 V vs. Li/Li^+, the cathodic charge passed is about 20 $mC.cm^{-2}$ at each cycle probably corresponding to lithium inserted in the oxide layer at the surface of the stainless steel or to the formation of a passivating layer. At high potential, the charge passed is about 20 $mC.cm^{-2}$ as well. When WO_3 is deposited on stainless steel, the steel must be masked to avoid the reaction between the substrate and the electrolyte.

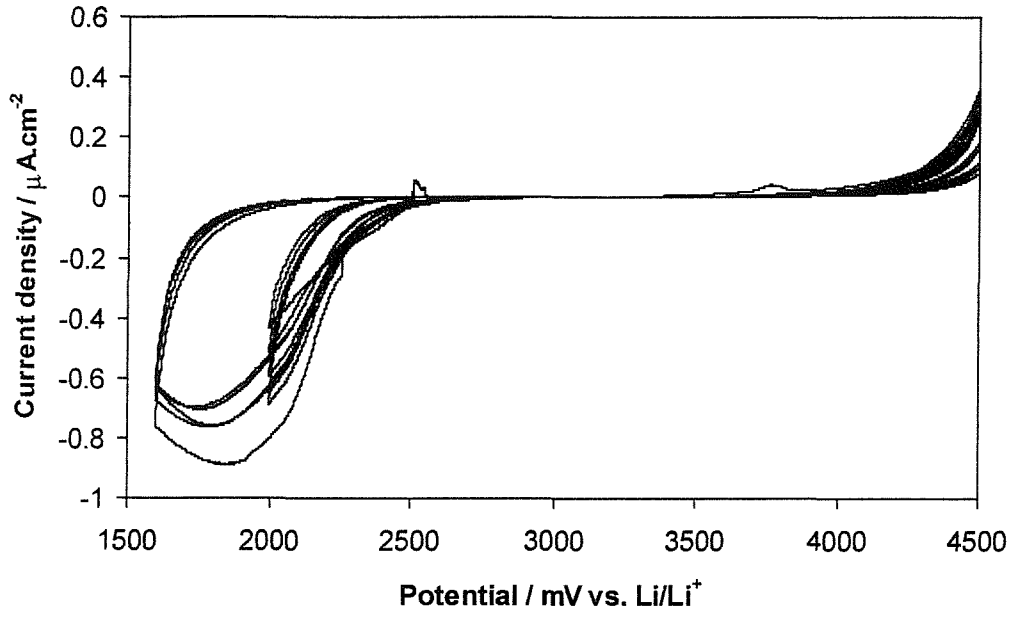

Figure 4-25: Cyclic voltammogram of K-glass at 0.1 mV/s: 5 cycles between 2 V and 4.5 V *vs.* Li/Li^+ followed by 5 cycles between 1.6 V and 4.5 V *vs.* Li/Li^+.

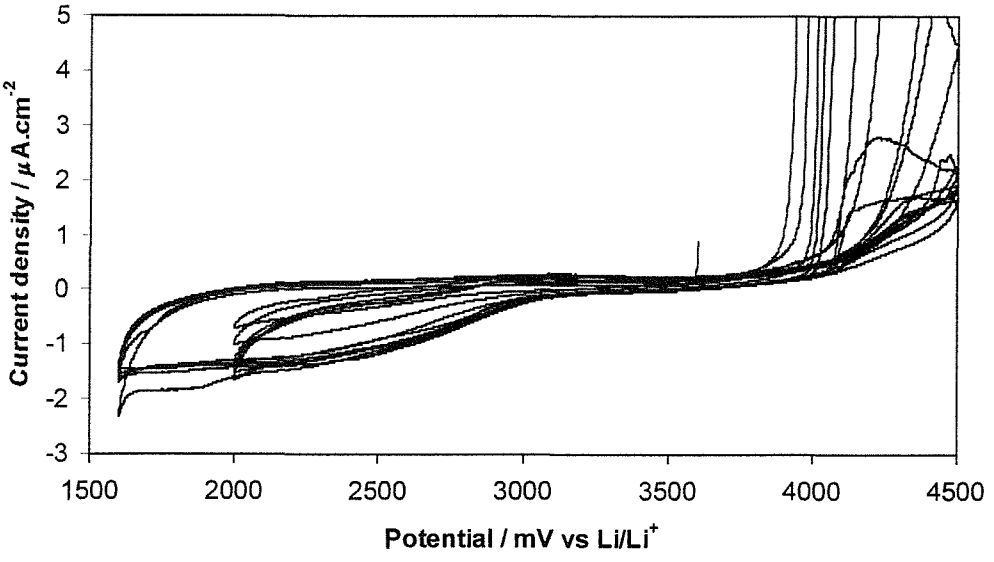

Figure 4-26: Cyclic voltammograms of stainless steel at 0.1 mV/s: 5 cycles between 2 V and 4.5 V *vs.* Li/Li^+ followed by 5 cycles between 1.6 V and 4.5 V *vs.* Li/Li^+.

Finally, figure 4-27 shows the cyclic voltammograms of glassy carbon in PC/ $LiCF_3SO_3$ (0.5M). It shows that glassy carbon is not very reactive towards the electrolyte in the potential range studied. The current is less than 0.4 $\mu A.cm^{-2}$ at 1.6 V *vs.* Li/Li^+ and the charge passed is only 1 to 2 $mC.cm^{-2}$.

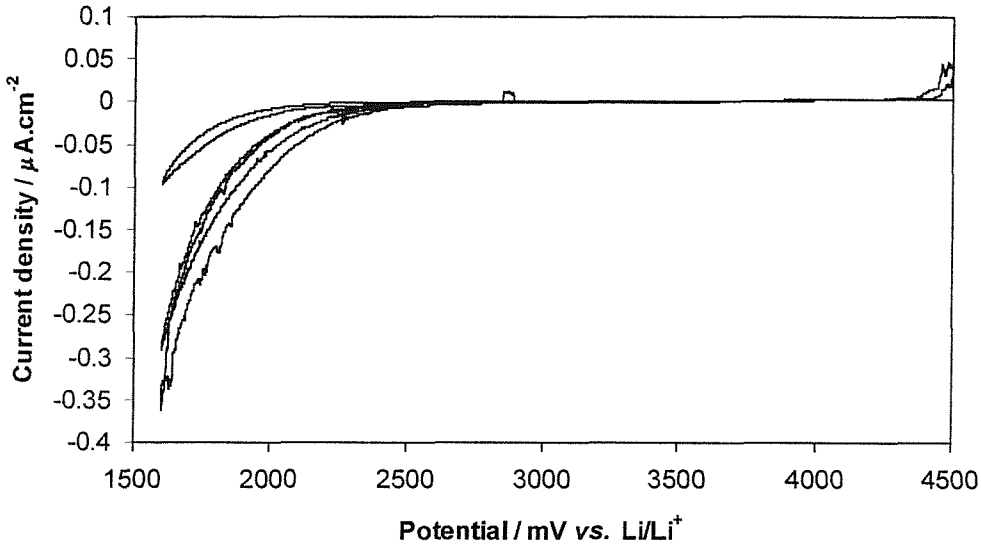

Figure 4-27: Cyclic voltammogram of glassy carbon in the electrolyte between 1.6 V and 4.5 V *vs.* Li/Li^+.

4.1.3.4.2. Cyclic voltammetry of tungsten oxide on the different substrates.

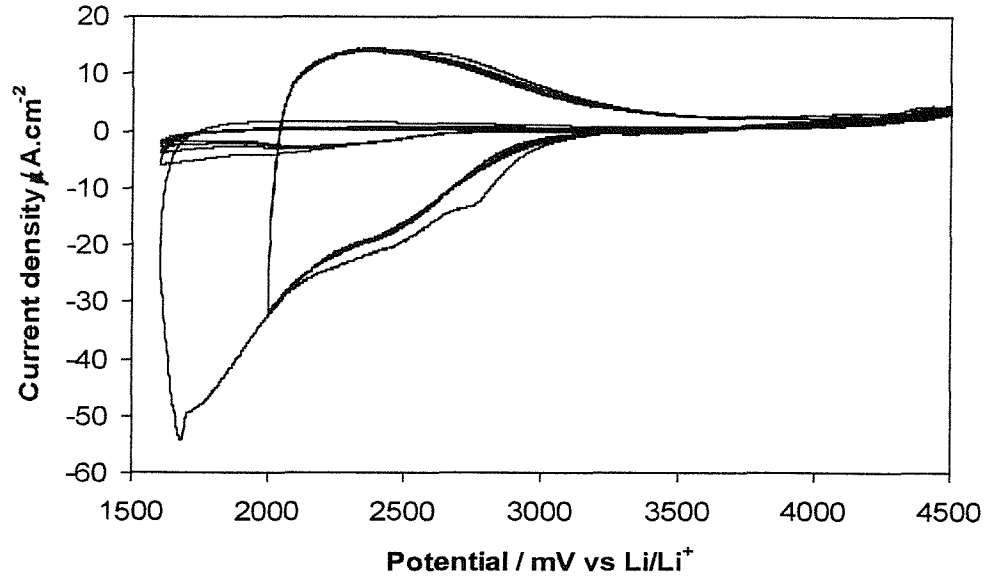

Figure 4-28: Cyclic voltammograms at 0.1 mV/s of an amorphous tungsten oxide sputtered on glassy carbon: five cycles between 2 V and 4.5 V *vs.* Li/Li^+ followed by 5 cycles between 1.6 V and 4.5 V *vs.* Li/Li^+ at 0.1 mV/s.

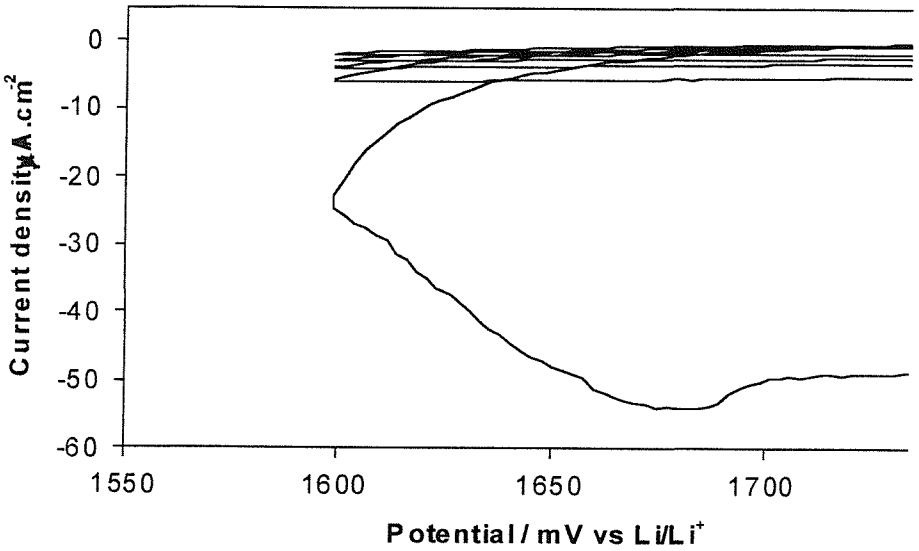

Figure 4-29: Cyclic voltammetry showed on figure 4-28, expanded in the region 1.55V to 1.75V.

The effect of changing the substrate is shown by the results displayed on figure 4-28, 4-29 and 4-30. Figure 4-28 shows the cyclic voltammetry of amorphous tungsten oxide on glassy carbon in the conditions used to study the previous samples: 5 cycles between 2 V and 4.5 V followed by 5 cycles between 1.6 V and 4.5 V *vs.* Li/Li^+. During the first cycles between 2 V and 4.5 V *vs.* Li/Li^+, the cyclic voltammogram was similar to the results obtained with the sample deposited on K-glass (fluorine doped tin oxide coated glass). Also, the downward spot to 1.6 V showed no anomalous behaviour until the event at 1.69 V, when the current increased slightly before decreasing to almost zero. The following cathodic sweeps also showed no current.

Figure 4-30 shows the cyclic voltammetry of amorphous tungsten oxide on stainless steel under the same conditions. The curves look very similar to the cyclic voltammogram obtained with on k-glass for both potential ranges, showing a gradual degradation of the amorphous tungsten oxide with repeated cycling to 1.6 V as well as a large discrepancy between the inserted and extracted charge.

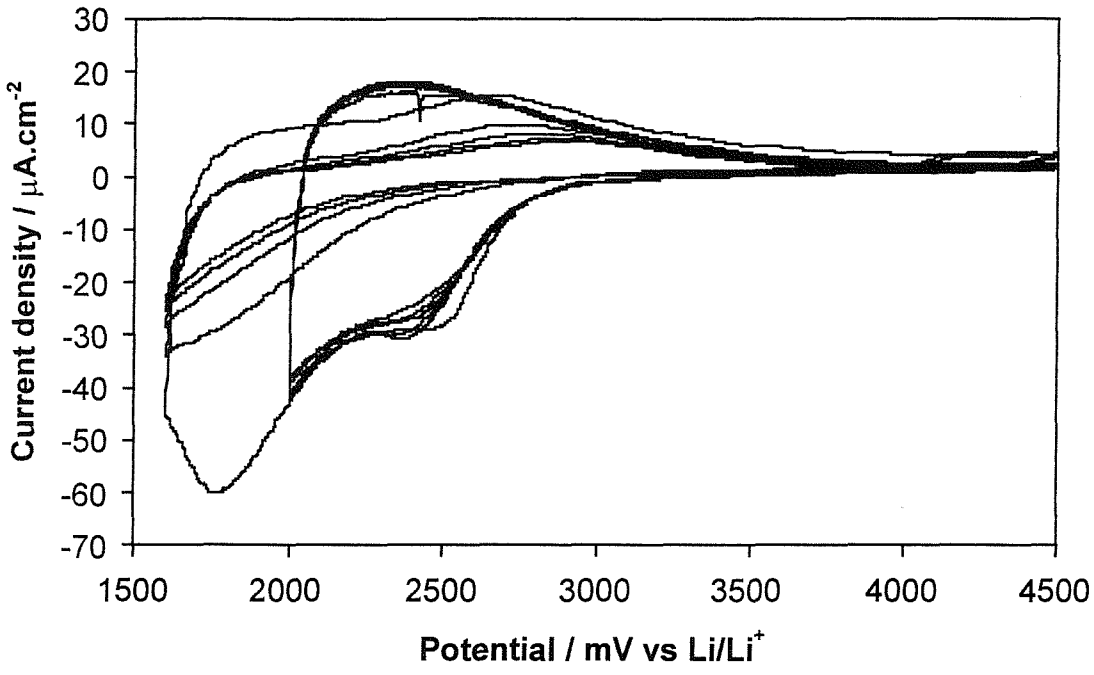

Figure 4-30: Cyclic voltammograms at 0.1 mV/s of an amorphous tungsten oxide deposited on stainless steel, in the same conditions as figure 4-28.

4.1.3.5. Impedance spectroscopy.

AC impedance spectroscopy of thin film insertion materials has been described by a few authors (87, 88, 89, 90). Figure 4-31 shows the impedance spectrum of an a-WO_3 electrode after 1 hour at 1.6 V *vs.* Li/Li^+. The charge transfer semi-circle is well separated from the diffusional part of the graph. The equivalent circuit corresponding to the system is shown on Figure 4-32. The interfacial resistance is calculated using the difference between R_2 and R_1 and the diffusional impedance using the difference between R_3 and R_2 where R_1 corresponds to the resistance at the first intersection between the semi-circle and the x axis, R_2 to the second intersection between the semi-circle and the axis and finally R_3 corresponds to the intersection between the dashed line and the x axis on figure 4-31.

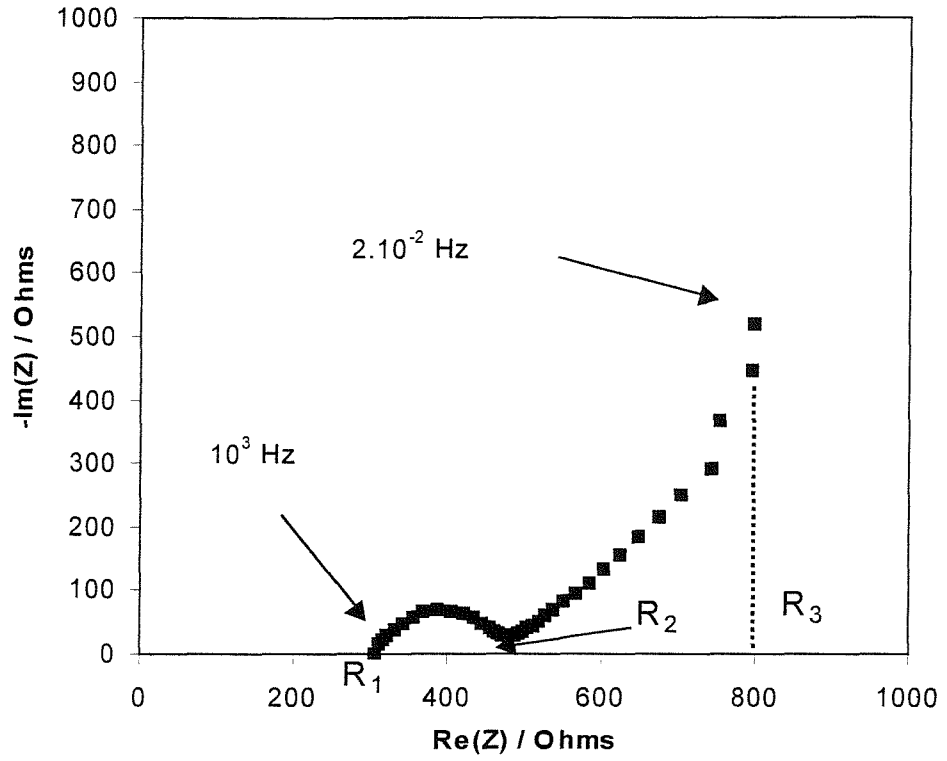

Figure 4-31: Impedance spectrum of a-WO_3 electrode left at 1.6 V *vs.* Li/Li^+ for 1 hour.

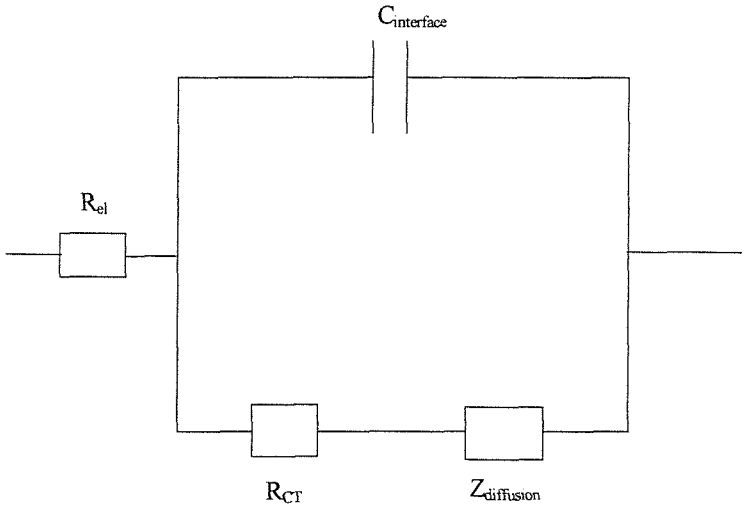

Figure 4-32: Equivalent circuit corresponding to the insertion electrode system.

The aim of this experiment was to study the effect of holding the sample at low potential: 1.6 V vs. Li/Li^+. Figure 4-33 shows the variation of the potential as a function of the time during the impedance analysis. Figure 4-34 shows the plot of the interfacial resistance and the diffusional impedance as a function of the time at 1.6 V *vs.* Li/Li^+. The sample was first held at 1.6 V for up to 72 hours and no real changes

were shown on the resistance values. The sample was then taken back to 2 V *vs.* Li/Li^+ to extract the lithium. After extracting the lithium, the sample was taken back to 1.6 V. After 24 hours back at 1.6V *vs.* Li/Li^+, the interfacial resistance increases by a factor of 3 whereas the diffusional impedance stays roughly the same,. This increase is confirmed after extracting the lithium a second time and inserting again at 1.6 V *vs.* Li/Li^+ for 24 hours: the interfacial resistance is now five times higher than the resistance at the begining of the experiment showing a loss of adhesion. These results show that the cell is damaged by successively inserting and extracting lithium when the insertion takes place at a low potential. A possible explanation for this phenomenon is that the film expands when lithium is inserted at very low potential. The loss of adhesion only occurs when the lithium is extracted and the film contracts again.

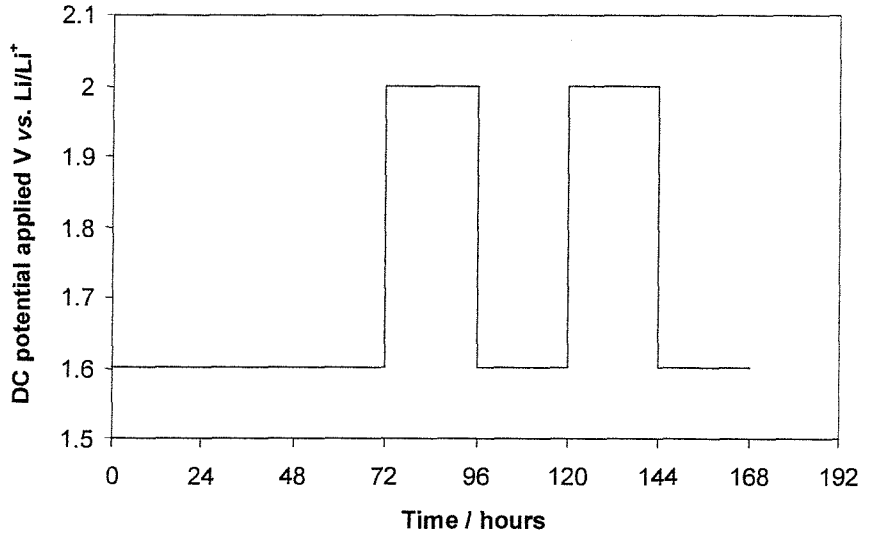

Figure 4-33: Variation of the DC potential as a function of time during the impedance analysis.

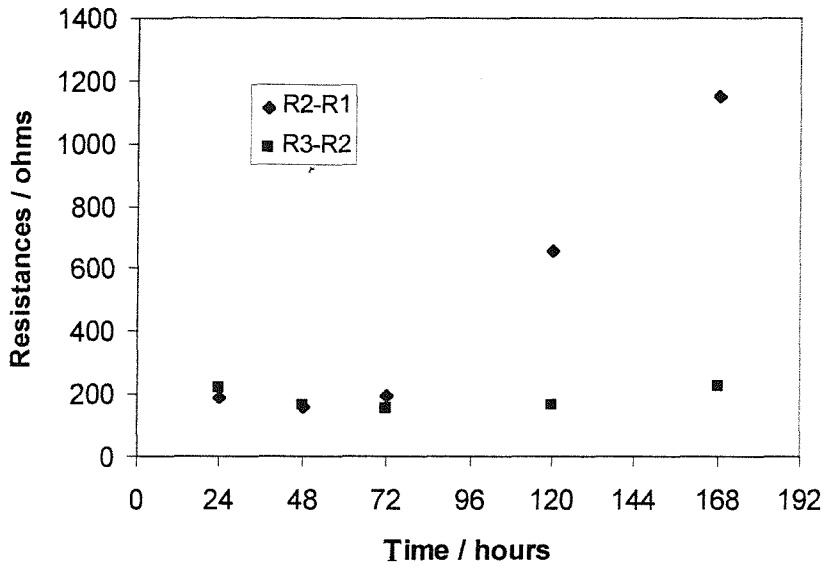

Figure 4-34: Interfacial resistance and diffusional impedance as a function of the time at 1.6 V *vs.* Li/Li^+.

4.1.3.6. Proposed model for the degradation.

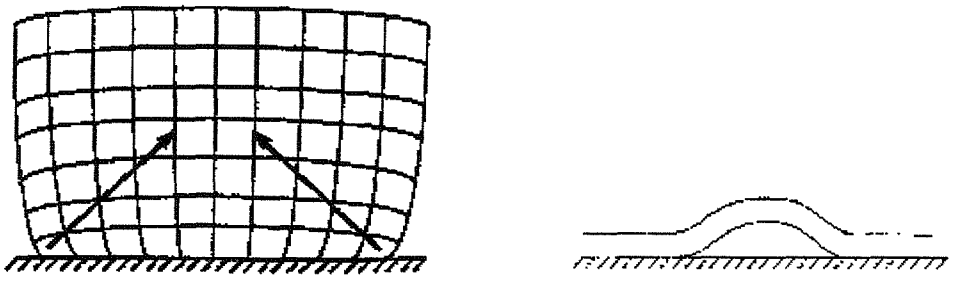

Figure 4-35: Applied strain at the interface between the electrochemical WO_3 and the underlying substrate when insertion is completed (a) and the resulting damage (b), from (91).

Our model is based on the fact that the tungsten oxide lattice expands on insertion of lithium, and that the amount of expansion increases severely at potentials below 2V *vs.* Li/Li^+. Figure 4-35 shows a textbook model of how film expansion relative to the substrate causes film detachment when the strain forces exceed the adhesion forces. The strain, compressive towards the substrate, leads to the formation of voids at the interface substrate/coating (Figure 4-35 b). In the case of Glassy Carbon, the interface

is abrupt and the substrate will behave quite rigidly, leading to a sudden delamination of the electrochromic material from the substrate at the film expansion potential. In the case of oxide (F-SnO_2) or oxide covered (passive film on stainless steel) materials, the interface is more progressive. Here we have an interphase and the strain is then better spread over, especially if the lithium can be inserted in this layer. However, this may not be sufficient to completely eliminate the creation of some voids as shown in Figure 4-35-b.

4.2. *Crystalline tungsten oxide.*

Crystalline tungsten oxide has a better reflectivity than amorphous tungsten oxide in the near IR region. That makes it a very interesting electrochromic material for "smart" windows. The electrochemical properties of c-WO_3 are also quite different from those of a-WO_3.

Two different types of crystalline tungsten oxide samples were studied. All the samples were sputtered from a tungsten target in a mixed argon-oxygen atmosphere, but the sputtering conditions were different:

- The samples prepared at Oxford were RF-sputtered and the crystalline state of tungsten oxide was obtained by heating the substrate during the sputtering.
- The samples prepared at Southampton were DC-sputtered and the crystalline state of the tungsten oxide layer was obtained by annealing the as-deposited samples at 400°C after the sputtering.

For both types of sample, various oxygen/argon ratios were used.

Crystalline tungsten oxide samples have been cycled successively five times at 0.1mV/s between 2 V and 4.5 V *vs.* Li/Li^+ and five times between 1.6 V and 4.5 V *vs.* Li/Li^+ to compare with the results obtained with amorphous tungsten oxide.

4.2.1. Cyclic voltammetry.

4.2.1.1. Samples prepared at Oxford.

Figure 4-36 shows the cyclic voltammograms obtained with the sample 1 (sputtered at 400°C with 8% O_2). The voltammograms show two insertion/extraction peaks: cathodic peaks at 2.4 V and 2.6 V *vs.* Li/Li^+ and anodic peaks at 2.7 and 2.9 V *vs.* Li/Li^+. Zhong and al. (92) attributed these peaks to phase transition: monoclinic to tetragonal for the peak at 2.6V *vs.* Li/Li^+ and tetragonal to cubic for the peak at 2.4V *vs.* Li/Li^+. The voltammograms are not perfectly similar. Judenstein and Livage (93) reported that during the first hundred cycles the shape of the curve shows

transformations. They attribute these transformations to structural modifications. When the cell is cycled down to 1.6 V *vs.* Li/Li^+, the peaks are sharper and shifted to higher potentials (2.5 V and 2.7 V *vs.* Li/Li^+). The voltammograms do show a loss of capacity during cycling but not as much as a-WO_3. The charge inserted below 2 V is extracted at higher potential: no anodic current passing through the cell below 2 V *vs.* Li/Li^+. It would seem that ion extraction is delayed by slow kinetics. Another difference with the amorphous tungsten oxide is the current passing through the cell at high potentials (above 3.5V *vs.* Li^+/Li^+). The potential/charge curve for this sample is similar to the potential/charge curve of a-WO_3: the curve is shifted towards the cathodic region indicating a significant parasitic current. Similar results were obtained with the sample 2 (sputtered at 400°C and 30% O_2) and the sample 4 (sputtered at 430°C and 30% O_2).

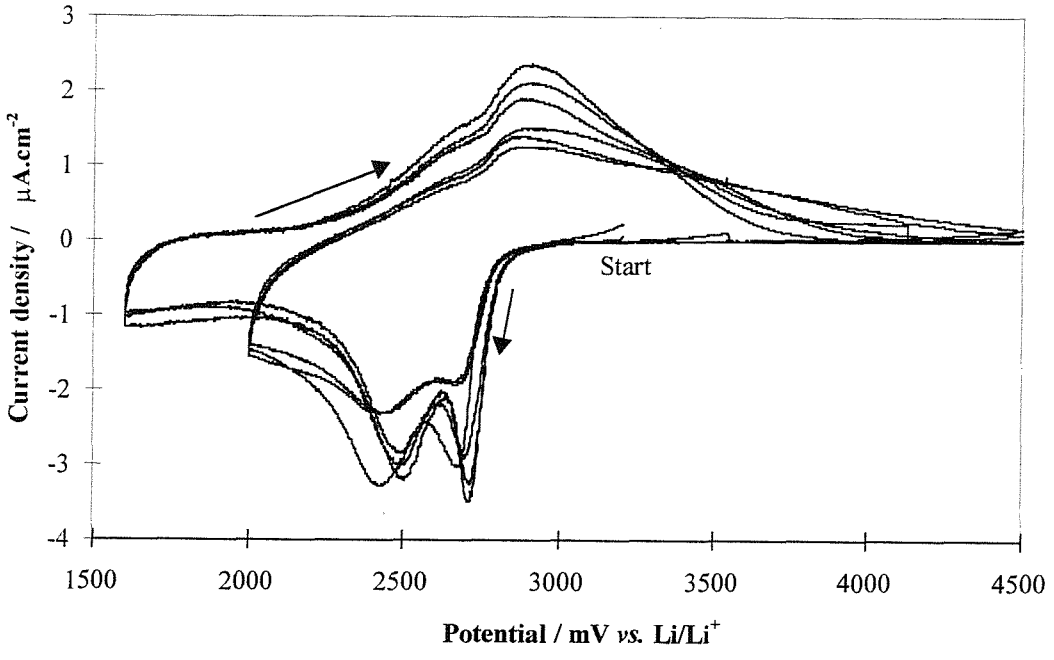

Figure 4-36: Cyclic voltammograms of a crystalline WO_3 sample sputtered at 400°C during sputtering and 8% O_2: 5 cycles between 2 V and 4.5 V *vs.* Li/Li^+.

Figure 4-37 shows the voltammograms obtained with the sample 3 (sputtered at 400°C and 40% O_2). The cathodic peaks tend to collapse into one peak. The potential/charge curve is also shifted towards the cathodic region. Cycling down to

1.6V *vs.* Li/Li^+ does not change the shape of the curve. The charge inserted below 2V is extracted at the same potential. In the high potential region (above 3.5 V *vs.* Li/Li^+), the current falls to zero. These results may be consistent with faster kinetics.
The most important property of these crystalline tungsten oxide samples is their good stability at potentials below 2 V *vs.* Li/Li^+ although slow scan rate cyclic voltammetry shows parasitic current.

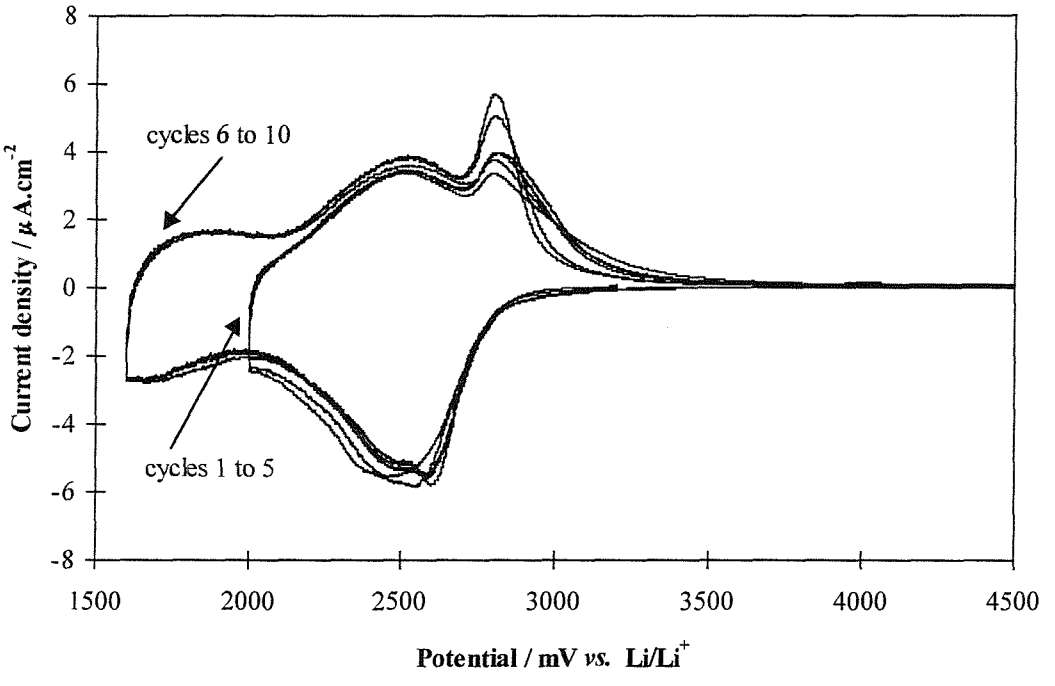

Figure 4-37: Cyclic voltammograms of a crystalline WO_3 sample sputtered at 400°C with 40% O_2 in the sputtering atmosphere: 5 cycles between 2 V and 4.5 V and 5 cycles between 1.6 V and 4.5 V *vs.* Li/Li^+.

4.2.1.2. Samples prepared at Southampton.

The home made crystalline tungsten oxide samples were amorphous samples annealed at 400°C after the sputtering under an oxygen flow in a tube furnace. The amorphous tungsten oxide samples were DC- magnetron sputtered for 10 minutes (1 A, 600 V) from a tungsten metal target in a mixed argon-oxygen atmosphere (argon flow 40, oxygen flow 115).

Figure 4-38 shows the cyclic voltammograms obtains for a crystalline tungsten oxide sample sputtered at Southampton and annealed at 400°C in oxygen after the sputtering. In the insertion half cycles, the voltammograms shows the cathodic peaks at 2.7 V and 2.4 V *vs.* Li/Li^+. In the extraction half cycles, the voltammogram shows a peak at 2.8 V and a shoulder at 2.6 V *vs.* Li/Li^+. The shape of the curves is very similar to the shape of the voltammograms obtained with the samples crystallised during the sputtering supplied by Oxford Brookes University (sample 1, sputtered at 400^0C and 8% O_2). On the electrochemical point of view, the samples crystallised by annealing the samples are 400°C after deposition are remarkably similar to the crystalline samples obtained by heating the substrate during the sputtering.

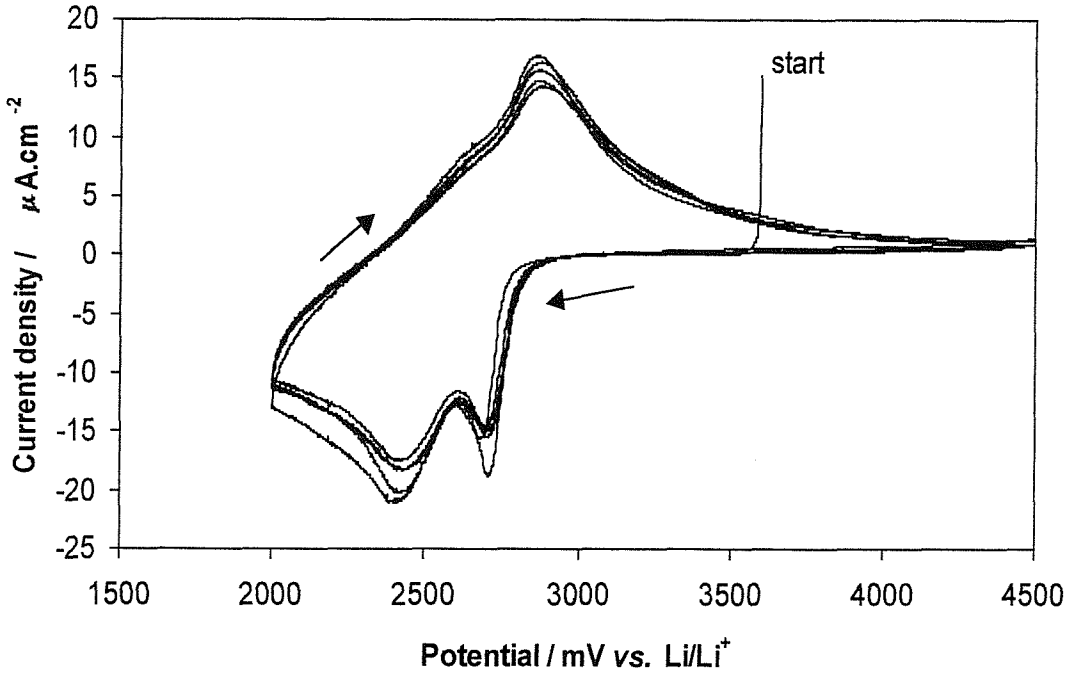

Figure 4-38: Cyclic voltammogram of a crystalline tungsten oxide sample between 2 V and 4.5 V *vs.* Li/Li^+.

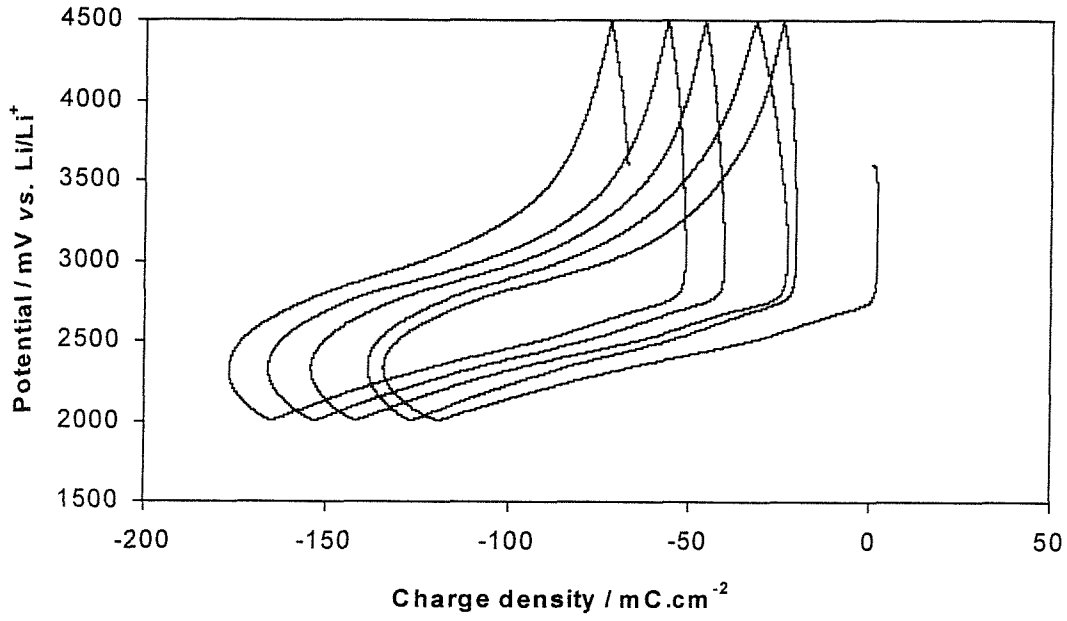

Figure 4-39: Potential *vs.* charge curves corresponding to the cyclic voltammetry on figure 4-38.

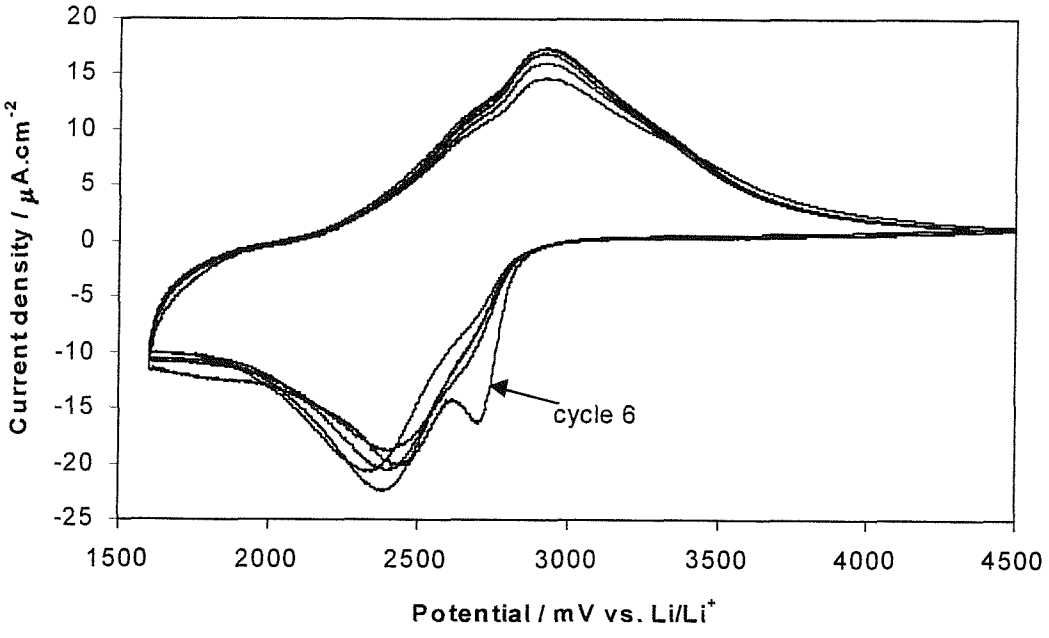

Figure 4-40: Cyclic voltammograms at 0.1 mV/s between 1.6 V and 4.5 V *vs.* Li/Li^+ for the same sample as figure 3-38.

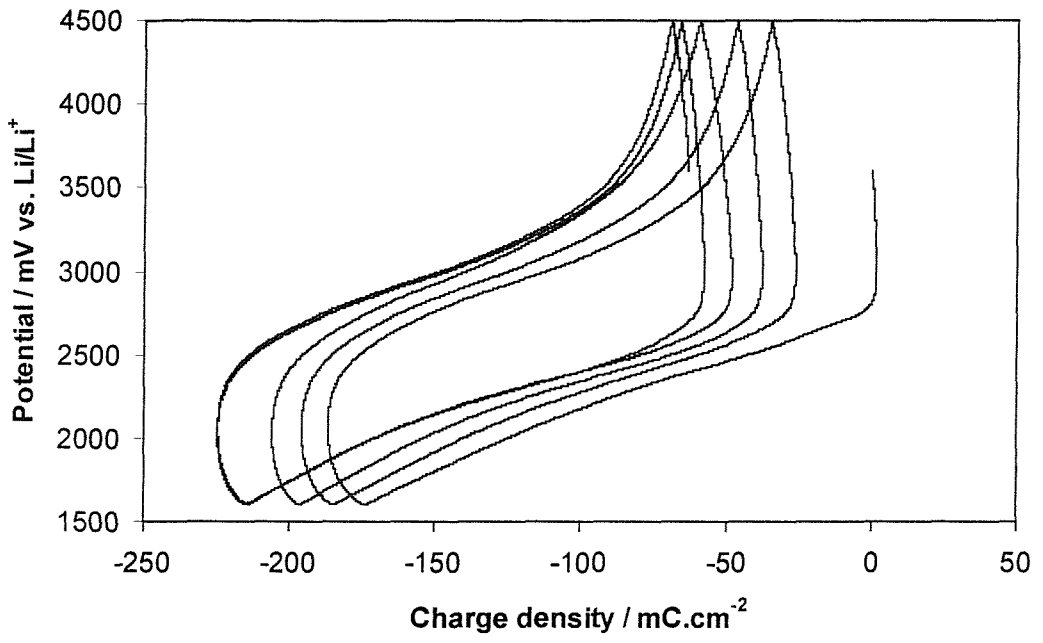

Figure 4-41: Potential *vs.* charge curves corresponding to the cyclic voltammetry on figure 4-40.

Figure 4-40 shows the cyclic voltammogram obtained between 1.6 V and 4.5 V *vs.* Li/Li^+ for the sample sputtered at Southampton and annealed after the sputtering. The voltammogram shows a few modifications during the first, second and third cycles. The first cathodic peak (at 2.6 V) disappears, maybe showing that when the sample is cycled down to 1.6 V, the monoclinic form of the tungsten oxide can not be formed any more. After, the fourth and fifth cycles are almost superimposed and their potential vs. charge curve is almost superimposed as well.

4.2.2. In situ optical density measurements.

The in situ optical density measurements were done on the samples sputtered at Oxford Brookes University. The optical density was measured at 622 nm and the cyclic voltammetry was performed at 0.1 mV/s. The aim of this study was to look at the effect of cycling the sample down to 1.6 V vs. Li/Li^+ on its optical properties.

Provided that the extinction coefficient, or electrochromic efficiency, can be regarded as constant, application of the Beer-Lambert law results in an expression for the optical density which is a function of the average composition of the sample i.e. of the Li/W ratio. As the Li/W ratio is directly proportional to the charge, the optical density is also proportional to the charge providing that all the charge passed is used for the electrochromic reaction as shown on figure 4-43. Figure 4-43 shows that Beer-Lambert is obeyed on the entire voltage range and for up to 35 mC. cm^{-2} charge inserted. In contrast with the amorphous tungsten oxide sample, crystalline sample is getting darker all the way down to 1.6 V. The proportionality between the optical density and the charge also implies that the shape of the cyclic voltammetry should be similar to the shape of the -dOD/dt *vs.* potential curve as shown on figure 4-44. This figure shows a remarkably good similarity of the curves between the cyclic voltammogram and the dOD/dt *vs.* potential curve. This similarity was not observed for the amorphous tungsten oxide sample. The only difference observed on this diagram is the absence of the peak at 2.4 V on the curve -dOD/dt *vs.* potential. Two possible explanations may be put forward:

- The phenomenon responsible for this peak on the CV is not active at the wavelength studied (i.e. 633 nm) as far as the optic is concerned.
- The electrochromic reaction is slightly delayed compared to the electrochemistry. This could explain the small shoulder observed at 2.3 V *vs.* Li/Li^+ on the –dOD/dt *vs.* potential curve.

The UV-visible spectroscopy in situ with the cyclic voltammetry for this sample shows a good optical stability as well as electrochemical stability of the sample at potential as low as 1.6 V *vs.* Li/Li^+.

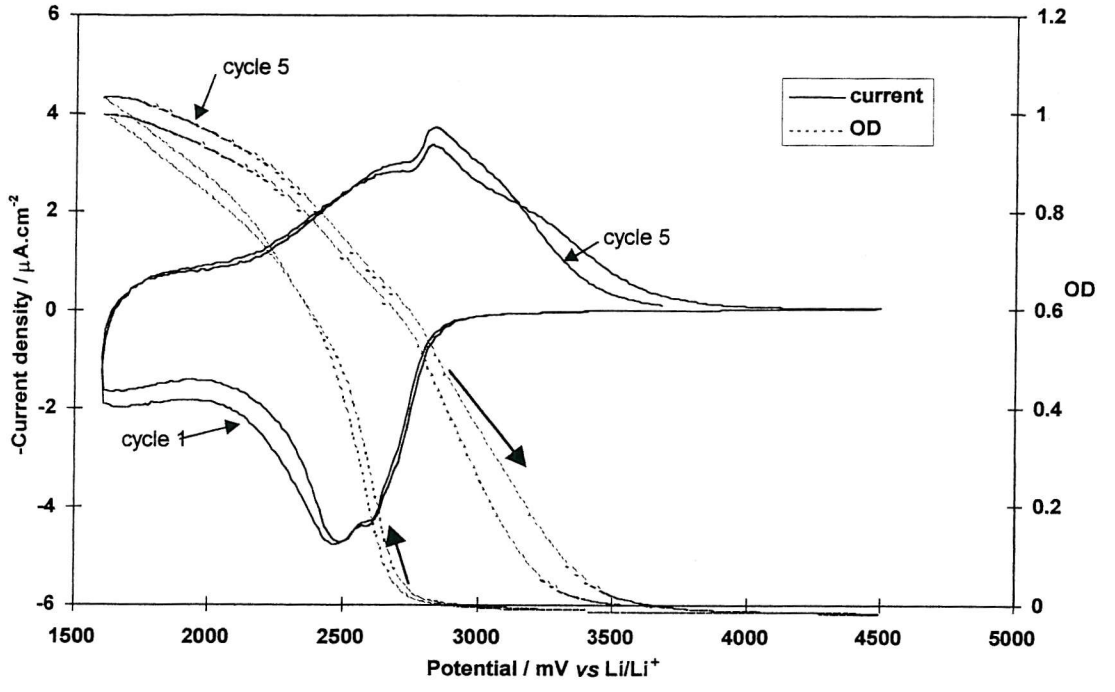

Figure 4-42: Cyclic voltammogram and optical density in situ between 1.6 V and 4.5 V *vs.* Li/Li^+ at 0.1mV/s for the sample 3 (sputtered at 400°C with 40% O_2) at Oxford Brookes University.

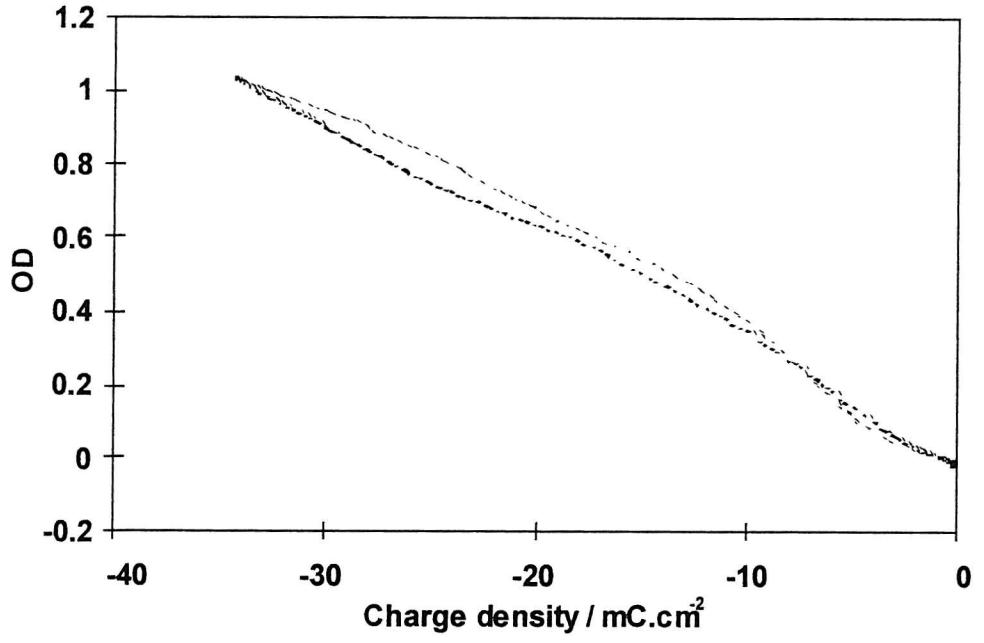

Figure 4-43: Optical density *vs.* charge density for a crystalline tungsten oxide sample.

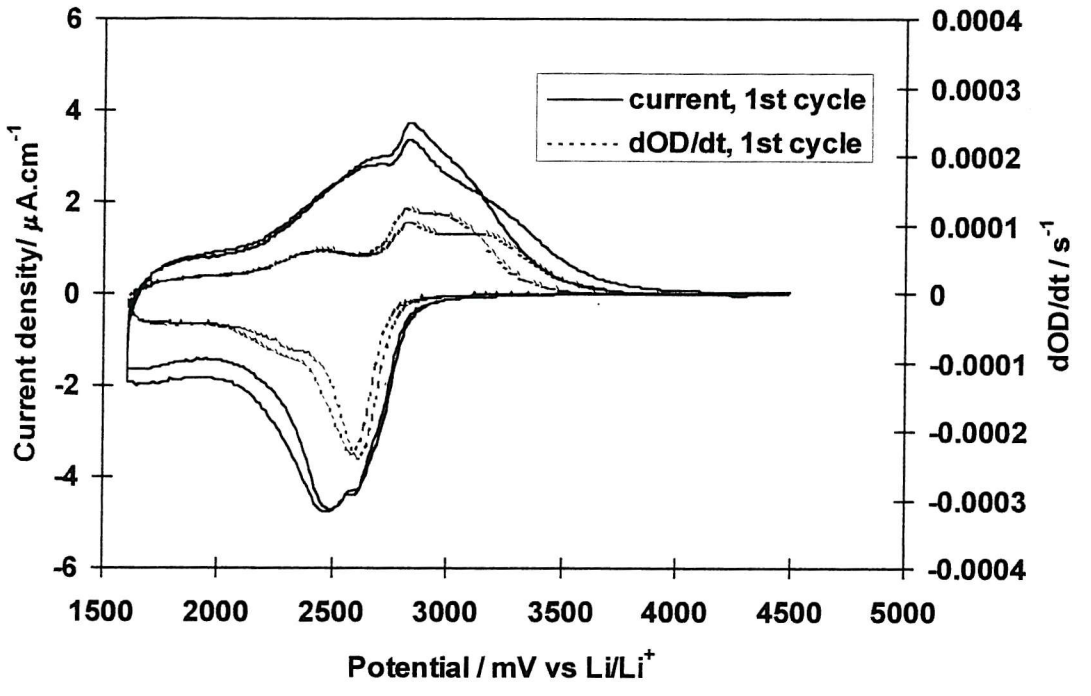

Figure 4-44: comparison of the cyclic voltammogram with the dOD/dt curve.

4.2.3. Effect of the substrate.

In the same way as we studied the amorphous tungsten oxide samples, we investigated the effect of changing the substrate on the stability of crystalline tungsten oxide. Three substrates were used: K-glass, glassy carbon and stainless steel. The results obtained on K-glass are reported in the previous paragraphs.

Figure 4-45 shows the cyclic voltammogram between 2 V and 4.5 V *vs.* Li/Li^+ for a tungsten oxide sample deposited on glassy carbon and annealed at 400°C in oxygen after deposition. The shape of the curve is different from the curve obtained with the same sample deposited on K-glass. The samples were deposited and annealed at the same time but the cyclic voltammogram is different. In the insertion half cycle, two peaks can be observed at 2.7 V and 2.4 V *vs.* Li/Li^+: probably the phase transformation peaks observed with the sample on K-glass. But, in the extraction half cycle, no peak can really be distinguished. The second observation is that the charge extracted is very poor. Figure 4-44 shows the cyclic voltammogram between 1.6 V and 4.5 V *vs.* Li/Li^+ for the same sample: cycles 1, 3 and 5. Although the

voltammogram shows a loss of current between the cycle 1, the loss of current is very small between the cycle 3 and the cycle 5 showing a good stability of the sample at low potential.

Figure 4-46 shows the cyclic voltammogram between 2 V and 4.5 V *vs.* Li/Li^+ for a tungsten oxide sample deposited on stainless steel and annealed at 400°C in oxygen after deposition. The sample was deposited and annealed at the same time as the sample on K-glass and the sample on glassy carbon. Similarly to the sample deposited on glassy carbon, the sample deposited on stainless steel shows two peaks on the insertion half cycle but no peak on the extraction half cycle. The second similarity is the poor extracted charge. The interesting difference between this sample and an amorphous tungsten oxide sample is the good stability of the sample between 1.6 V and 4.5 V *vs.* Li/Li^+ as shown on figure 4-46. Figure 4-46 shows the first cycle and the fifth cycle down to 1.6 V for this sample. They show a very good stability compared to the amorphous samples for which after 5 cycles down to 1.6 V, only 10% of the initial charge could be inserted and extracted.

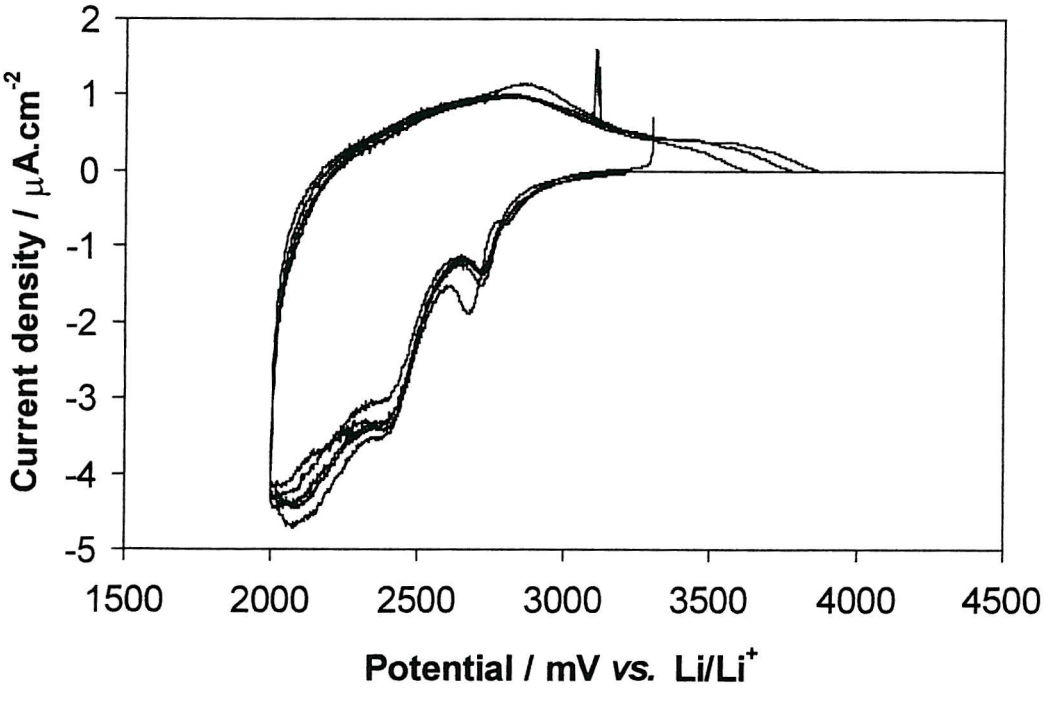

Figure 4-45: Cyclic voltammogram between 2 V and 4.5 V *vs.* Li^+/Li^+ of a WO_3 sample deposited on glassy carbon annealed after the deposition.

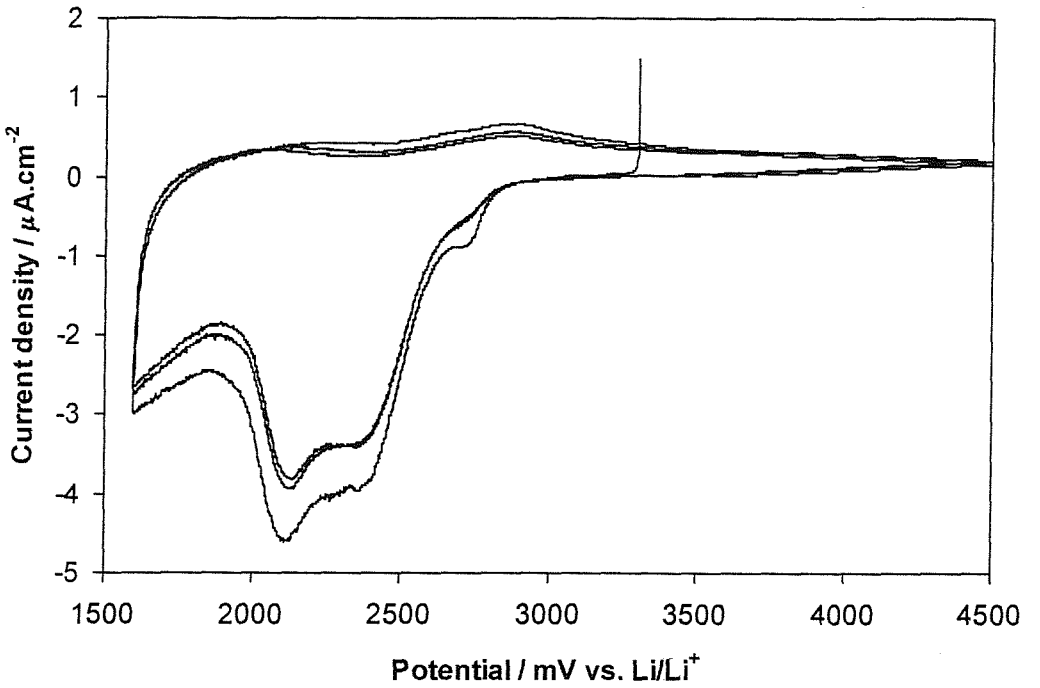

Figure 4-46: Cyclic voltammogram between 1.6 v and 4.5 V *vs.* Li/Li^+ for the same sample as figure 4-45.

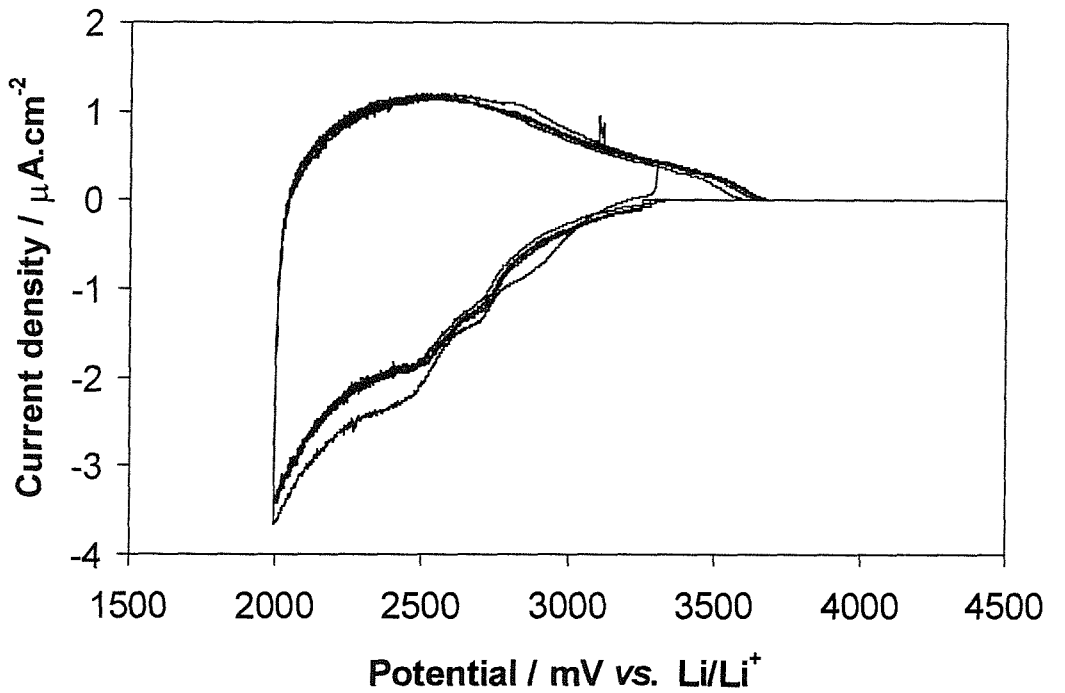

Figure 4-47: Cyclic voltammogram between 2 V and 4.5 V *vs.* Li/Li^+ for a tungsten oxide deposited on stainless steel annealed at 400°C after deposition.

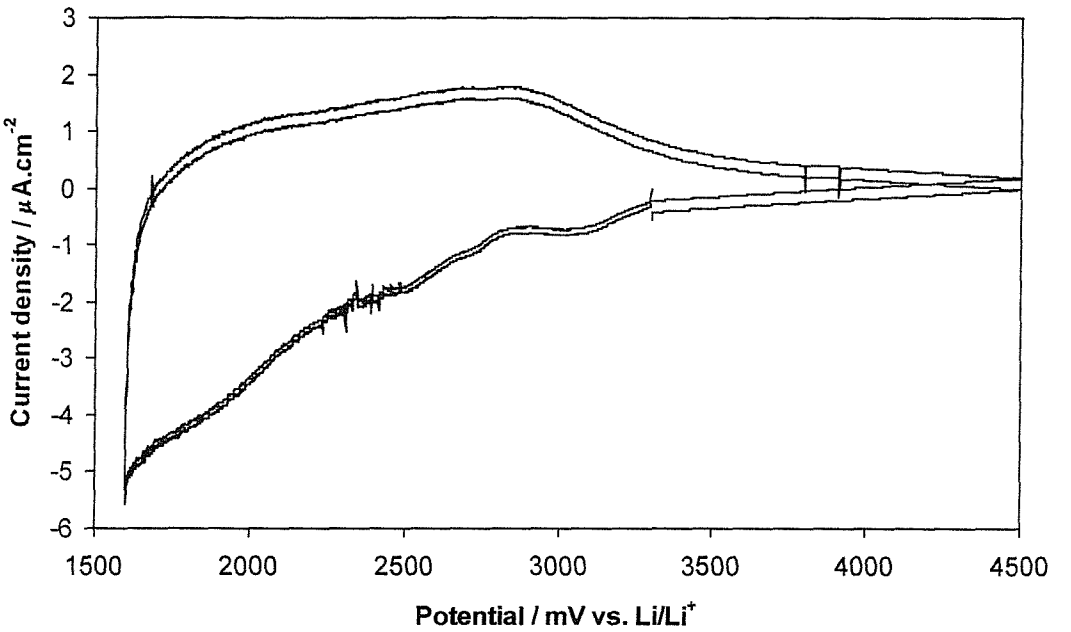

Figure 4-48: Cyclic voltammogram between 1.6 V and 4.5 V vs. Li^+/Li^+ (same sample as figure 4-47).

In both cases, the charge extracted is very different from the charge inserted but there is a very good reproducibility between cycles. Therefore, this charge imbalance is not due to the degradation of the oxide layer. This is very different from the good charge reversibility observed with the crystalline samples deposited on K-glass. The main difference between the K-glass on one side and the glassy carbon on the other side is that K-glass is made of a thin layer of fluorine doped tin oxide deposited on glass whereas glassy carbon and stainless steel are bulk materials. These bulk materials can insert more lithium than a thin film. The cyclic voltammogram of glassy carbon and stainless steel was shown on figures 4-27 and 4-26 respectively. These voltammograms show that glassy carbon and stainless steel can irreversibly insert lithium at potentials below 2.5 V *vs.* Li/Li^+ for glassy carbon and below 3 V *vs.* Li/Li^+. The difference between the charge inserted and the charge extracted can be due to the insertion of the lithium in the bulk of the substrate. If the insertion occurs in the K-glass, it is limited by the fact that it is a thin layer of doped tin oxide on insulating glass.

4.3. Comparison of samples - Conclusions.

Two types of tungsten oxide samples were studied here: amorphous and crystalline tungsten oxide. Table 4-2 summarises the results obtained with all the tungsten oxide samples. Between the amorphous tungsten oxide samples, three types can be distinguished:

- The "standard" amorphous tungsten oxide from Pilkington.
- The amorphous tungsten oxide deposited at higher power from Pilkington.
- The amorphous tungsten oxide deposited at Southampton.

For the three types of sample, the cyclic voltammograms between 2 V and 4.5 V showed a good stability with a small parasitic reaction. Cycling down to 1.6 V *vs.* Li/Li^+ induced a dramatic and irreversible damage for the three types of sample. The difference between the samples was shown by the scanning electron microscopy:

- The "standard" amorphous tungsten oxide had a dissolution patch with some crystals characteristic of a dissolution reprecipitation mechanism.
- The amorphous sample sputtered at higher power had some cracks on the surface of the sample after cycling down to 1.6 V *vs.* Li/Li^+. These cracks are characteristic of the expansion of the lattice until the film buckled up and cracked.
- No evidence of a surface damage was shown by the SEM on the amorphous tungsten oxide sample sputtered at Southampton. But the AC-impedance spectroscopy showed an increase of the interfacial resistance characteristic of a loss of contact between the tungsten oxide and the underlying conductive layer.

The damage mechanism for the sample sputtered at Southampton can be related to the mechanism of damage of the sample sputtered at high power from Pilkington as the formation of cracks implies a loss of adhesion between the oxide layer and the conductive layer.

As far as crystalline tungsten oxide is concerned, cyclic voltammetry showed a very good stability down to 1.6 V *vs.* Li/Li^+. The high temperature processing heat can cause interdiffusion between the substrate and the electrochromic material. The thickness of the interphase is then greatly increased, so that the strain is accommodated progressively, and no loss of adhesion is observed.

Amorphous tungsten oxide	
"Standard" amorphous tungsten oxide from Pilkington	- Good stability between 2 V and 4.5 V *vs.* Li/Li^+. - Very poor stability below 2 V. - Very poor optical stability below 2 V. - SEM after cycles down to 1.6 V showed dissolution-reprecipitation patterns. - Model: dissolution due to localised alkaline conditions and reprecipitation away from the surface where conditions are less alkaline.
High power sample from Pilkington.	- Good stability between 2 V and 4.5 V *vs.* Li/Li^+. - Very poor stability below 2 V. - SEM after cycles down to 1.6 V showed cracks due to compressive stress.
Samples prepared at Southampton	- Good stability between 2 V and 4.5 V *vs.* Li/Li^+. - Very poor stability below 2 V. - SEM after cycles down to 2 V showed no evidence of damage i.e. no pinholes, cracks, etc. - Impedance spectroscopy showed and increase of the interfacial resistance when steps between 1.6 V and 2 V. - Effect of the substrate: relative better stability of the sample if there is an oxide at the surface of the underlying layer. - Model: loss of adhesion due to the excessive stress on the lattice.
Crystalline tungsten oxide	
Crystalline sample obtained by heating the substrate during the sputtering (Oxford Brookes University)	- Good electrochemical and optical stability for both cathodic limits.
Crystalline samples obtained by annealing the samples at 400°C after sputtering.	- Good stability for both cathodic limits. - Experiments done with samples deposited on glassy carbon and stainless steel showed good stability for both cathodic limits on all the substrate but a charge imbalance probably due to the insertion of lithium in the bulk of the substrate.

Table 4-2: Summary of the results obtained with the tungsten oxide samples.

5. Results on vanadium titanium oxide counter electrode.

5.1. *Effect of the sputtering conditions.*

The sputtering conditions have an influence on the electrochemical behaviour of the oxide as seen previously with tungsten oxide. In order to study the effect of the hydrogen pressure in the sputtering chamber, the oxygen flow was varied for a constant argon flow and the samples obtained were tested using cyclic voltammetry. Table 5-1 presents the sputtering conditions for four samples. Figure 5-1 shows the first cyclic voltammograms obtained for these samples. The current was normalised at 2 V vs. Li/Li^+ to allow easy comparison of the first cathodic peak. The insertion half cycle presents a peak around 3.2 V *vs.* Li^+/Li^+. The intensity of this peak increases with an increasing concentration of oxygen in the plasma. This peak corresponds to an irreversible inserted charge, as there is no equivalent in the extraction half cycle. The peak disappears during the second cycle as shown on figure 5-2.

Sample number	Oxygen flow	Sputtering time / min
1	15	5
2	20	10
3	30	10
4	40	10

Table 5-1: sputtering conditions for the $VTiO_x$ samples.

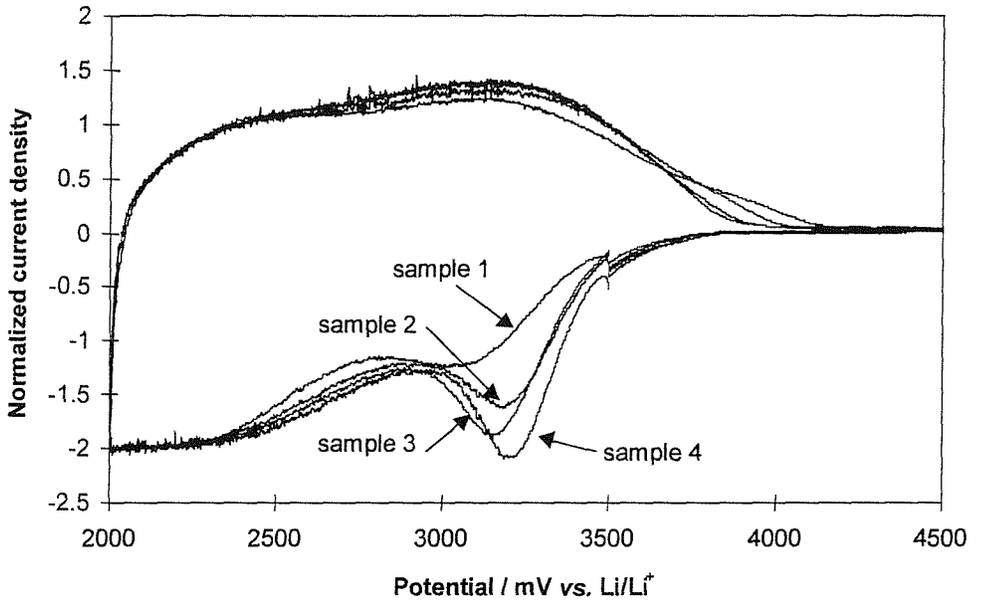

Figure 5-1: Cyclic voltammograms (normalised to the value of the current at 2 V) (first cycle) of $VTiO_x$ samples sputtered at different oxygen flows during the sputtering and an argon flow of 40. See table 5-1 for details.

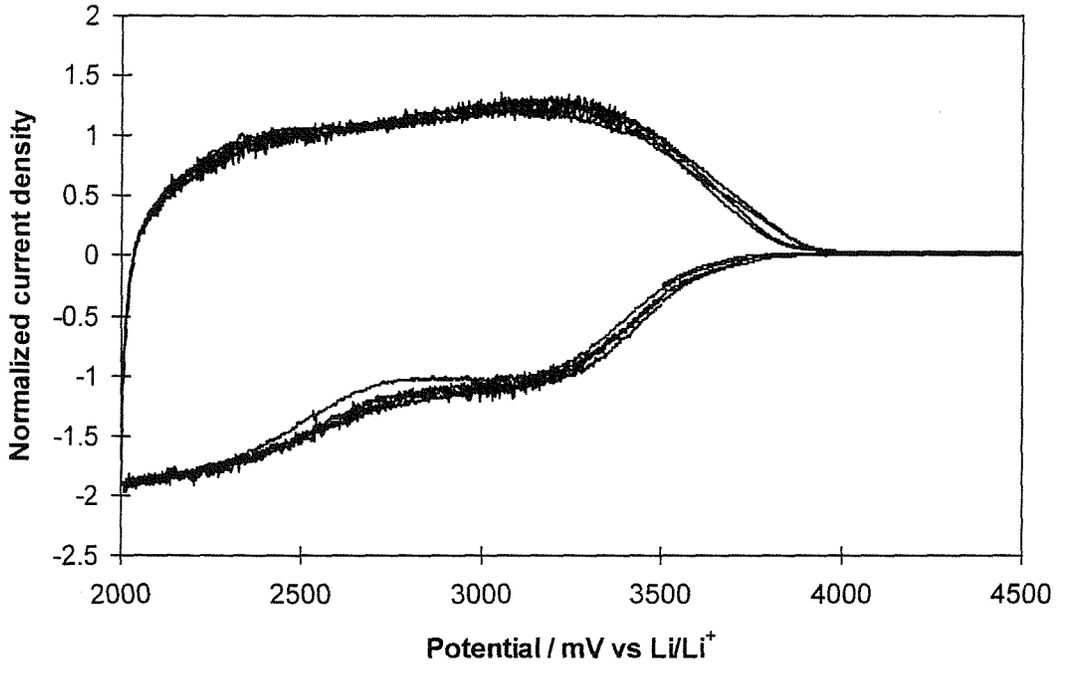

Figure 5-2: Second cycles for the samples showed on figure 5-1.

5.2. *Cyclic voltammetry.*

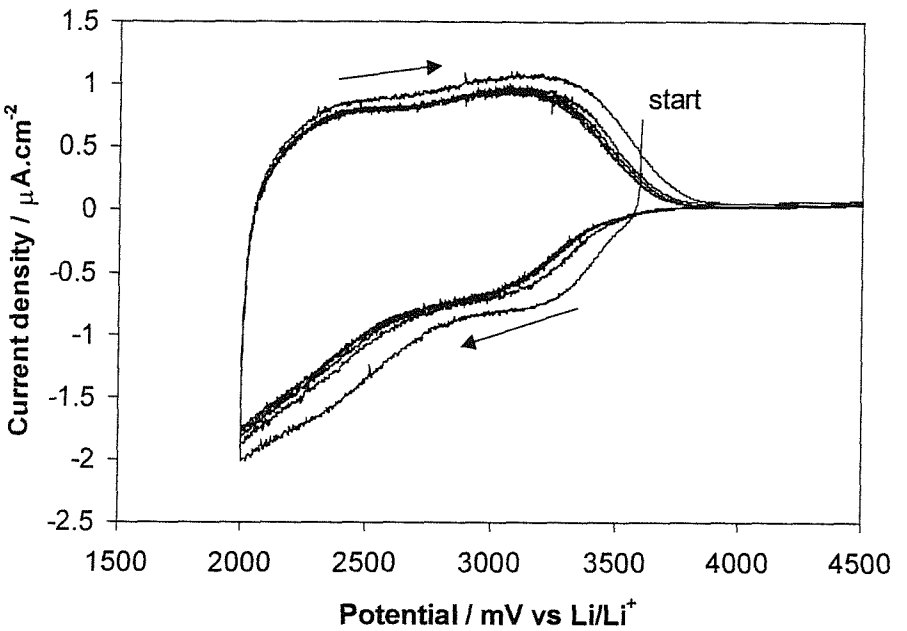

Figure 5-3: Cyclic voltammetry (5 cycles) of $VTiO_x$ on K-glass at 0.1mV/s between 2V and 4.5V vs. Li/Li^+.

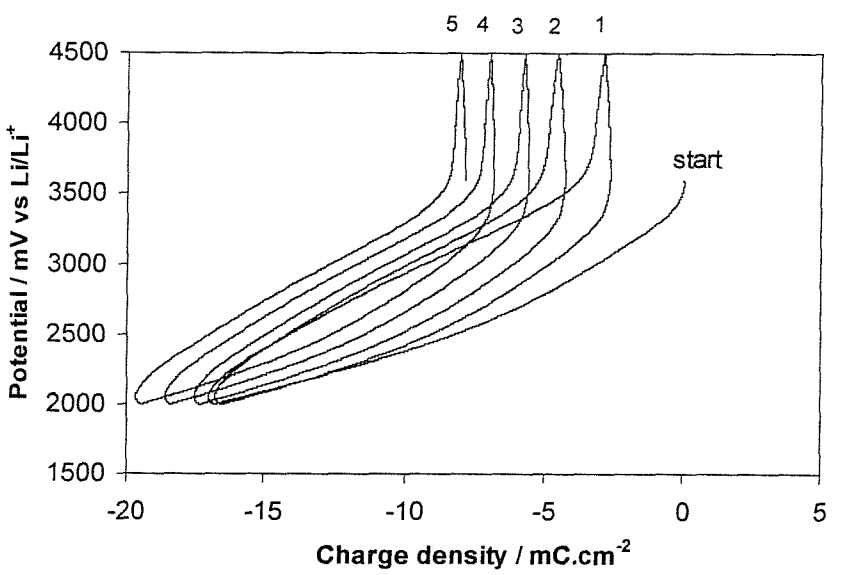

Figure 5-4: Potential vs. charge curves corresponding to the cyclic voltammetry of figure 5-3.

Figure 5-3 shows the cyclic voltammogram obtained with a $VTiO_x$ electrode on K-glass. After a first cycle showing a cathodic peak, the cyclic voltammograms are almost perfectly superposable. Although the cyclic voltammograms are

superimposable, potential *vs.* charge curve shifts progressively towards the cathodic region showing that another cathodic process is occurring (figure 5-4).

The parasitic charge is defined as the difference between the inserted and the extracted charge. To investigate the effect of the potential range, the electrodes were cycled down to low cathodic potentials (1.2 V *vs.* Li/Li^+). The same sample was cycled successively 10 times between 2V and 4.5 V *vs.* Li/Li^+, 5 times between 1.6 V and 4.5 V, 5 times between 1.4 V and 4.5 V and finally 5 times down to 1.2 V *vs.* Li/Li^+.

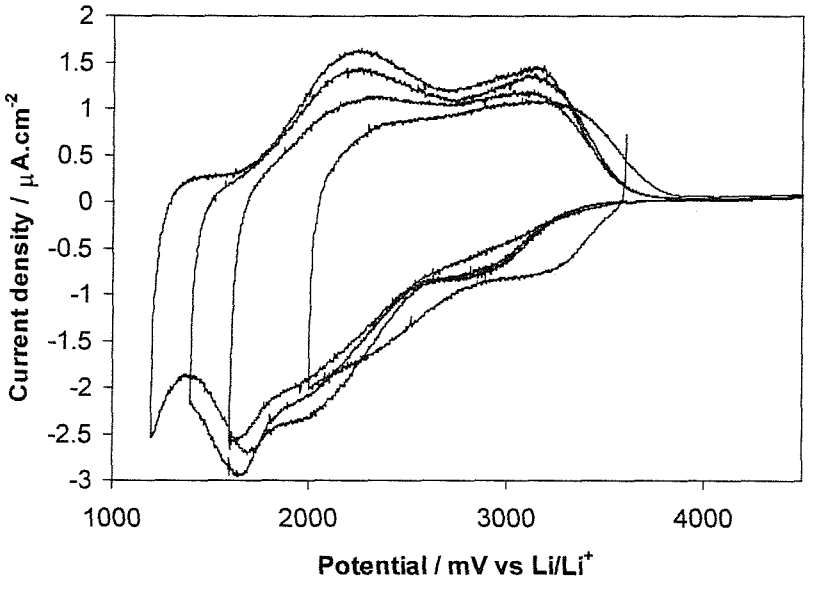

Figure 5-5: Cyclic voltammetry of $VTiO_x$ at 0.1 mV/s for various cathodic limits (2 V, 1.6 V, 1.4 V and 1.2 V *vs.* Li/Li^+).

Figure 5-5 shows the first cycle for each cathodic limit. Cycling down to 1.6 V, the current increases continuously and the shape of the curve is similar to the cyclic voltammogram between 2 V and 4.5 V *vs.* Li/Li^+. Cycling down to 1.4 V *vs.* Li/Li^+, a new peak appears around 1.6V in the insertion half cycle and the extraction half cycle shows two separated peaks. The cyclic voltammograms down to 1.4 V *vs.* Li/Li^+ show a very good stability and reversibility upon insertion-extraction of lithium.

The cyclic voltammograms down to 1.2 V *vs.* Li/Li^+ show a progressive loss of current in the insertion half cycles (figure 5-6) of about 5 to 8 % at each cycle in the lowest potential range of the cyclic voltammogram. As the cyclic voltammograms are perfectly superimposable in the 2 V to 4.5 V potential window, the loss of current

seen at very low potential is probably not due to the degradation of the oxide. Bearing in mind that the vanadium-titanium oxide is deposited onto K-glass and that it was shown that the fluorine doped tin oxide (FTO) layer can irreversibly insert lithium, particularly at low potential, we can assume that lithium is inserted in the FTO layer. In this experiment, the thin FTO layer is probably filling up with lithium. The FTO layer is very thin (~3000 Å) and the insertion sites are limited and the current decreases with the number of cycles.

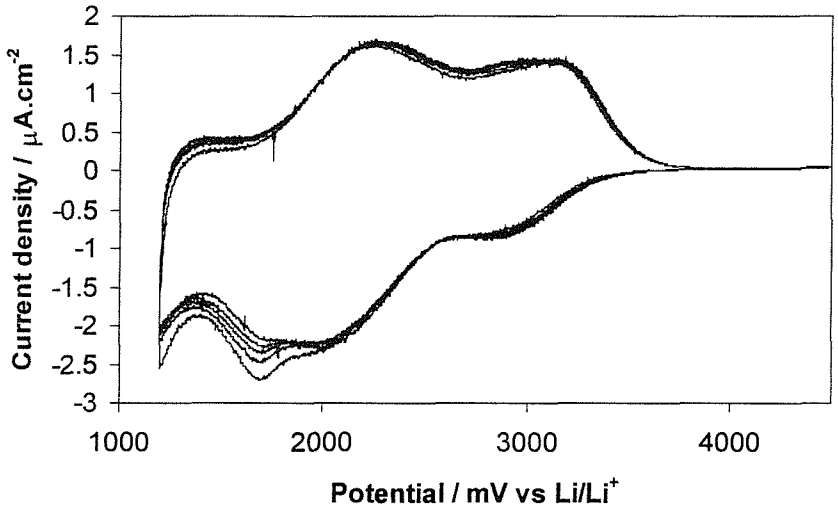

Figure 5-6: Cyclic voltammetry at 0.1 mV/s of $VTiO_x$ on K-glass down to 1.2 V *vs.* Li/Li^+.

Figure 5-7 shows a plot of the inserted charge, extracted charge and parasitic charge as a function of the cathodic limit. The offset current error is less than 2%. Although this plot shows that both the inserted and extracted charges are increasing with a decreasing cathodic limit which is consistent with what we would expect for a samples that shows no dergadation. The parasitic charge is also increasing when the sample is cycled down to a lower cathodic limit but if we consider the parasitic current corresponding to the parasitic charge, we obtain a constant parasitic current of about 1 $\mu A.cm^{-2}$ between 2 V and 1.6 V. The parasitic current is even decreasing if we consider the lower cathodic limit i.e. 1.2 V *vs.* Li/Li^+.

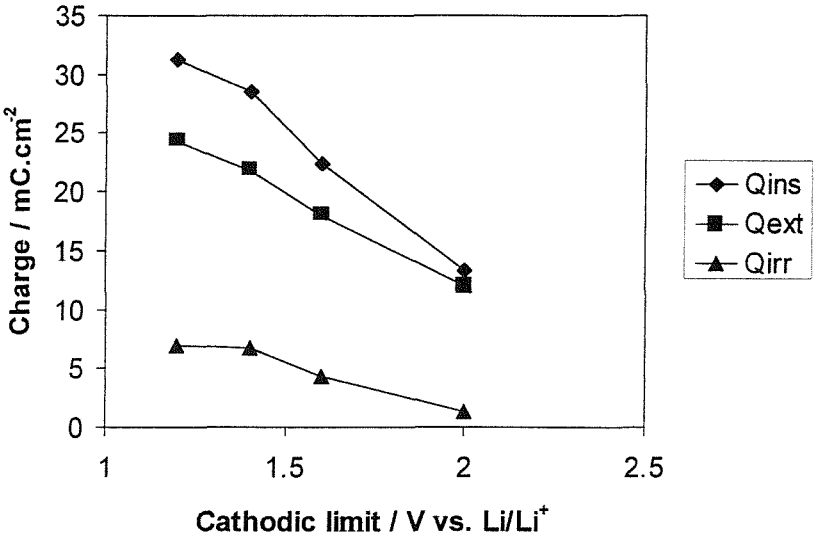

Figure 5-7: Charge inserted (Qins), extracted (Qext) and the parasitic charge (Qirr) as a function of the cathodic limit for the cyclic voltammetry.

5.3. *Electrochemical quartz crystal microbalance.*

Electrochemical quartz crystal microbalance is a very powerful technique to measure variation of mass at the electrode. For the insertion materials, this technique can be used to study the gain/loss of mass due to the insertion/extraction of lithium checking if the lithium is inserted as an ion or solvated by the solvent or traces of water. The second purpose of this experiment was to study the eventual degradation of the electrode and possible loss of mass.

Figure 5-8 shows the first and second cycles obtained with vanadium-titanium oxide deposited on gold-coated quartz as described in chapter 3. The same sputtering conditions were used for the samples deposited on K-glass and on the quartz. The voltammogram was measured at 0.1 mV/s and the admittance of the quartz was measured every 24 mV (1 measure every 10 measures of the current). The cell was thermostated at 30°C by circulation of water.

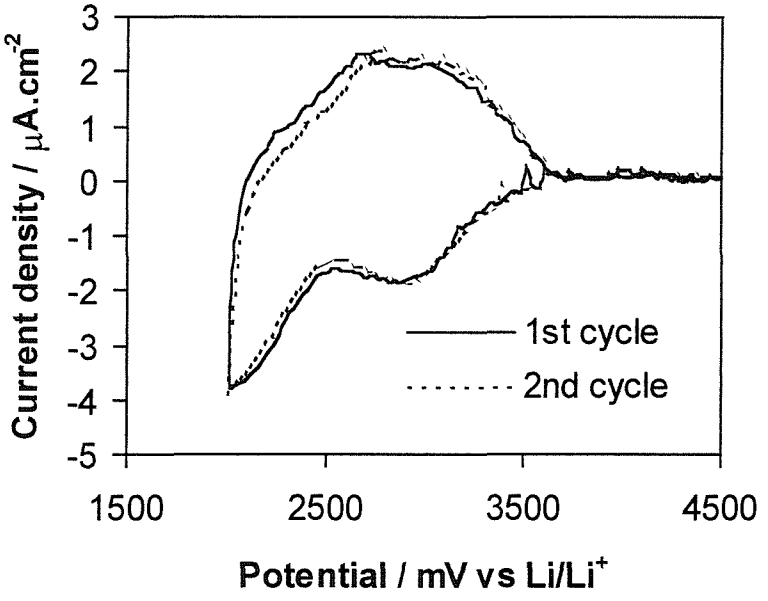

Figure 5-8: Cyclic voltammetry at 0.1mV/s of $VTiO_x$ on the quartz: first and second cycle.

The shape of the voltammogram is very similar to the shape of the cyclic voltammogram obtained with the sample deposited on K-glass shown on figure 5-3: no current is passing through the cell at potentials above 3.6 V *vs.* Li/Li^+ and we can notice a small peak around 3 V. The second cycle shows a lower current both in the insertion and in the extraction half cycle as observed before with the samples deposited on K-glass. The same experiment was done with three different samples to check the reproducibility of the measure and the same result was obtained each time.

The variation of mass is directly proportional to the variation of the resonance frequency of the quartz providing that there is no viscoelastic effect. Figure 5-9, 5-10 and 5-11 shows the typical response of the quartz to the ac signal. Figure 5-9 shows the variation of the real part of the admittance of the quartz with the frequency of the signal. The resonance frequency of the quartz corresponds to the maximum of the curve. Figure 5-10 shows the variation of the imaginary part of the admittance of the quartz as a function of the frequency. The resonance frequency of the quartz corresponds to the inflection point of the curve. On the imaginary part *vs.* real part curve, the resonance frequency corresponds to the maximum value of the real part.

The admittance of the quartz was fitted using the equations described in the theory of the technique (chapter 2) to obtain the value of the parameters of the equivalent circuit: R, L, C and C_0 and the resonance frequency of the quartz. The changes in the viscoelastic properties of the system are shown by the changes in the value of R. In this experiment, the value of R were constant at ± 2%. This shows that we can use the Sauerbrey equation to calculate the variation of mass from the resonance frequency:

$$\Delta f = -\Delta m \left[\frac{2\pi f_0^2}{\sqrt{(\rho_q \mu_q)}} \right]$$

Where f_0 is the resonance frequency of the fundamental mode of the quartz.

ρ_q is the density of the quartz.

μ_q is the shear modulus of the quartz.

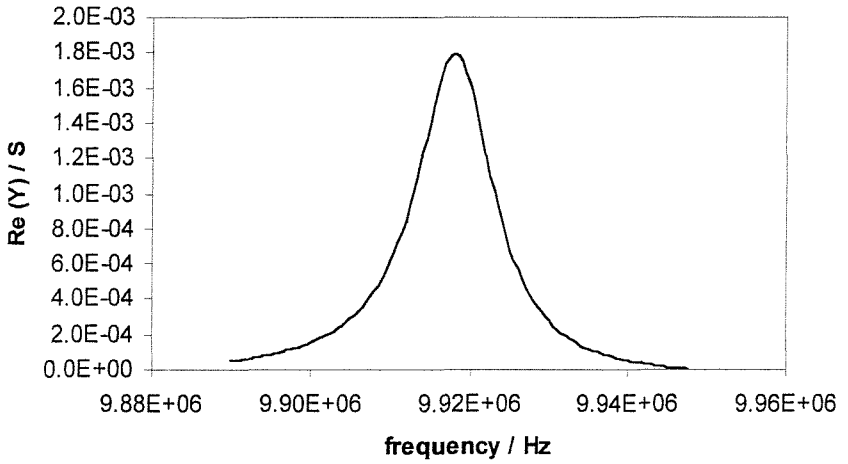

Figure 5-9: Variation of the real part of the admittance of the quartz as a function of the frequency.

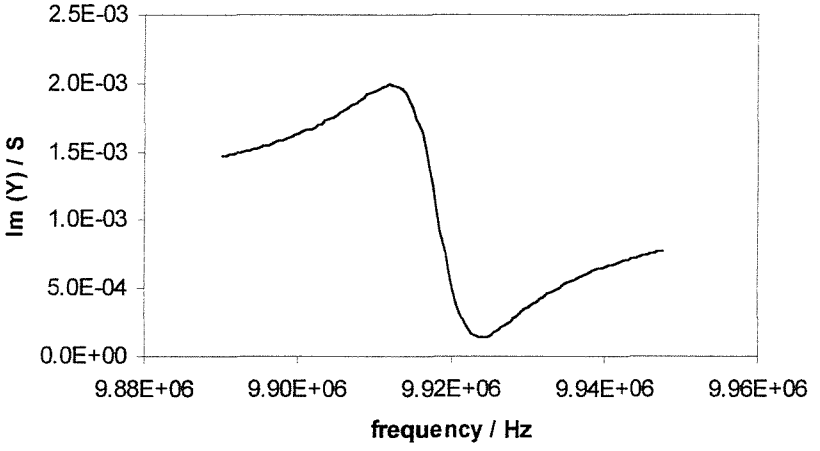

Figure 5-10: Variation of the imaginary part of the admittance of the quartz as a function of the frequency.

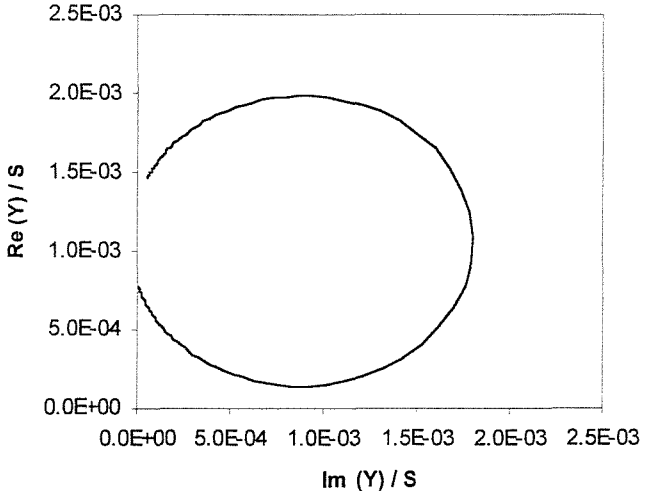

Figure 5-11: Imaginary part of the admittance *vs.* real part of the admittance.

The shape of the curves shown above are modified by the variation of mass. When the mass of the electrode increases, the curves shown on figure 5-9 and 5-10 are shifted towards higher frequencies. The maximum values of the real and imaginary parts are also increased giving a bigger circle on figure 5-12.

Figure 5-13 shows the change of mass as a function of the charge density corresponding to the cyclic voltammograms shown on figure 5-8. At the beginning of the experiment, a loss of mass is observed. Bohnke *et al.* (94) reported the same observation on tungsten oxide and explained it by the expulsion of the specifically adsorbed anion (from the salt) from the electrode surface. But, if we consider a monolayer of anions at the surface of the electrode, the expulsion of the anions from the electrode surface would give a change of mass of about 100 $ng.cm^{-2}$ only. Therefore, this loss of mass could be due to an artefact of the EQCM and not to an electrochemical process. During the insertion, the change of mass is linear with the charge density. By determining the slope of this curve, the mass of the species inserted can be calculated. The mass obtained is very close to 7 $g.F^{-1}$, which corresponds to the molecular weight of lithium. At the very begining of the experiment, the slope is higher than $7g.F^{-1}$, it is about 25 $g.F^{-1}$. This result shows that at the beginning of the experiment, lithium is not the only species inserted. The mass of 25 could correspond to hydrated lithium ion, which could accommodate the surface of the nanocrystalline structure of vanadium titanium oxide. Once that surface sites are full, the only species inserted is lithium as shown by the slope of the curve. In the extraction half cycle, the curve follows the insertion curve until a charge of about –12 $mC.cm^{-2}$, showing a good reversibility of the insertion-extraction process. The slope of the Δm vs. Q curve changes at about –12 $mC.cm^{-2}$ (corresponding to a voltage of about 3.2 V *vs.* Li/Li^+ as shown on figure 5-14). The slope of the curve gives now a mass of 26 $g.F^{-1}$ showing an additional loss of mass. During the second cycle, the change of mass *vs.* charge curve observed during the insertion is almost parallel to the curve obtained during the first cycle. During the extraction, the curve is not superimposable to the insertion curve as observed in the first cycle but the change of the slope at about 3.2 V *vs.* Li/Li^+ is still observed.

Two explanations might be put forward to explain the extra loss of mass. First, it could be the corrosion of the layer. Burdis (16) reported that vanadium is very soluble in water and that the effect of the titanium is to increase the stability of the oxide. Although the cell was assembled in a dry box using a very dry electrolyte, traces of water are always present in the system. But the slope of the curve is 26 $g.F^{-1}$, which would give 3 F per vanadium atoms and it is very unlikely that the vanadium goes from a V^{2+} to a V^{5+}. The second possibility is that the hydrate lithium is extracted again at the same potential. This seems to be a more obvious explanation.

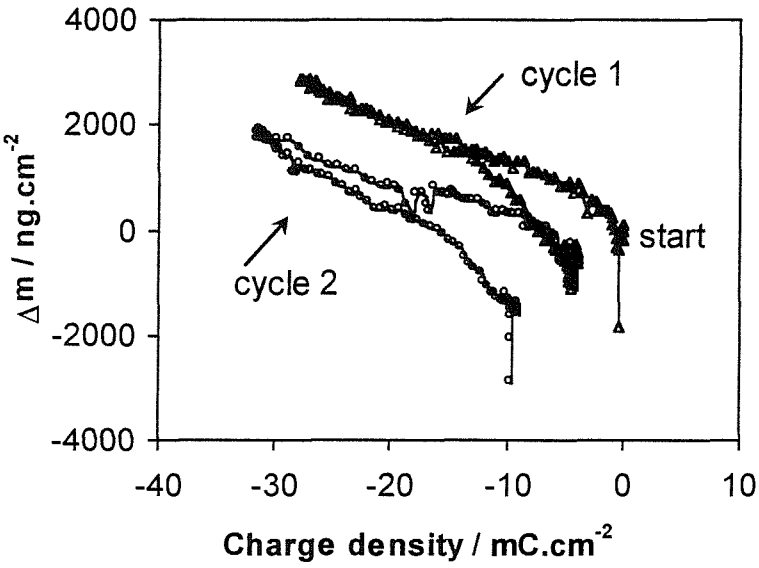

Figure 5-13: Change of mass *vs.* charge plot during cycle 1 and 2 of the cyclic voltammetry on figure 5-8.

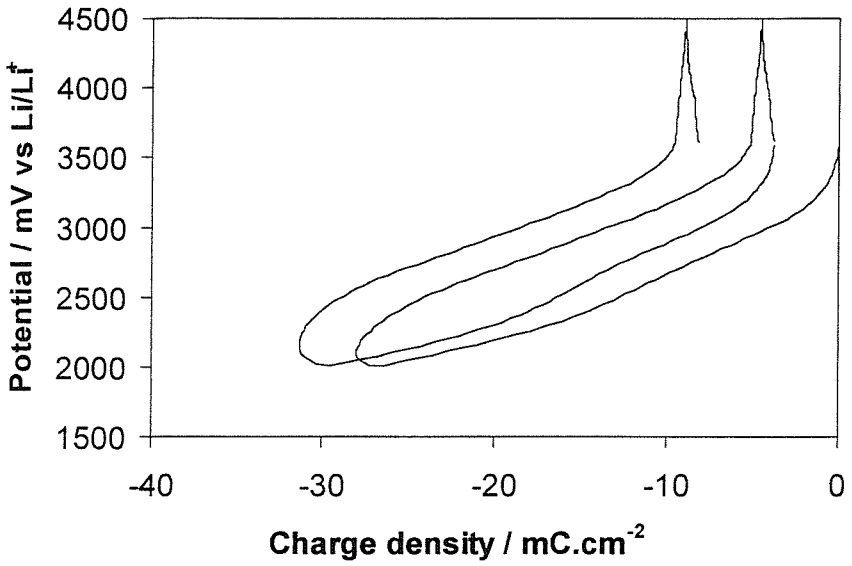

Figure 5-14: Potential *vs.* charge curves corresponding to the cyclic voltammetry on figure 5-8.

5.4. Conclusions.

Cyclic voltammetry of vanadium titanium oxide shows a very good stability of the electrode upon insertion-extraction of lithium. Decreasing the cathodic limit, it has been shown that although the reversibility is very good down to a potential as low as 1.2 V *vs.* Li/Li^+. It was shown that the parasitic current is constant between 2 V and 1.4 V vs. Li/Li^+. The loss of current during the cycles down to 1.2 V is probably due to the lithium filling up the FTO layer and the decreasing number of vacant site for the lithium to enter the FTO layer. The electrochemical quartz crystal microbalance showed that after inserting hydrated lithium under very mild conditions (potentials above 3.2 V) lithium ions are the only species inserted. The second observation was an additional loss of mass is seen during the extraction half cycle above 3.2 V *vs.* Li/Li^+. The more obvious explanation is the extraction of the hydrated lithium.

Further work should try to identify the mechanism responsible for the additional loss of charge.

Chapter 6. Conclusion

The aim of this work was to study the stability of tungsten oxide and mixed vanadium titanium oxide samples to insertion/extraction of lithium. Three different types of amorphous tungsten oxide samples and two types of crystalline tungsten oxide samples were studied. The second objective was to identify the degradation mechanism responsible for the eventual low stability of the samples studied. Slow scan cyclic voltammetry was used to study the behaviour of the samples during insertion extraction of lithium.

Cyclic voltammetry of amorphous tungsten oxide samples showed a good stability between 2 V and 4.5 V *vs.* Li/Li^+ but the charge *vs.* potential curves corresponding to the cyclic voltammograms showed that a parasitic reaction occurred in that potential range usually considered as safe. To investigate the effect of a larger overpotential, the samples were then cycled down to 1.6 V *vs.* Li/Li^+. All the samples showed a dramatic loss of current and charge with cycling down to this limit. The difference between the different samples was seen when we investigated the damage on the surface of the electrodes. The "standard" amorphous samples from Pilkington showed some areas where the tungsten oxide was dissolved and reprecipitated forming crystals on the surface (95). The samples sputtered at higher power from Pilkington showed some cracks on the surface. The samples prepared at Southampton presented no damage of the surface after cycling to low potential and no evidence of dissolution but the effect of the substrate showed that the adhesion of the tungsten oxide layer on the substrate was a key issue for these samples and that the presence of an oxide layer on the surface of the conducting layer improved slightly the cycling performances of the samples. Impedance spectroscopy showed that the interfacial resistance increased with the time at 1.6 V *vs.* Li/Li^+ (96). We proposed a model (97) where the tungsten oxide lattice expands on insertion of lithium. The expansion causes film detachment creating voids at the interface between the tungsten oxide layer and the substrate and failure of the device. To summarise the work done on tungsten oxide, we showed that tungsten oxide is stable between 2 V and 4.5 V *vs.* Li/Li^+ as previously reported in the literature cycling the sample at lower potential causes a device failure.

Cyclic voltammetry of vanadium-titanium samples showed a very good stability of the electrode upon lithium insertion-extraction down to potential as low as 1.2 V *vs.* Li/Li^+, and it was shown that the parasitic charge was constant when the cathodic limit was decreased. At potential below 2 V, lithium is probably inserted into the FTO layer, filling up the layer and causing a decrease of the current when the layer is full. Electrochemical quartz crystal microbalance was used to investigate the mechanism of the damage. It was shown that lithium after inserting hydrated lithium ions on the surface, the only species inserted during the cycle. During the extraction, an additional loss of mass appeared above 3.2 V *vs.* Li/Li^+. This additional loss of mass was probably due to the extraction of the hydrated lithium ions.

Some more work should be done to investigate the mechanism of degradation of vanadium-titanium oxide and the first results using electrochemical quartz crystal microbalance are very promising. It would probably be interesting to investigate the changes of mass at very low potential.

References

1. C.G. Granqvist, *Handbook of Inorganic Electrochromic Materials,* Elsevier, Amsterdam (1995).

2. P.M.S. Monk, R.J. Mortimer, D.R. Rosseinsky, *Electrochromism: Fundamentals and Applications,* VCH Verlagsgesellschaft, Weinheim (1995).

3. J.R. Platt, *J.Chem. Phys.*, **34** (1961) 862.

4. S.K. Deb, *Appl. Opt Suppl.*, **3** (1969) 193.

5. S.K. Deb, *Phil. Mag.*, **27** (1973) 801.

6. D. Krause, V. Paquet, *Electro-Opto. Systems design,* **9** (1977) 54.

7. J.S.E.M. Svensson, C.G. Granqvist, *Solar energy mater.,* **12** (1985) 391.

8. A. Breig, T. Meisel, *Dornier Post*, **2**(1992) 29.

9. I. Brotherston , PhD thesis, Southampton (1997).

10. B.W. Faughnan, R.S. Crandall, *Appl. Phys. Lett.*, **31** (1977) 834.

11. J. Gottsche, A.Hinsch, V. Wittwer, *Proc. Soc. Photo-Opt. Instrum Eng.*, **1728** (1992) 13.

12. A.T. Baker, J.M. Bell, D.R. MacFarlane, B.G. Monsma, I. Skryabin, J. Wang, *Solar Energ. Mat. and Solar Cells*, **39** (1995) 133.

13. L.E. Despero, I. Natali-Sora, L. Sangaletti, G. Sberveglieri, E. Tondello, *J. Solid State Chem.*, **121** (1996) 379.

14. Y.M Li, T. Kudo , *J. Electrochem. Soc.*, **142** (1995) 1194.

15. B. Poumellec, J.F. Marucco., B. Touzelin, *Physical Rev. B.*, **35** (1987) 2284.

16. M.S. Burdis, *Thin Solid Films*, **311** (1997) 286.

17. K. Von Rottkay, N. Ozer, M. Rubin, T. Richardson, *Thin Solid Films*, **308** (1997) 50.

18. T.J. Richardson, K. Von Rottkay, J. Slack, F. Michalak, M. Rubin, *Electrochem. Soc. Proc.,* **98-26** (1999) 158.

19. R.S. Conell, D.A. Corrigan, B.R. Powell, *Solar Energ. Mat. and Sol. Cells*, **25** (1992) 301.

20. Z. Crnjak Orel, M.G. Hutchins, G. McMeeking, *Solar Energ. Mat. and Solar Cells*, **30** (1993) 327.

21. F. Decker, S. Passerini, R. Pileggi, B. Scrosati, *Electrochim. Acta*, **37** (1992) 1033.

22.M.B. Robin, P. Day, *Adv. Inorg. Chem. Radiochem.*, **10** (1967) 247.

23. K. Itaya, I. Ushida, V.D. Neff, *Acc. Chem. Res.*, **19** (1986) 162.

24. J.N. Huiberts, R. Griessen, J.H. Rector, R.J. Wijngarden, J.P. Dekker, D.G. de Groot, N.J. Koeman, *Nature*, **380** (1996) 231.

25. P. Van der Sluis, M. Outerkerk, P. Duine, *Appl. Phys. Lett.*, **70** (1997) 3356.

26. K. von Rottkay, M. Rubin, F. Michalak, R. Armitage, T. Richardson, J. Slack, P.A. Duine, *Electrochim. Acta*, **44** (1999) 3093.

27. M. Armand, W. Gorecki, R. Andreani, in *Second International Symposium on Polymer Electrolytes,* Editor B. Scrosati, Elsevier London (1990) 91.

28. D. Deroo, J.G. Beraud, *Solar Energ. Mat.*, **31** (1993) 263.

29. C.G. Granqvist, C.M. Lampert, *Sciences and Technology of Electrochromics,* Europto Series, Toulouse (1992).

30. D. Schoolman, PhD thesis. Bordeaux, France (1993).

31. R.S. Yeo, *J. Electrochem. Soc,* **130** (1983) 533.

32. P. Aldebert, M. Guglielmi, M. Pineri, *Polymer J.*, **23** (1991) 399.

33. M. Kitao, H. Akram, H. Machida, K. Urabe, S. Yamada, *Proc. Soc. Photo-Opto. Instrum. Ing.*, **1728** (1992) 165.

34. O. Bohnke, C. Rousselot, P.A. Gillet, C. Truche, *J. Electrochem. Soc*, **139** (1992) 1862.

35. S. Passerini, B. Scrosati, A. Gorenstein, A.M. Andersson, C.G. Granqvist, *J. Electrochem. Soc.*, **136** (1989) 3394.

36. B. Zachau-Christiansen, K. West, T. Jacobsen, S. Atlung, *Solid State Ionics,* **28** (1988) 1176.

37. S. Stromme, A. Gorenstein, G.A. Niklasson, C.G. Granqvist, *J. Appl. Phys.*, **76** (1996) 3749.

38. M.P. Cantao, J.I. Cisneros, R.N. Torresi, *J. Phys. Chem.*, **98** (1994) 4865.

39. A.M. Andersson, C.G. Granqvist, J.R. Stevens, *Appl. Opt.*, **28** (1989) 3295.

40. J.G. Zhang, D.K. Benson, C.E. Tracy, S.K. Deb, A.W. Czanderna, R.S. Crandall, *J. Electrochem. Soc.*, **141** (1994) 2795.

41. S.A. Agnihotry, M.N. Kamanasalan, R. Rashmi, R. Ramachandran, M. Pohit, *Bull. of Electrochem.*, **12** (1996) 756.

42. B. Orel, U. Lavrencic-Strangar, K. Kalcher, *J. Electrochem. Soc.*, **141** (1994) L127.

43. P.O. Olivi, E.C. Pereira, E. Longo, J.A. Varella, L.O. de Bulhoes, *J. Electrochem. Soc.*, **140** (1993) L81.

44. U. Lavrencic-Strangar, B. Orel, I. Grabec, R. Ogorvec, *Proc. Soc. Photo-Opt. Instrum Eng.*, **1728** (1992) 118.

45. M.S. Burdis, J.R. Siddle, R.A. Batchelor, J.M. Gallego, *Solar Energ. Mat. and Solar cells,* **54** (1998) 93.

46. M.A. Macedo, L.H. Dallantonia, B. Valla, M.A. Aegerter, *J. Non-Cryst. Solids*, **147** (1992) 792.

47. Z. Crnjak Orel, B. Orel, *Solar Energ. Mat. and Solar Cells*, **40** (1996) 205.

48. N. Kumagai, S. Tanifuji, K. Tanno, *J. Power Sources,* **35** (1991) 313.

49. M. Veszelei, L. Kullman, C.G. Granqvist, K. von Rottkay, M. Rubin, *Applied Optics,* **37** (1998) 5993.

50. A. Azens, L. Kullman, D.D. Ragan, M. Stromme-Mattson, C.G. Granqvist, *Proc Electrochem. Soc.*, **96-24** (1996) 218.

51. D. Keomany, C. Poinsignon, D. Deroo, *Solar Energ. Mat. and Solar cells,* **33** (1994) 429.

52. I. Elfalla, R.D. Pilkington, A.E. Hill, *J. Materials Science,* **26** (1991) 6203.

53. R. Schollhorn, *Angewandte Chemie*, **92** (1980) 1015.

54. M.S. Wittingham, *J. Electroanal. Chem.*, **118** (1981) 229.

55. A.J. Jacobson, R.R. Chianelli, S.M. Rich, M.S. Whittingham, *Mat. Res. Bull.*, **14** (1979) 1437.

56. C.G. Granqvist, *Solid State Ionics,* **70-71** (1994) 678.

57. T.C. Arnoldussen, *J. Electrochem. Soc.*, **128** (1981) 117.

58. H.R. Zeller, H.U. Beyeler, *Appl. Phys.*, **13** (1977) 231.

59. V.I. Kukuyev, L.F. Komolova, M.V. Lesovoy, Y.Y. Tomaspolsky, *J. Microsc. Spectrosc. Electron.*, **14** (1989) 471.

60. M. Green, K.S. Kang, *Solid State Ionics*, **3-4** (1981) 141.

61. B.W. Faughnan, R.S. Crandall, P.W. Heyman, *RCA Rev.*, **36** (1975) 177.

62. O.F. Schirmer, V. Wittwer, G. Baur, G. Brandt, *J. Electrochem. Soc.*, **124** (1977) 749.

63. C. Bechinger, M.S. Burdis, J. G. Zhang, *Solid State Comm.*, **101** (1997) 753.

64. M. Armand, PhD thesis, Grenoble, France (1978.

65. R.S. Faughnan, B.W. Crandall, *Appl. Phys. Lett.*, **28** (1976) 95.

66. S.K. Mohapatra, *J. Electrochem. Soc.*, **125** (1978) 95.

67. C.Ho, I.D. Raistrick, R.A. Huggins, *J. Electrochem. Soc.*, **127** (1980) 343.

68. G.G. Amatucci, J.M. Tarascon, L.C. Klein, *Solid State Ionics*, **83** (1996) 167.

69. D. Guyomard, J.M. Tarascon, *J. Electrochem. Soc.*, **139** (1992) 937.

70. D.H. Jang, Y.J. Shin, S.M. Oh, *J. Electrochem. Soc.*, **143** (1996) 2204.

71. D.A. Buttry, D.M. Ward, *Chem. Rev.*, **92** (1992) 1355.

72. S.I. Cordoba de Torresi, A. Gorenstein, R.M. Torresi, V.M. Vasquez, *J. Electroanal. Chem.*, **318** (1991) 131.

73. O. Bohnke, B. Vuillemin, C. Gabrielli, M. Keddam, H. Perrot, H. Takenouti, R. Torresi, *Electrochim. Acta*, **40** (1995) 1755.

74. O. Bohnke, B. Vuillemin, C. Gabrielli, M. Keddam, H. Perrot, H. Takenouti, R. Torresi, *Electrochim. Acta*, **40** (1995) 2765.

75. B.L. Wu, D. Lincot, J. Vedel, L.T. Yu, *J. Electroanal. Chem.*, **420** (1997) 159.

76. Y. M. Choi, S.I. Pyun, H.C. Shin, *Metals and Materials (Korea)*, **4** (1998) 193.

77. M. Xu, G.A. Parker, *Talanta*, **34** (1987) 512.

78. H.K. Pulker, *Coatings on glass*, Elsevier, Amsterdam, 1984.

79. E.S. McDaniel, *Collision phenomena in ionised gases*, John Wiley and sons, New York, 1964, chapter 13.

80. F.M. Michalak, J.R. Owen, *Solid State Ionics*, **86-88** (1996) 965.

81. M.S. Burdis, J.R. Siddle, *Thin Solid Films*, **237** (1994) 320.

82. O. Bohnke, G. Robert, *Solid State Ionics,* **6** (1982) 115.

83.K.H. Cheng, M.S. Whittigham, *Solid State Ionics,* **1** (1980) 151.

84. M. Green, *Thin solid Film*, **50** (1978) 145.

85. H. Akram, M. Kitao, S. Yamada, *J. Appl. Phys.*, **66** (1989) 4364.

86. H. Kaneko, F. Nagao, K. Miyake, *J. Appl. Phys.*, **63** (1988) 510.

87. G. Barral, J-P. Diard, C. Montella, *Electrochim. Acta*, **29** (1984) 239.

88. R. Cabanel, G. Barral, J-P. Diard, C. Montella, *J. Appl. Electrochem.*, **23** (1993) 93.

89. M. Stromme, A. Gutarra, G.A. Niklasson, C.G. Granqvist, *J. Appl. Phys..*, **79** (1996) 3749.

90. J.S. Chen, J-P. Diard, R. Durand, C. Montella, *J. Electroanal. Chem.*, **406** (1996) 1.

91. D.L. Smith, *Thin-Film Deposition : Principles and Facts*, Mc Graw-Hill, New York, (1995).

92 .Q Zhong, J.R. Dahn, K. Colbow, *Phys. Rev. B. Condensed Mater.*, **46** (1989) 129.

93. P. Judenstein, J. Livage, *Mat. Science and Eng.*, **B3** (1989) 129.

94. O. Bohnke, B. Vuillemin, C. Gabrielli, M. Keddam, H. Perrot, H. Takenouti, R. Torresi, *Electrochimica Acta*, **40** (1995), 2755.

95. B. Gavanier, F. Michalak, J.R. Owen, *Ionics*, **3** (1997) 265.

96. B. Gavanier, N.S. Butt, M.G. Hutchins, V. Mercier, A.J. Topping, J.R. Owen, *Proc. Electrochem. Soc.,* **98-26** (1998) 170.

97. V. Mercier, B. Gavanier, J. Owen, *Proc. Electrochem. Soc.* **98-26** (1998) 152.